THE UNIVERSITY OF CHICAGO

CREATING QUANTUM TOPOLOGICAL MATERIALS WITH 3D MICROWAVE PHOTONS

A DISSERTATION SUBMITTED TO
THE FACULTY OF THE DIVISION OF THE PHYSICAL SCIENCES
IN CANDIDACY FOR THE DEGREE OF
DOCTOR OF PHILOSOPHY

DEPARTMENT OF PHYSICS

BY
JOHN CLAIBORNE OWENS

CHICAGO, ILLINOIS
DECEMBER 2019

TABLE OF CONTENTS

LIST OF FIGURES

ACKNOWLEDGMENTS

My first Chicago winter was the polar vortex year where temperature plummeted so low that the university issued a memo saying going outside was life-threatening. This being my first winter outside of the South, I remember questioning my life decisions. Looking back with that 20/20 hindsight vision, I would not have changed anything. My whole experience of completing my PhD has been an absolute pleasure, from working in lab and learning physics to experiencing the city of Chicago with good friends. There were definitely some frustrating points in research where it looked like we had run into a corner, but having supportive colleagues, mentors, and friends made even the difficult parts seem like a chance for learning.

First off my two advisors Jonathan Simon and David Schuster have been an incredible team of two very different people that pushed me and believed in me to succeed. Jon's constant positive attitude and excitement over our progress really instilled both a sense of value in what we were doing and a vision for the future of the field in which we are working. Jon is one of my favorite people with whom to talk about science- he breaks down new concepts and ideas so quickly into understandable, intuitive pieces. From Jon I learned to turn everything into masses on springs. Besides the science, Jon as an advisor went the extra mile. One particular memory that stands out- At my last DAMOP when I was trying to figure out what to do with my future I remember Jon immediately clearing his schedule for me as many other scientists were hunting him down looking to get some of his time. Jon always tries to make sure you are on track for the career path you want. Dave is someone who you should always talk to when you either have or need some ideas. When you have a good idea, Dave can immediately think of many new applications in which you could use the idea. Dave saw the lattice as a platform for multimode 3D qubits and the chiral cavities as circulators, as just a few examples. The new ideas and directions from Dave make you feel like there is always something fun to do with your research and that you are building useful scientific

tools. As a mentor Dave was insightful and always approachable. He keeps an honest and broad perspective on a graduating PhD's options, and he helped me work through them extensively. One of my favorite memories of Dave as an advisor is him being triple-booked for meetings and accidentally missing all of them because we had lost track of time talking about science in the lab. Also, Dave put in special effort to get to know us all personally, by planning barbiques, superbowl parties, and lab getaways. These experiences were always amazing and I will remember them fondly.

In the lab I received so much support from the very first day. Nathan Schine and I entered the lab together and he is still the first person I go to when I have a fun idea or I want to get better intuition on some physical concept. Not only that but he has been one of those types of friends who will drop whatever he is doing and jump your car for you when you let the battery die (that may have happened more than once or twice). Ruichao Ma came in and immediately cleaned up my whole microwave cavity operation, and provided tons of ideas on how to improve all facets of the project from the day he joined. He was a great mentor who could really strategize and think many steps ahead in designing complex experiments, but then make them seem so clean and simple when he explained them. My first undergraduate student, Aman LaChapelle, was incredible from the first day. He worked hard, had lots of creative ideas, and had a great sense of humor.

I spent most of my first few years of my PhD in the Simon lab, where I got to work with other amazing people- Ningyuan Jia brought me on board and guided me through my first measurements and designs. Alex Georgakopoulos and I had a running joke early on where I tried to present him with unsolvable problems (sometimes serious sometimes arbitrary machining challenges) and he always would seem to find a solution. Mark Stone and Aziza Suleymanzade many times brought fresh perspectives when I was stuck. The whole lab- Albert, Ariel, Logan, Claire, Tianxing, Levanya, and Chuan were great people to work and see every day.

In the Schuster lab I had rapid training in how to make qubits from several members of the lab- Akash Dixit, Brendan Saxberg, and Sasha Anferov sacrificed a lot of their time to bring me up to speed. Brendan came in on the project and brought a lot of energy, excitement, and creativity. Vatsan Chakram spent even more time teaching me how to characterize a qubit and how to perform different procedures on them. Ravi Naik was an amazing person to have in the lab as well; besides always having ideas on new directions in which to take projects, he was also a great mentor when it came to deciding what to do after graduate school. Gerwin Koolstra was not only a great friend, but also was always great to bounce ideas of to figure out what to do next in my research and also my career. Andrew Oriani built and generously let me use the fridge that allowed me to iterate fast enough to solve the cryogenic problems so I could graduate before I turned 30. The rest of the community- Yao, Helin, Nelson, Gabrielle, Kevin, Tanay, Ankur, Nate, Abigail, and Taekwan- made the lab so enjoyable.

I also recieved so much support from people outside of the lab. My friends from my class Nathan and Rachel, Thomas, Aaron, Kieran, Gerwin, Mary, Chris, Gus, and Patrick are incredibly generous, interesting, and fun people. Other friends I met in the department- Simas, Rhys, Jake, and Alex made life much more fun. Also thank you to Andrew and Lauren for their encouragement and kindness. In the machine shop, Luigi was always providing ingenious solutions to the myriad of machining conundrums I threw his was.

Of course, I would also like to thank my family, who have helped me be who I am today and provided constant love. My brother and sister with whom I have gone through everything, my mom and dad who always supported and trusted me, and everyone else, all of whom I could write their own books on how much they have done for me. Finally, I thank Jungmin for all the love, patience, and day-to-day sacrifices she made as I took my time doing the things I loved.

ABSTRACT

The recent rapid advancement in the ability to create and manipulate superconducting qubit systems has created an exciting opportunity to construct quantum materials from the ground up, artificial atom by atom. This thesis will explore the creation of a new architecture of quantum simulation in which we use the circuit quantum electrodynamics toolbox to build quantum topological materials that so far have proven difficult to understand with theory, simulate with computational methods, and realize/measure with other quantum systems. Specifically we design a two-dimensional material in which microwave photons living in a superconducting 3D microwave cavity lattice interact strongly with a time-reversal symmetry breaking magnetic field and with each other. This is the first photonic topological lattice platform compatible with strong interactions. The combination of these interactions will enable the study of fractional quantum Hall systems, where fractionally charged particles called anyons are theorized to exist. This thesis describes how to engineer a tunable, low loss microwave lattice, create a magnetic field for chargeless photons using ferrite crystals, and generate inter-particle interactions using Josephson junction transmon qubits.

CHAPTER 1

INTRODUCTION

One of unifying goals of the diverse field of condensed matter physics is trying to understand how macroscopic properties of materials emerge from simple repeating building blocks. These "emergent phenomena" occur in all type of systems, from granular materials where the shapes of the constituent particles can determine how the material collapses under pressure [6] to elemental metals where effective attractions between electrons due to the atomic lattice results in a reorganization of the electrons into Cooper pairs and dissipationless charge transport [7]. Quantum materials have particularly interesting emergent phenomena, since the strange properties of quantum mechanics, such as entanglement and wavefunction topology, define the macroscopic behavior of the material. Entanglement can lead to non-local effects and new types of quasiparticle formation (Cooper pairs or Bogoliubov quasiparticles [8]), and when combined with topological effects can create even more exotic quasiparticles that have different exchange statistics and fractional charge like anyons. Interactions between the particles are what causes entanglement, but random defects or thermal lattice excitations that are in most systems often end up scrambling the phase of the quantum wavefunction, which can make entangled quantum materials difficult to realize. However, the discovery of high-temperature superconductivity [9] and the quantum Hall effect at zero field showed that macroscopic quantum effects can be realized at less extreme conditions and spurred the community towards developing many new quantum systems.

There are several challenges to designing quantum materials that makes creating artificial, customizable quantum systems a rich field of research. There are many open questions theoretically, since adding interaction/entangling terms to the Hamiltonian makes them analytically unsolvable and numerically unreachable for large systems due to the exponential scaling of the Hilbert space size with particle number. Experimentally, synthetic quantum

materials offer Hamiltonians designed from the ground up, with every interaction, coupling, and frequency term controllable. Quantum phenomena can be more completely mapped out through correlation functions measured not only on a site-by-site basis, but also as a function of time, since the energy scales of interactions vary depending on what particles are being used. The potential ability to control all of these parameters and then to measure the interplay of interactions comprehensively has created a community with the goal of building synthetic quantum materials from larger particles such as atoms or photons or even phonons.

While considerable success has been achieved in creating quantum materials out of cold atoms trapped with lasers, we have developed a novel architecture for studying quantum materials using tools from the circuit quantum electrodynamics (cQED) toolbox. In this system, the interacting quantum particles are microwave photons that are trapped in microwave cavities (Figure1.1). Although microwave photons do not interact naturally with one another, the effort to develop a digital quantum computer has lead to the creation of powerful tools to create synthetic "atoms" with customizable energy levels that are so anharmonic that absorbing a single microwave photon can change the frequency of absorbing another photon by more than 5% of the frequency. One of the most successful tools developed to date is the transmon qubit [10], which has long lifetimes ($> 100\mu$s [11]) while still maintaining large anharmonicities ($100 - 400$ MHz). These artificial atoms can mediate interactions between microwave photons via a blockade effect, similar to the Rydberg blockade that is used in cold atoms [12]. The sheer flexibility, control, and favorable interaction strength to decay ratio makes the microwave photon a promising candidate with which to build quantum materials.

This work has pioneered several paths toward specifically making quantum *topological* materials out of microwave light a reality. We have developed and tested a method to combine strong nonlinearities with time reversal symmetry breaking topology in a low-disorder system where dynamics and eigenmodes are easily measured. This work is easily translatable to Bose-Hubbard model physics as well - combined with the dissapitive stabilizer [13] developed

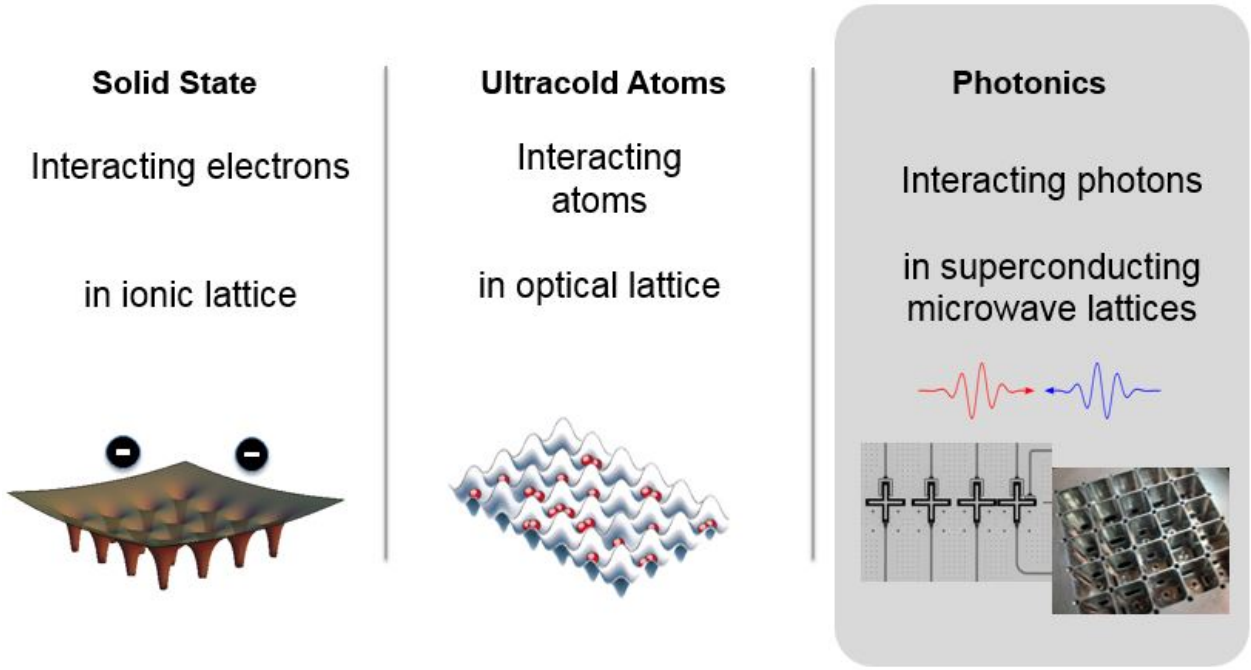

Figure 1.1: The three main architectures for building quantum materials. Shown on the right are two examples of cQED simulators– 3D cavities and printed 2D circuits

alongside the Chern insulator we can explore physics with large interactions and arbitrary filling factors (Chapter 6). Finally, this system already has the qualities to explore new physics in chiral quantum optics [14], since we have already coupled single photon emitters to chiral edge channels. Superconducting circuits and cavities are powerful tools not only to perform universal quantum computation, but also to study quantum materials, condensed matter physics, and quantum optics.

In this thesis, I will discuss the work done specifically to create a 3D microwave photon material that not only has strong inter-particle interactions, but also has a similarly strong magnetic field interacting with the microwave photons. These two interactions are married prominently in studies of the fractional quantum effect, which is the one of the main directions we intend to explore.

1.1 Topological Materials and the Fractional Quantum Hall Effect

Initial interest in the quantum Hall effect arose from the unexpected observation of quantized transport in electronic heterostructures [15]. In the intervening years, we have come to understand that this property is the direct result of a topological winding number of the Bloch wave-function in the Brillioun zone – physics which is robust not only to disorder but also to inter-particle collisions [16]. In this interacting case, the lowest-lying excitations, "anyons," are of particular interest, as they are quasi-particles of fractional charge [17], believed to have fractional statistics [18]. The statistics of particles in a quantum material strongly affect the macroscopic behavior – for example, superfluid formation is possible because of bosonic statistics. Anyons could not only be the building blocks for whole new classes of quantum materials, but there are also proposals suggesting that the robustness of anyons and the ability to store information in "braiding" anyons' paths in time could make anyons a promising candidate for quantum computing [19].

To date, definitive proof of fractional statistics remain elusive, though transport measurements in anyon interferometers [20, 21] are highly suggestive [22]. As new material platforms are developed, so are new measurement techniques and new perspectives on the underlying physics; both particle-by-particle construction of rotating punctured topological fluids [23] and impurity interferometry [24] promise direct experimental signatures of the braiding phase/braid group of anyons, but require either the ability to construct a small Laughlin puddle one particle at a time, or the binding of an anyon to a mobile impurity that is itself transported through an interferometer. While it is unclear how to achieve this in electronic materials, microscopic control in synthetic materials made of much larger photons or trapped atoms is feasible.

Synthetic topological materials fall into three principal categories: those made of ultracold

atoms [25], phonons [26, 27], and light. In both cases the challenges are (1) to engineer a synthetic gauge field for the (charge neutral) particles; and (2) to mediate interactions between them. In the case of ultracold atoms, s-wave contact interactions arise by default [28], while inducing gauge fields requires rotation of the atomic gas [29, 30], Raman couplings [31, 32], or lattice modulation [33, 34, 35], at the cost of reduced energy scales and challenges in state preparation [36]. For materials made of light, synthetic magnetic fields have been realized across the electromagnetic spectrum, from the optical [37, 38, 39] domain, to microwave [40] and RF [1] photons, to even phonons [26]. Because photons do not naturally interact with one another, the principal challenge is to realize a topological meta-material which is compatible with strong interactions. In the optical domain, Rydberg electromagnetically induced transparency is a possibility [12, 41]; in the microwave, circuit QED tools offer a viable solution [42, 43].

1.2 Advantages and Challenges of Building Quantum Materials Using Circuit QED

Due to many impressive results in building quantum materials, trapped atomic lattices are the standard to which to compare synthetic quantum material systems. The largest raw parameter advantage superconducting circuits have is the interaction strengths, which control the dynamics of the material. While cold atoms typically have kilohertz dynamics, circuits can be designed to have interaction strengths ranging all the way to gigahertz. Atomic lifetimes can be very long, often up to seconds [44], but 3D microwave cavities have also recently advanced to having lifetimes of several seconds in FermiLab SRF cavities [45]. While these cavities are not yet practical to use while making quantum materials, cavities that we use in our lattices have already achieved lifetimes greater than 100 milliseconds after etching and baking. Transmon qubits, the source of the nonlinearities and interactions

in our material (which we describe later in the thesis), have lifetimes in state of the art samples of 100μs, though these lifetimes are constantly increasing. Circuit QED systems have the potential to have much larger ratios of the interaction energies to the lifetimes of the particles in the system, which is important in order to explore the dynamics of a material before particles decay.

Another benefit that comes with using cQED is the flexibility of both printed circuits and 3D cavities. Parameters of the circuits are completely tunable, either in the fabrication or often by knobs that can be turned mid-experiment. For example, the frequency of qubits can be tuned by changing the magnetic field through a superconducting quantum interference device (SQuID) loop. The coupling between elements such as cavities and qubits can be calculated by simulation and then fabricated with high precision. Useful features such as inductors, capacitors, waveguides, and cavities are near lossless and can be created modularly as needed. Furthermore, circuits and cavities can be coupled and connected to each other synthetically, allowing control over which mode is coupled to another mode, instead of only coupling to each other as a function of proximity. This allows interesting lattice models to implemented, such as lattices in hyperbolic space [46], higher dimensional lattices [2], or Möbius strip boundary conditions [1]. Superconducting circuit materials are built from the ground up, site-by-site, which has exceptional potential for control over the desired Hamiltonian.

The microwave toolbox also has answers for creating magnetic field for interacting photons, which can be difficult in interacting atom systems. In Chapter 2 I go into much more detail on how we specifically do this. Yttrium Iron Garnet (YIG) is a ferrite that has a chiral, high quality factor mode that can be tuned into the microwave regime and coupled to microwave cavities to break time reversal symmetry and impose a magnetic field on microwave photons. The vast resources available when working in the microwave regime is an advantage that solves many problems not only in material design but also in measurements and characterization.

Finally, microwave lattices are physically much bigger than any other quantum simulator (centimeter scale), and this allows access to individual lattice site spectroscopy. We can control which sites or modes we populate or measure. We can directly measure correlation functions on a single site level, which can lend insight into how entangled materials work. Microwave photons can be observed moving from one site to another, and they can also be measured as a function of time. This allows dynamics of the system to be measured more thoroughly than in other systems.

However, there are also significant challenges using microwave photons to make quantum materials. While there is great control over individual sites, this inversely means that each individual site must be controlled well, or the disorder in the system can be a limiting factor. All of the control knobs on the system are for individual sites, and there are no global control knobs like the ones available in atomic systems. In practice, this will limit system sizes (especially combined with the larger lattice sites).

Additionally, controlling the loss in microwave systems can be difficult since new elements must be added to break time-reversal symmetry, which can add potential loss channels. Only certain lossless materials can be used inside of the system, and transmons must be made carefully to avoid limiting the system from loss. Lossy modes from antennas or cavity seams (more on this in section 2) must be carefully removed or else they can limit the system.

Last, none of the interactions (magnetic field or inter-particle) come by default for microwave photons and must be individually engineered. While this is useful because it allows creative freedom in the design, this also add a lot of complexity to the system. For example, in order to generate equal particle-particle interactions on every site, a qubit must be controlled, maintained, and added to each lattice site. This greatly increases either the cost and instrument requirements (if every qubit must be controlled actively during an experiment) or it must be designed around (qubits would have to be more passive and not frequency tunable).

1.3 Thesis Overview

In Chapter 2, I will discuss the many techniques we developed in designing the 3D microwave cavities that serve as the lattice sites for the material. In this section I will discuss how we trap the photons effectively and efficiently, how we control the site frequencies and tunneling rates, and how we engineer cavities that are used to generate a synthetic gauge field for the photons. In Chapter 3, I will show how we made the first Chern insulator for microwave photons and then examine the properties of the material we created. This material was measured at room temperature without particle interactions and superconducting cavities. In Chapter 4, I will explain how we adapted the Chern insulator to work at cryogenic temperatures. I will go through all of the technical innovations that were required to make this happen. In Chapter 5, I will explore the recent efforts to couple transmon qubits to the lattice sites in order to generate the nonlinearity necessary to create effective inter-particle interactions. This will include a detailed explanation of the cQED techiniques and theory used in coupling a single qubit to a single lattice site. This section will end with the most recent results in coupling a transmon to the topologically protected edge modes of the lattice. In Chapter 6 I conclude with an outlook of the exciting work that can now be done with these systems.

CHAPTER 2

MICROWAVE CAVITIES AS PHOTONIC LATTICES

2.1 Introduction

Most of technical innovation covered in this thesis centers on how to engineer lattices for microwave photons out of 3D cavities. These lattices define the potential which the microwave photons experience. Using 3D microwave cavities as the lattice gives you several advantages in both creating and studying quantum materials, explained in greater detail in the introduction. First, microwave photons are centimeters in scale. This means that each lattice site's pertinent parameters can be customized and added modularly, and individual sites can be resolved and thus dynamics can be studied with single site resolution. Additionally, the connectivity between cavities can be controlled. Unlike other quantum materials, the particle's probability to tunnel to adjacent lattice sites is not just a function of distance between sites. Both long-range tunneling and short-range blockading of tunneling can be achieved to engineer exotic geometry [46], higher dimensionality [2], or lattice models with connectivity that leads to exotic band structure [1]. Finally, 3D microwave cavities allow you freedom to tailor-make the wavefunctions of individual lattice sites, and we use that freedom to develop many of the significant technological innovations that allow the creation of topological quantum materials.

In the pursuit of developing tools that break time-reversal symmetry and create inter-particle interactions simultaneously, we explored using many different microwave platforms. We started with transmission lines of inductors and capacitors to create a time-reversal invariant topological insulator [1], shown in Figure 2.1. We then tried to break time-reversal symmetry in this setup by replacing some of the capacitors with varactors that could be modulated in real time, generating a time-reversal symmetry breaking gauge field similar to results with

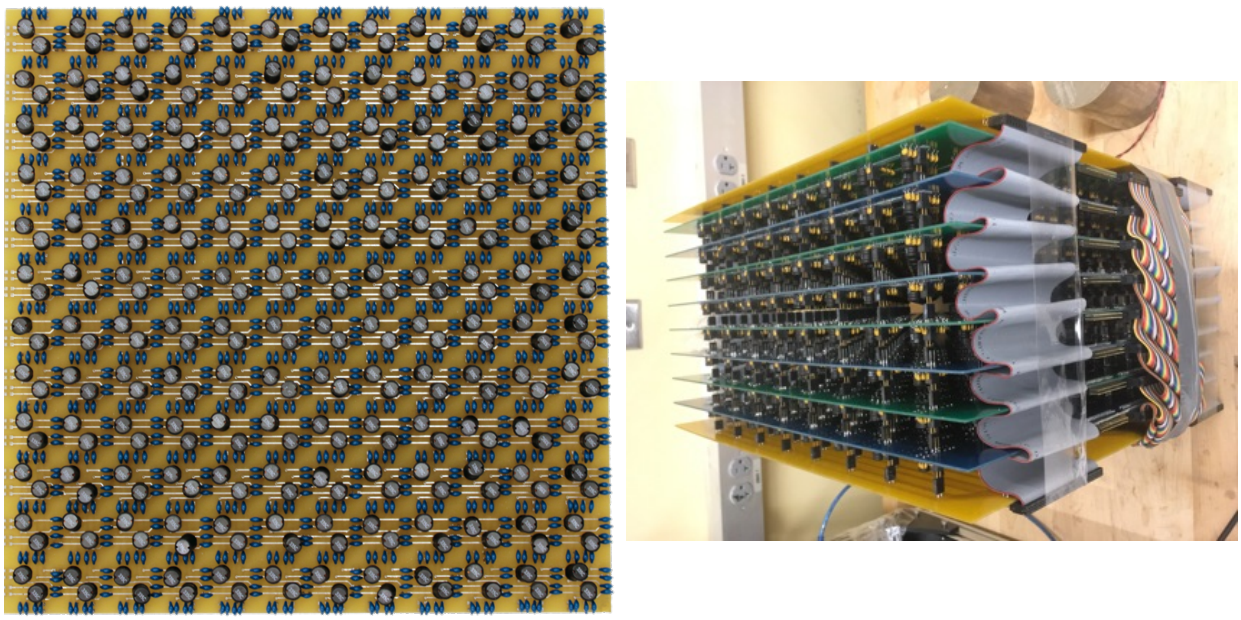

Figure 2.1: **(a)** 14x14 topological circuit discussed in our earlier paper [1] **(b)** Weyl semimetal made from inductors and capacitors [2]

both microwaves [47, 43] and atoms [48]. Similarly, we tried coupling an Yttrium Iron Garnet sphere (much more detail on these work in section 2.3) to the inductors, since an applied magnetic field on the YIG sphere coupled to an inductor can tune the its inductance. While these schemes are not necessarily unreachable, extra loss is added when using varactors, and the inductive tuning is quite small and requires large fields. We realized that moving to 3D lattices improves most of the parameters (such as quality factors of resonators) of the system while providing potential paths towards strongly breaking time-reversal symmetry in a way that maintains high quality factors (Section 2.3) and qubit compatibility (Chapter 5).

2.2 Trapping Photons Effectively

Achieving a long particle lifetime for the photons trapped in the microwave lattice is important because otherwise the particles will decay before any of the interesting interactions occur. 3D microwave cavities have been shown to be incredibly good at trapping photons for long times, up to seconds for certain cavity geometries [45]. These long life times, especially

compared to the interaction strengths achievable with microwave photons are what make microwave photons a particularly exciting candidate to achieve universal quantum computing. Interactions with qubits can reach gigahertz, qubit anharmonicities (of transmons) are typically hundreds of megahertz, and interactions with magnetic fields in our lattice break time reversal symmetry by ~400 MHz, which is what limits how large our site-to-site tunneling to ~30 Mhz. However, achieving high life times also is one of the central challenges to making a microwave system a good quantum material, and constant care has to be taken to avoid loss mechanisms.

There are three main categories of loss that must be considered in order to achieve high lifetimes in cavities: leakage to the vacuum or other modes, material effects (usually resistive or dielectric losses), and measurement losses. Leakage to the vacuum comes in several forms, most notably due to evanescent decay out of a hole in the cavity or coupling to modes that are created from a seam in the cavity if the cavity is not monolithic. Typically these loss sources can be removed or minimized by careful design of the cavity geometry. Material losses, on the other hand, are impossible to completely remove but there has been ample work on minimizing it [49, 45]. The metal that sets the boundary of the cavity will have resistive losses, though by using superconductors the loss can be greatly reduced. However, there are typically impurities such as oxides or hydrides on the surface of these materials that are more lossy. These effects can also be greatly reduced by etching and baking superconductors to purify them, while also keeping the materials under vacuum [45]. Finally, the measurement of the cavities itself also can be a loss source. See section 2.5.1 for more details on how that loss channel is managed.

2.2.1 Geometric Design

In addition to avoiding loss mechanisms, several things must be taken into account when designing the geometry of the lattice sites. First, the geometry sets the mode density of the resonator. Typically a low density of modes is desired since tuning and controlling a single mode per lattice site is easier and most of the Hamiltonians we are building only need one mode per lattice site. We first look at the most classic of 3D cavity modes such as cylinders or rectangular prisms, or any 3D cavity that can be described by 3 or less length scales (perturbations of length scales much less than a wavelength will not change the basic behavior as well). If we solve for the eigenmodes of a rectangular prism as an example, we get the following result:

$$f_{lmn} = \frac{c}{2\sqrt{\mu_r \epsilon_r}} \sqrt{\left(\frac{l}{a}\right)^2 + \left(\frac{m}{b}\right)^2 + \left(\frac{n}{c}\right)^2} \tag{2.1}$$

where a,b, and c are the side lengths of the cavity and l,m, and n are the mode indices. An important additional restraint is also imposed that only one of the mode indices can be zero in order to solve Maxwell's equations. This means that the lowest frequency mode is set by the two longest lengths, and that the third length can be minimized so that it contributes only cavity modes of much higher frequency. Thus in order to constrain cavity modes to one ground state well isolated in energy, the cavity must have one dimension that is much smaller than the wavelength of the mode being used for the lattice, while the other two dimensions are free to set frequency of the lowest energy mode.

The second constraint on cavity design is that it requires that the cavity support chiral cavity modes, since chiral modes will be essential in generating the magnetic field for the photons. Chiral cavity modes are modes where the phase of the excitation varies linearly with the angular position in the cavity, wrapping from 0 to a multiple of 2π (see Figure 2.2). If you

animate these modes as a function of time, you see the mode pattern rotate either clockwise or counterclockwise. In order to have chiral modes, a cavity must have some rotation symmetry. For rectangular prism cavities, this imposes the restriction that the largest two dimensions must be equal. Second, because of time-reversal symmetry, any chiral cavity mode must have a degenerate chiral cavity mode of the opposite chirality paired with it. This means that the lowest frequency mode cannot be chiral since the lowest frequency mode is nondegenerate (as long as one dimensions is much shorter than the other two). Because of this care must be taken to ensure the ground state of the chiral cavity mode is sufficiently separated in frequency from the higher energy chiral modes.

In my earlier work [3] I employed cylindrical cavities, since they fulfill all of these conditions, while also having the best volume to surface area ratio which minimizes resistive losses in the surrounding conductor (This is especially important at room temperature where the metal is not superconducting). They can have well isolated ground state modes by making the height of the cylinder much smaller than the the diameter. The next excited modes of the cylinder are two degenerate chiral modes, as shown in Figure 2.2. In section 3.3 we discuss how these chiral cavities can be used for making a Chern insulator. In Figure 2.9 we summarize how the frequencies of all the modes depend on geometry and magnetic field.

However, cylindrical cavities had several drawbacks that required a different cavity design in order to overcome. First, the diameter must be on the order of the wavelength which makes the lattices physically large. More importantly, it is difficult to construct cylindrical cavities without a seam, introducing associated losses[50]. In typical 3D qubit experiments[51], the seam in these type of cavities is cut such that no current crosses it significantly reducing loss. However, for chiral modes this cannot be done since the direction of the current rotates in time. This seam loss limits the quality factor even at room temperature, especially for larger cavities and lattices. A significant innovation in this work is to use reentrant-style cavities [52] (see Figure 2.3a) engineered to have appropriate mode structure. This geometry

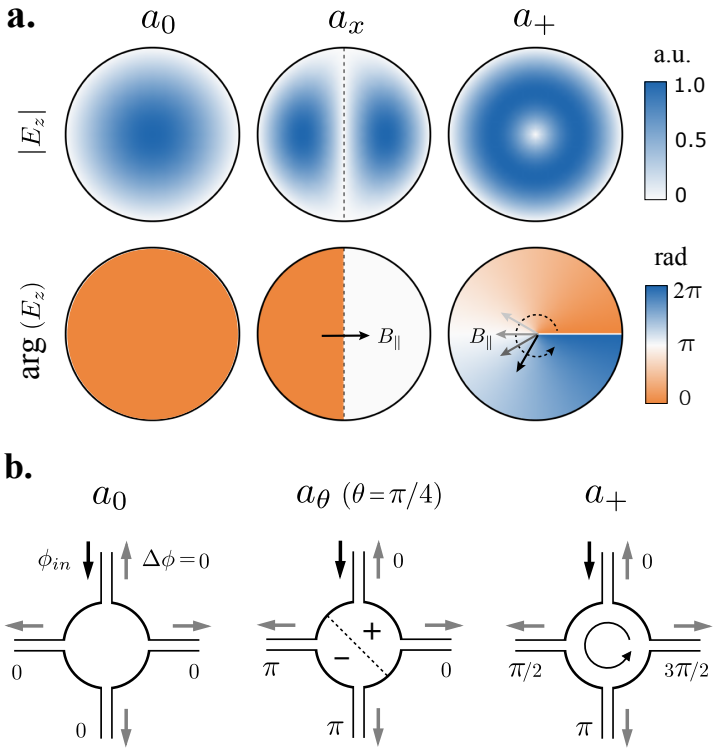

Figure 2.2: **a.** The electric field magnitude and phase of the lowest three modes of a cylindrical cavity where the height is much smaller than the radius. The first column is the lowest energy mode, where the phase is uniform in the cavity. The second and third columns are two separate ways to describe a mode in the second manifold of modes. Since the cavity is cylindrical, the mode can either be descibed in a linear basis like the second column, or it can be described in a circular basis like the third column. For the circular basis, the phase wraps around the cavity from 0 to 2π **b.** Phase acquired by photons tunneling through the different modes of the cavity. For the fundamental cavity, this phase is always zero. However, for the second mode, the phase acquired depends on both the angle between the tunneling ports and the basis chosen! This is rectified by the second degenerate mode in the manifold that cancels the total phase to zero for both modes. This figure is from our original theory proposal paper [3].

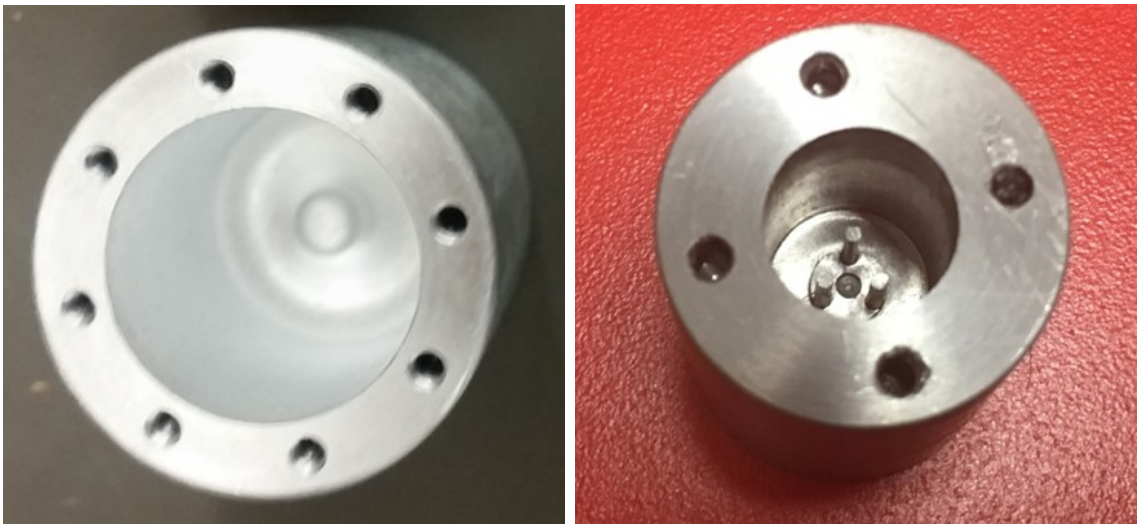

(a) (b)

Figure 2.3: **(a)** Reentrant cavity made of aluminum **(b)** Reentrant cavity made of superconducting niobium with three posts that supports chiral modes.

is both compact, and has no seam loss, making it ideal for current and future studies.

The reentrant post in these cavities creates a new mode in the system. Adding this post is effectively adding a 1D resonator inside the cavity. For example, if a 1D metal rod could be put in a rectangular prism, the rod would have modes dependant only on the length of the rod, with the wavelength of the lowest energy mode being equal to the length of the rod divided by two. If this rod was then connected to the side of the cavity, the rod would still have modes dependent on the length of rod, but instead of a $\frac{\lambda}{2}$ wavelength, the lowest energy mode would have a wavelength of $\frac{\lambda}{4}$. This rod can have a thickness, and the thickness of the rod only perturbatively affects the rod mode frequency. This rod becomes the reentrant post that causes the mode that is used for most of the work in this thesis. Since the post mode is essentially 1D, the post can fit inside a rectangular prism (box) cavity while having substantially lower frequencies than the lowest frequency mode of the box. This is because the lowest frequency of a box is determined by the two longest dimensions of the box, so that 1 dimension of the box can be arbitrarily long without lowering the frequency of the ground state. This long dimension can align with the long dimension of the post. Thus the mode

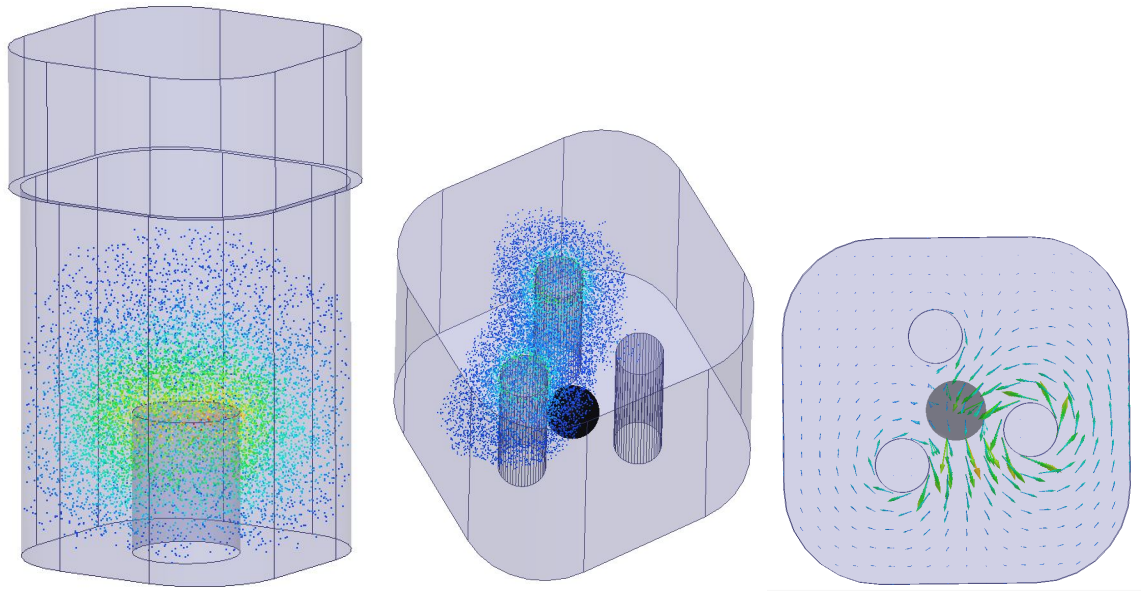

(a) (b) (c)

Figure 2.4: **a.** Fundamental mode cavity electric field. The mode is localized at the bottom of the cavity. **b.** Electric field simulation of one of the chiral YIG cavity modes. A video that shows the rotation as a function of time is available at https://youtu.be/gHoyFxkw9iQ. **c.** Magnetic field of one of the chiral YIG cavity modes viewed from the top. The field at the center of the cavity rotates in time, coupling to the magnetic moment of the YIG.

of the post is trapped inside a cavity that has no modes near it in frequency. This becomes especially useful since the box modes of the cavity are several gigahertz away in frequency, so even if they are much lossier than the post modes they can be effectively ignored. In fact, the end of the box on the opposite side of the cavity from the post can be completely open to air and still the modes of the post retain high quality factors. This allows these reentrant cavities to be monolithic by simply machining from one side of a piece of metal (see section 2.2.4 for more information on fabrication). The electric field and magnetic field of the mode is shown in Figure 2.4. In this post mode, current flows up and down the post, resulting in maximum charge build-up at the top of the post which causes the electric field to be at a maximum and point radially outward at the top of the post.

In these re-entrant cavities, there are several parameters that can be controlled. First, the length of the post largely determines the frequency of the mode. This is convenient because

we can then run an aluminum or dielectric screw through the middle of the post to allow tuning of the post mode, or the posts can be physically shortened. Second, the cross-sectional area of the box can affect the quality factor of the cavity. Increasing this increases the surface to volume ratio, thereby decreasing surface losses, which is by far the dominant loss source for room temperature cavities and often the limiting loss source even when the cavity is superconducting. However, the cross-section becoming larger also lowers the frequency of the lossy box mode of the resonator, which can also be a dominant loss source in the system if it is too close. We then optimize this size to achieve the highest quality factors possible in the cavity. Cavity eigenmodes can be simulated with different parameters in computation microwave cavity solvers such as ANSYS Electronic Desktop or COMSOL.

2.2.2 Other Cavity Designs

Other cavity designs were tried and used for long periods of time before we discovered how to use the reentrant post cavity design and they possessed their own useful qualities. Shown in Figure 2.5a is linear chain of seven "flower" cavities. These are basically cylindrical cavities except that four corners are pinched. This design was originally inspired by an attempt to make YIG cavities and fundamental cavities simultaneously the same radius and frequency so that they fit uniformly on a square lattice, which is difficult since the YIG cavities use higher order modes (section 2.3). By pinching in the corners of the cavity, the frequency of the fundamental cavity could be raised while keeping the overall radius the same. In this lattice we implemented and tested the Hamiltonian tomography (section 2.5.3). Another type of cavity we tried was a cylindrical cavity with intentional disorder in one of the x or y direction in order to break the degeneracy between the two higher order modes in a cylindrical cavity (Figure 2.5b) This could make cavities that shift the phase of photons that pass through them by either 0 or 180 degrees. These could be implemented in some proposals [53]. Finally we employed some reentrant cavities with four posts shown in Figure

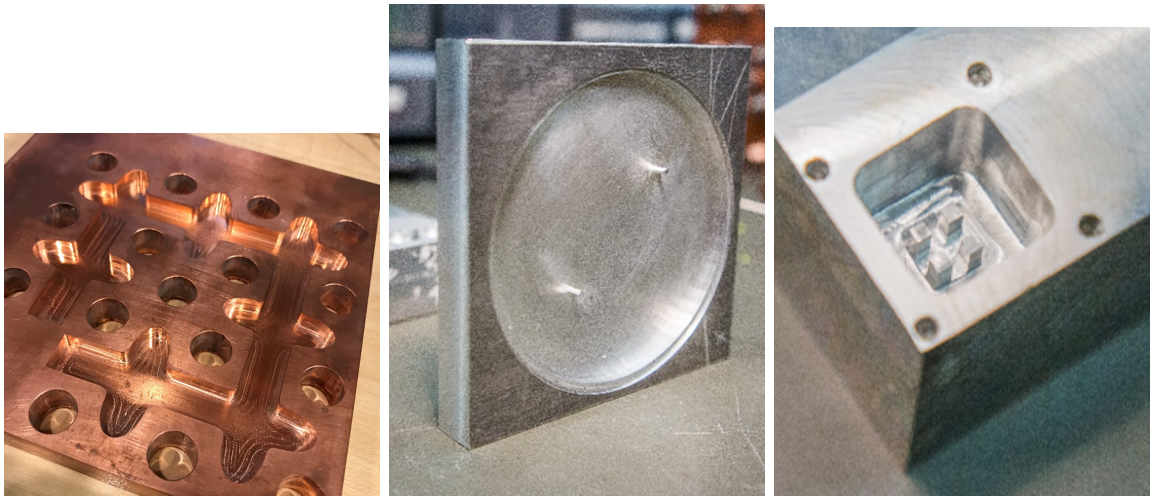

(a) (b) (c)

Figure 2.5: **Left.** "Flower" cavity design. Seven of the cavities are arranged in a 1D chain that wraps around the copper. **Middle.** Electric field simulation of one of the chiral YIG cavity modes. A video that shows the rotation as a function of time is available at https://youtu.be/gHoyFxkw9iQ. **Right.** Magnetic field of one of the chiral YIG cavity modes viewed from the top. The field at the center of the cavity rotates in time, coupling to the magnetic moment of the YIG.

2.5c that also had chiral modes, but the mode spacing with the other modes in the manifold was too small.

2.2.3 Material Effects and Cryogenics

There are several factors to consider when choosing the material to make the lattice. At room temperature, the primary concern is conductivity, thus making copper and aluminum ideal choices (silver has a slightly higher conductivity but much more expensive). Aluminum is easiest to machine though it has 61% the conductivity of copper. We used aluminum at room temperature for the lattices measured in this thesis.

After cooling the lattice to cryogenic temperatures in the dilution refrigerator, the choice on which material becomes more nuanced as many materials start superconducting. Since some of the lattice cavities require DC magnetic fields applied to ferrite crystals put inside them

(more details in chapter 3), type II superconductors with a high second critical field perform better, so that flux can penetrate the cavity but not destroy its superconducting properties. Niobium and Niobium titanium both can withstand high fields (~1800 Gauss H_{c1} and 4000 Gauss H_{c2} for high purity niobium [54]) before going normal. Niobium titanium has a larger critical field than niobium, but the differences proved negligible (more details in chapter 4).

2.2.4 Fabrication

All cavities and lattices were made using CNC milling. Some of the design decisions were constrained by the limitations of milling, most notably how small the cavities can be machines while maintaining structural stability of the post inside the cavities. Many of the prototypes were machined by myself at the student shop while the final versions were made by the company Zero Hour Parts.

2.3 Breaking Time Reversal Symmetry in Microwave Cavities

The first main step I took in building topological quantum materials out of light was designing a magnetic field that interacted strongly with microwave photons. Magnetic fields both break time reversal symmetry and induce interesting topological states. In chapter 3 I discuss how to make a magnetic field for photons in greater detail, but the essential requirement is that photons have to acquire extra, nontrivial (not a multiple of π) phase as they tunnel from site to site. In addition, in order to generate a uniform magnetic field of the right strength, the phase photons acquire from tunneling must be carefully controlled. A central innovation of my work was designing individual cavities that both strongly break time reversal symmetry and tune tunneling phases while maintaining high quality factors and a low density of states. This is accomplished by first making a cavity with chiral modes that are high quality factor

and isolated in energy, and then breaking the degeneracy between these two chiral cavity modes. To break the degeneracy, we couple the rotating modes of a cavity to a ferrite material called YIG (yttrium iron garnet) that has its own chiral modes. When a magnetic field is applied to YIG, the magnetic moment of the YIG sphere precesses at a frequency $f = \gamma B$, where γ is the gyromagnetic ratio 28 GHz/T and B is the DC field strength, similar to how an electron spin precesses in a magnetic field. This precession's chirality is set by the direction of the magnetic field and always has the same chirality as one of the cavity modes and the opposite of the other mode. Due to what amounts to a rotating wave approximation in real space, the YIG couples much more strongly to the cavity mode precessing with the same frequency.

I first achieved time-reversal symmetry breaking in cylindrical cavities. The first two excited states of a cylindrical cavity are chiral modes, though because they are degenerate the two modes can be described in a linear basis as well. This would make the two modes have identical structure but rotated $\frac{\pi}{2}$ (see Figure 2.2). Not only do these fields have a chiral modes, but the chiral modes have maximums of their magnetic field sitting at the center of the cavity (Figure 2.7) shows the magnetic field of a cylindrical cavity mode). The magnetic field at this location precesses at the cavity frequency. This allows us to place a YIG sphere at the center of the cavity to maximize the coupling between the YIG and the cavity without breaking the circular symmetry that is necessary for chiral modes. In Fig 2.6, we show the magnetic field dependence of the frequency of the circular modes (details on the measurement setup given in section 2.5.1). One of the modes shifts in frequency much more than the other as we tune the magnetic field, resulting in a splitting of 100 MHz. This splitting is effectively how much time reversal symmetry is broken in the cavities. We term the mode that interacts strongly with the YIG sphere the "bright" mode and the noninteracting mode the "dark" mode. The dark mode is particularly interesting since it does not hybridize with the YIG sphere and thus its quality factor is set only by the quality factor of the cavity (the YIG dielectric loss is small (quality factors of the YIG mode are ~3000 at room temperature at

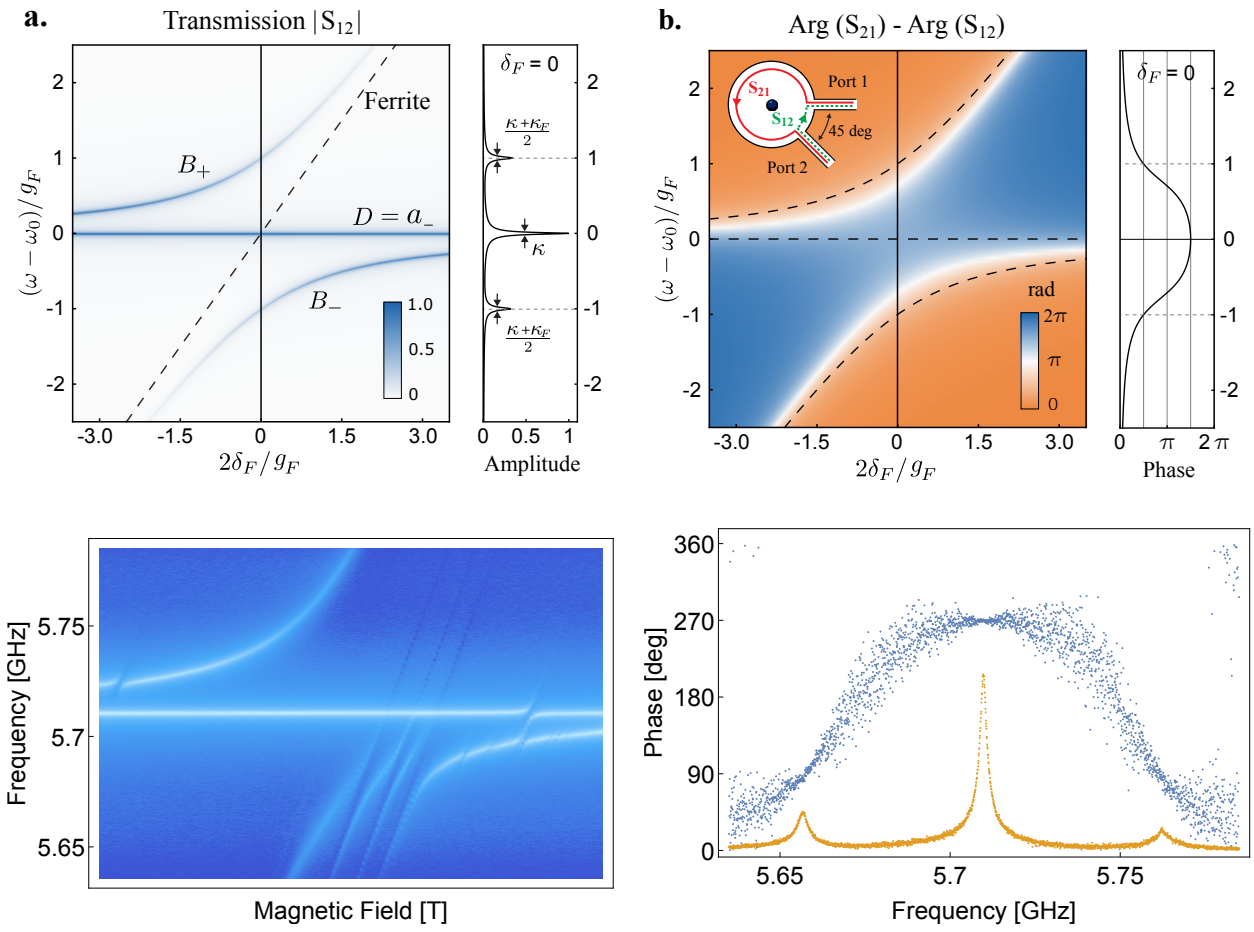

Figure 2.6: **a.** Predicted spectra of the YIG mode and the two chiral cavity modes as a function of magnetic field. The YIG mode interacts with a cavity mode of the same chirality, but does not interact with the mode of the opposite chirality. **b.** Simulated phase of transmission through a YIG cavity when the two ports are 45° apart. On resonance (the rightmost plot) the phase of the dark modes is exactly opposite the phase of the bright modes due to the opposite chirality. **c.** Measured transmission of a cylindrical cavity with a YIG sphere at its center as the magnetic field on the YIG sphere is swept. The cavity behaves as modeled except for the extra YIG modes interacting with the cavity at higher magnetic fields. **d.** The YIG is tuned into resonance with the cavity modes and two antennas are put into the cavity with a 45° angle between them. The phase is measured in blue and magnitude the magnitude is plotted in gold in order to show the frequency of the modes. At the mode frequencies, the two dark modes have a phase shift equal to twice the angle between the antennas, while the bright mode has the opposite phase, indicating opposite chirality. Figure a and b come from our paper theoretically proposing this model [3].

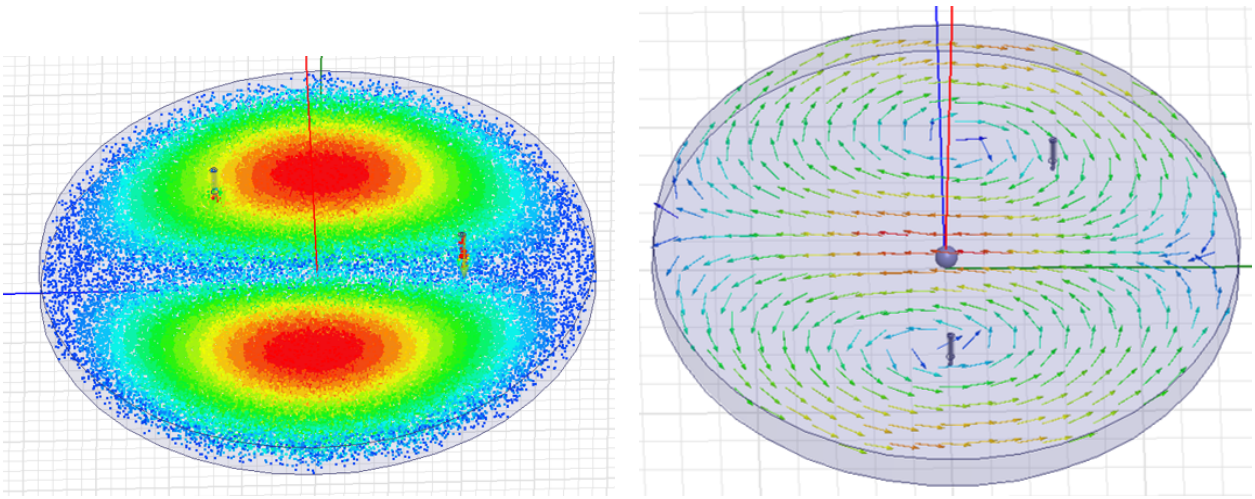

Figure 2.7: **a.** Simulated electric field of one of the second excited states of a cylindrical cavity.**b.** Simulated magnetic field of one of the second excited states of a cylindrical cavity. The magnetic field is strongest in the center.

our fields and frequencies [55]) and it turns out the mode itself is not that lossy at cryogenic temperatures. This is discussed in greater detail in chapter 4). We can also directly measure the chirality of the modes by measuring the phase of transmission through the cavity. Chiral cavity modes have a linear phase gradient (see Figure 2.2) as a function of the angle in the cavity, so we would expect to observe a transmission phase that is either equal to the angle between the measurement ports relative to the cavity center or 2π minus that angle. In Figure 2.6 we plot the phase as a function of frequency between two measurement ports that have a $\frac{\pi}{4}$ angle between them. In order to eliminate cable and connector phase, we measure S12 -S21 (transmission from port 1 to 2 minus transmission from port 2 to 1), so the actual phase plotted in Figure 2.6 is two times the actual phase. The phase observed for the dark mode is $\frac{3\pi}{2}$ while the phase observed for the hybridized dark modes is $\frac{\pi}{2}$, which is consistent with twice the angle between the ports. The main takeaway here is that we have created a high quality factor cavity mode that can be used to control the phase of microwave photons by breaking time reversal symmetry. The main limitation is the size of the splitting between the bright and dark modes, which is effectively how strong we have broken time reversal symmetry. This splitting is important because in order for the cavity to shift the phase of

the photon like we designed, we assume the photon only populates the dark mode of the cavity, which is only true if the splitting in the states is much larger than other parameters in the system, most notably the tunneling rate between cavity lattice sites or the interactions between photons, which are discussed in Section 2.4 and Chapter 5, respectively.

However, we needed to design a cavity that behaved similarly but was compatible with the re-entrant post cavities described earlier in this section. The excited manifold of the re-entrant post cavities is composed of two time-reversal symmetric chiral modes, but the maximum magnetic field position in these modes moves in the cavity as a function of time, making these cavities incompatible with coupling to a ferrite. Additionally, these modes are at approximately three times the frequency of the fundamental mode which causes other issues when trying to isolate the two modes in frequency. The goal then was to create a degenerate pair of chiral modes that had a stationary magnetic field maximum. One simple way to create extra modes in a cavity is to add more posts. Each additional post will add another mode. Adding a second post of the same length does not create a degenerate set of modes however, since the two posts couple to each other through the box mode of the cavity, and the resultant two modes are split in energy by twice this coupling. One of the modes is antisymmetric (the phase of the oscillations on each post are different by π radians) and the other is symmetric, analogous to two masses on spring coupled to each other. Adding a third post in a triangular pattern (as shown in Figure 2.4b) results in a more promising dispersion of modes. When the post modes couple to one another through the box modes, the spectrum of the post modes resolves into one lowest energy mode where all posts resonate in-phase, and two degenerate higher-energy modes. Since there is still a rotational symmetry in the system, these two degenerate modes have a rotational basis in which they can be measured. The field structure of these modes is shown in Figure 2.4b (electric field) and in Figure 2.4c (magnetic field) and animations are available in the supplemental materials online. The field's maximum hops from post to post either clockwise or counterclockwise as a function of time/phase.The magnetic field is not maximal at the cavity center, but exhibits sufficient

concentration to couple strongly to the YIG sphere; at resonance, the bright mode - ferrite coupling reaches 1.4 GHz.

In Figure 2.8, we show the magnetic field dependence of the frequency of the circular modes in three post cavities coupled to a YIG sphere placed in the center of the posts. One of the circular modes shifts in frequency more than the other as we tune the magnetic field, giving a maximum frequency separation in the cavities of ~400 MHz. Similar to the cylindrical cavity, the phase shift through the bright mode is the same and equal to two times the angle between the antennas, while the phase shift through the dark mode is 2Π minus the phase shift in the bright modes since this mode is orbiting with opposite chirality. The uniform oscillating mode is also shown on this plot at the lowest frequency. The phase shift through this mode is 0 since it has no spatial dependence on phase. The dark mode does interact to some degree with the YIG spheres in these types of cavities (much more than circular cylindrical cavities as shown in Figure 2.6). This is primarily because the modes of the resonators are not perfectly circularly polarized and because the bias field is not perfectly homogeneous. Additionally, the coupling to the YIG sphere is quite strong, making these effects easily observable as additional avoided crossings in Figure 2.8. At low temperatures we will couple the lattice to the dark mode since it will hybridize less with the YIG modes (cavity modes are higher Q when the cavity is superconducting). At room temperature it is convenient to couple to the bright, higher frequency YIG mode since it not only has similar Q to the dark mode, but also only has the one dark mode nearby in frequency. Also, since it is higher frequency, it allows the fundamental cavities to have less screw length protruding into the cavity and thus somewhat better quality factors.

I chose to work at 9.6 GHz since at this frequency I could maximize the coupling to the YIG sphere while not having the higher frequency modes of the YIG sphere complicate the cavity-YIG coupling (Figure 2.6 shows the higher order modes). Figure 2.9 summarizes the how the frequencies of the modes depend on geometry and the YIG sphere. The cavity we

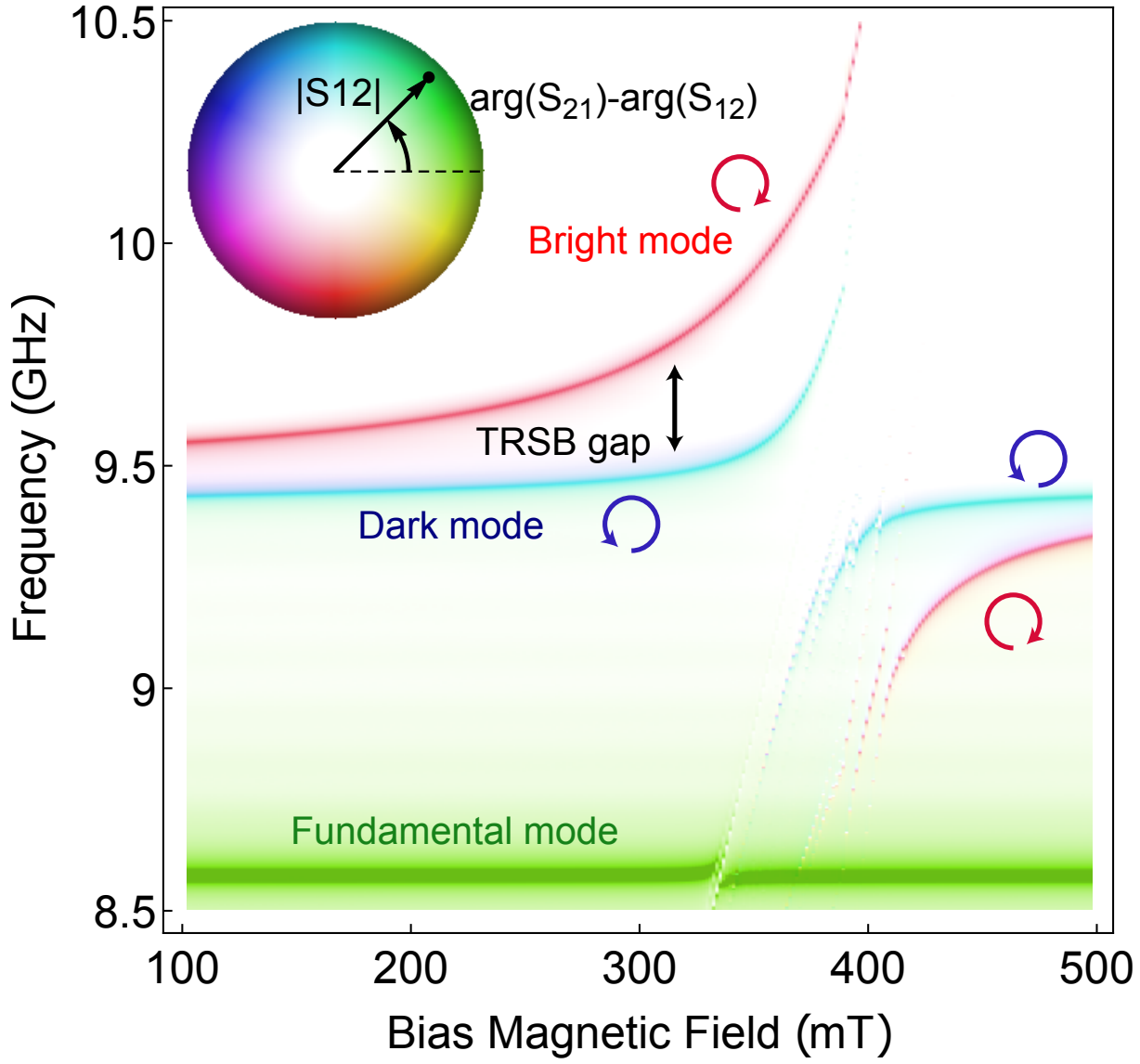

Figure 2.8: S_{12}-S_{21} Transmission between two antennas 45° apart in a single YIG cavity as a function of magnetic field. There is stronger coupling between the cavity mode with the same chirality as the YIG sphere. The largest frequency splitting is 446 MHz. The color indicates the phase shift a photon acquires in transmission. After subtracting the two different directions of transmission to eliminate phase noise from cables and impedance mismatches, one chiral mode has a phase shift of 90° while the other has a phase shift of −90°, indicating the modes are of opposite chirality. This picture comes from our paper [4].

ended up using for the rest of this thesis is the last column, the YIG cavity with 3 posts.

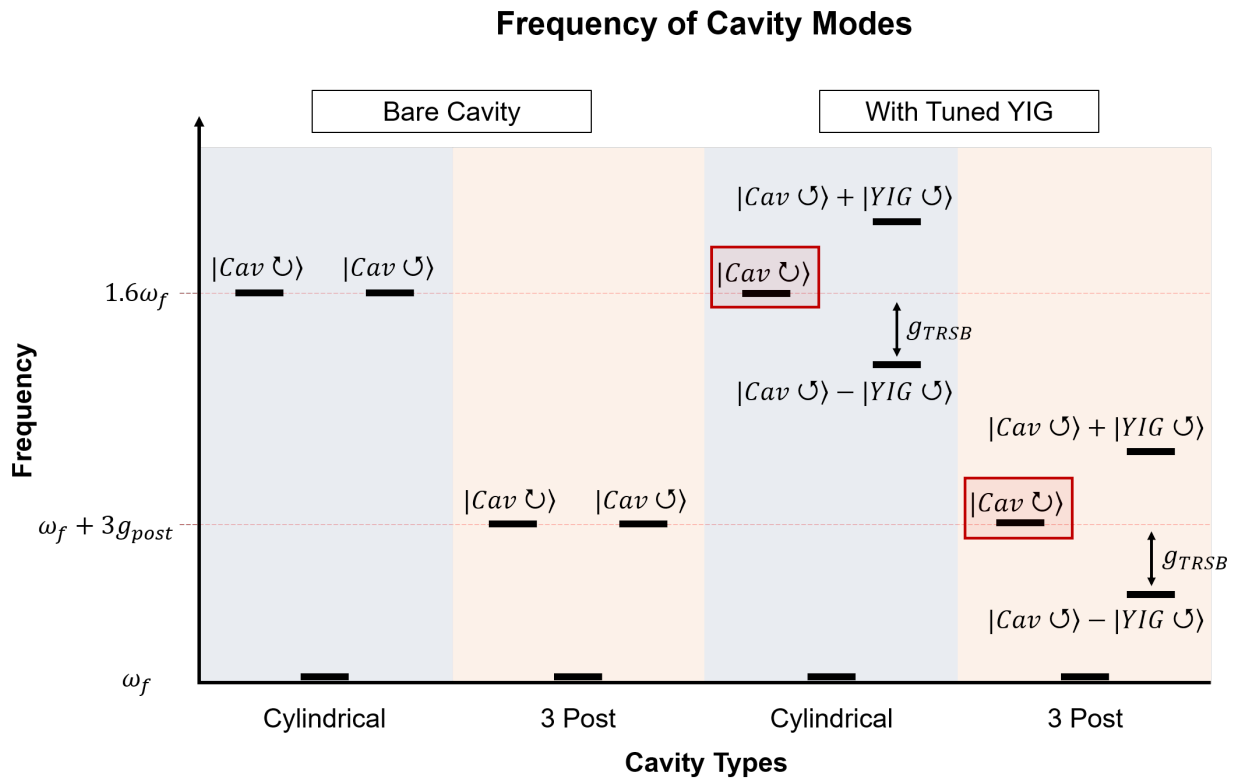

Figure 2.9: The fundamental and next highest excited manifold of modes for the four types of cavities discussed in the section. The two cavities on the left are the bare cavities- the lowest modes are the fundamental mode not used for the chiral cavities, then two excited modes are degenerate and have opposite chirality. The cylindrical cavity mode spacing is determined by zeros of the Bessel functions, while the 3 post cavity mode spacing is determined by the coupling between the three posts g_{post} (the three posts are essentially three separate resonators hybridizing equally to each other), or essentially how close they are to each other. When the YIG sphere is added and tuned to the excited manifold frequency, it hybridizes with the mode of the same chirality and splits it in energy by g_{TRSB} in both cases. Left at the original excited manifold frequency is a mode of the opposite chirality, which is the chiral, time-reversal symmetry broken mode we needed to engineer a magnetic field.

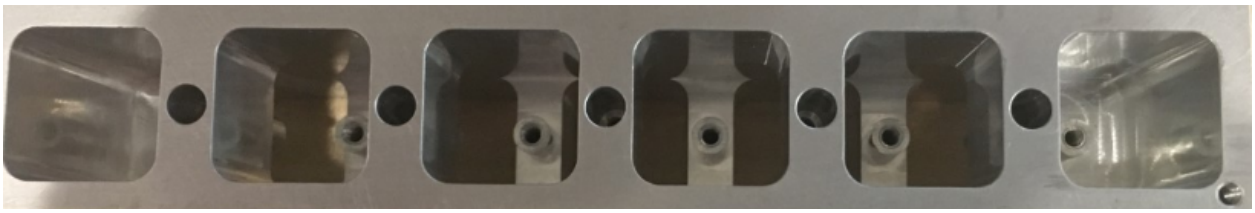

Figure 2.10: Cavities coupled to each other in a 1D lattice. In this particular version, there are posts in both the cavities and the couplers. Tuning the post lengths with a screw allows both the frequency of the cavity and the coupling between sites to be tuned.

2.4 Tunnel Coupling

The cavities are coupled by drilling a hole from the other side of the lattice in between the lattice sites. As long as the couplers' cross-sectional areas are small enough so that frequency of the mode in the couplers is much higher than the lattice site modes, then negligible loss is introduced from the couplers. The couplers can be thought of as higher frequency resonators between neighboring cavities that couple the cavities with a strength $\frac{g^2}{\Delta}$, where g is the direct coupling of the cavities to the coupler and Δ is the detuning. Thus one way to increase the coupling between cavities is to bring the posts of the cavities closer together which increases g. Similarly, any method that concentrates the mode of the coupler closer to the posts will increase the coupling. To increase Δ, we can either increase the size of the coupler or add a post in the coupler so that the coupler has its own post mode. By carefully selecting the length of this post, we can keep the couplers off-resonant to the lattice, but decrease Δ significantly for higher coupling. We use a tapped screw as the post so that we can tune the coupling between lattice sites. The screws allow the frequency of the coupling to be tuned from 20 MHz to 100 MHz, though to keep the band structure of our lattice comfortably within the 400 MHz splitting between the chiral YIG cavity modes (so that the YIG mode with opposite chirality does not hybridize with any lattice modes), we tuned the coupling in the room temperature lattices to 30 MHz.

For the cryogenic lattice, we remove the tuning screws and set the tunneling rate by the size

of the coupler, since screws can be a loss source at higher quality factors. Since the YIG splitting is smaller (discussed more in chapter 4), the coupling rate is lowered to 15 MHz.

2.5 Measuring Cavities

2.5.1 Microwave Cavity Measurements

When measuring a microwave cavity, several factors must be considered. For all of the cavities in this thesis, the method of coupling is the dipole antenna. Essentially this is just a single wire (antenna) that protrudes into the cavity and couples to the cavity mode by aligning with the electric field of the cavity. The coupling is determined by how much the antenna aligns with the electric field of the cavity.

Getting the right coupling to the cavity can be a challenge. If the coupling is too high, then the cavity quality factor and frequency can be affected by the antenna. If the coupling is too low, then the signal to noise will not be high enough to learn anything about the resonator. Typically the antenna will be put on top of cavity where the electric field profile is decaying exponentially. This makes the coupling to the cavity highly sensitive to the antenna length. Furthermore, in order to achieve the desired couplings (in the YIG cavities), the antenna must be so long that the antenna will support its own modes near the cavity frequency. These modes are extremely lossy and can spoil the quality factor of the cavity.

2.5.2 Setup of the Lattice Measurements

Every cavity has a microwave antenna weakly coupled to it from the top, so that the antenna does not add significant loss or shift the frequency of the resonator. The length of all the antennas are kept the same so that the coupling to each cavity is the same. Each antenna

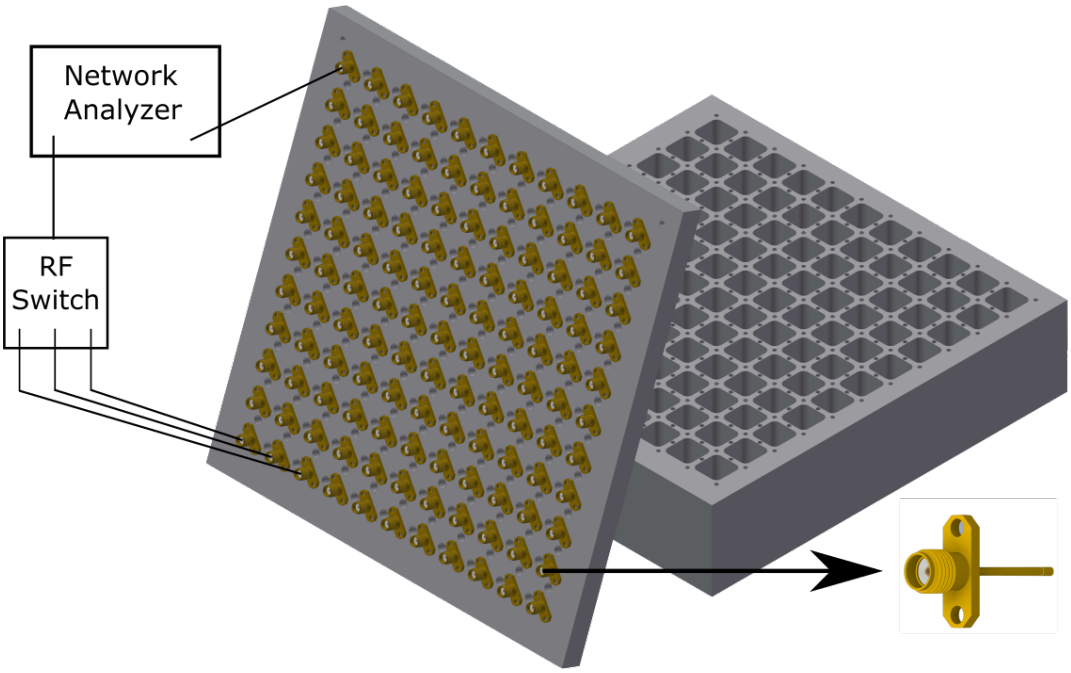

Figure 2.11: The lattice is shown on the right. A lid for the lattice is made so that one of the gold-colored antennas is connected to every lattice site. These antennas are connected through an RF switch to the network analyzer so that arbitrary transmission between pairs of sites can be measured.

is then connected to a vector network analyzer through a switch network so that we can measure the transmission between any two cavities. We can measure reflection off any site as well, though reflection measurements are more sensitive to impedance mismatches in the cables and switches. Effectively, allows us to perform measurements akin to an scanning tunneling microscope, for microwave metamaterials.

Using the same network of antennas, we can pulse the lattice and measure the response as a function of time. For the room temperature lattice we create the pulse by mixing a 9.6 GHz sine wave signal with a 75 ns long Gaussian pulse (50 ns for the beam-splitter experiment). The pulse must be short enough in the time domain so that it does not interfere with itself, but long enough so that the pulse is not so wide in frequency space that it strongly excites the bulk bands. We use a shorter pulse for the wall data since the pulse takes less time to come back to the originally excited cavity. To measure the pulse, we first use an IQ mixer to

mix the signal coming out of the measured cavity with the 9.6 GHz oscillator to make the signal near DC. We then measure the IQ output on an oscilloscope to get both the phase and the amplitude of the response as a function of time.

2.5.3 Hamiltonian Tomography

After all the lattice sites are coupled, measuring the individual properties of each lattice site becomes difficult because all of the modes hybridize. This is important because disorder enters the lattice through fluctuations in the individual lattice site frequencies (and couplings). Since there are so many sites and therefore modes, it is exceedingly difficult to decipher where disorder is in the lattice from reflection measurements from different sites. If one tried to fit the spectrum of N peaks (N is the number of lattice sites), there would be a number of fitting parameters equal to the number of lattice sites plus the number of couplers ($N + 2(\sqrt{N} - 1)\sqrt{N} = 3N - 2\sqrt{N}$, or 341 for the room temperature lattice). In addition, there would be many degenerate solutions. In practice, we detune neighboring lattice sites effectively decoupling lattice sites one at a time so that we can measure the uncoupled resonator frequency. To measure tunneling rates, we detune all neighboring lattice sites except for two cavities, tune them into resonance, and then measure the splitting between the two cavities. This splitting is equal to $2t$. This method is functional, but especially tedious using the cryogenic lattice. We developed a more elegant solution to deciphering the individual site frequencies of a coupled lattice that uses reflection measurements to determine lattice site frequencies and transmission measurements to measure tunneling frequencies [56]. Much of the detail behind the technique can be found in the paper, but I want to make a few remarks on the practicality of using this technique as well as discuss potential methods for making it work in experiments.

A key component of this technique relies on integrating the area under the reflection or trans-

mission responses. Essentially, the weighted average of the frequency f and the response R ($\int_0^\infty Rdf$) gives the uncoupled frequency of the site being measured for reflection spectra, and the direct coupling between the two sites being measured for a transmission spectra. However, this technique only works if the off-resonant background signal is much smaller than the total response of the lattice modes. In practice, this is often not the case, since there are typically some types of impedance mismatch between cables and couplers, which leads to frequency-dependent background noise. These impedance mismatches are particularly troublesome for reflective measurements compared to transmission measurements. In reflection measurements, all of the input power is reflected off the sample off-resonance, so the background of the measurement is changed when some of the input power is absorbed by effective cavities created by impedance mismatches. On the other hand, transmission measurements have a background of zero power being transmitted, which means that the background of transmission measurements are mostly flat even if there are impedance mismatches. The backgrounds of reflection measurements can be fit out to minimize the error on the lattice measurement. We found that with sufficient calibration, the technique is useful to measure the bare frequency of the fundamental cavities. However, in the YIG cavities a different problem emerged. The mode of the YIG cavity is much more localized near the posts than the modes of the fundamental cavities, so the antennas that couple to the YIG cavities are required to be longer to get a decent signal. The longer antennas in the YIG cavities then couple directly to the neighboring fundamental cavities in the lattice (in fact they couple about equally to the YIG cavity and the neighboring fundamental cavities). This direct coupling to the neighboring cavities makes it difficult to isolate the uncoupled frequency of the YIG cavity. The amount the antenna couples to each cavity can be measured and new procedures can be done to back out the uncoupled frequency, but this in combination with the noisy backgrounds led us to temporarily abandon this technique in tuning the lattice.

Beyond improving the fitting of the background and the coupling of the antennas, another

step can be done to make Hamiltonian tomography more useful. One technique I tried was putting two antennas on a lattice site and then measuring transmission from one site to itself. This greatly lessens the background noise, except if the antennas have a direct coupling to each other. The direct coupling would add a background on the transmission measurement. Avoiding this direct coupling is not trivial since being in the same cavity naturally forces the antenna in close proximity, though there are many ways of coupling to the cavity and perhaps one way could be found that minimizes this problem.

CHAPTER 3

CHERN INSULATOR OF MICROWAVE PHOTONS

This section is based off the work published in our paper [4], with added technical and theoretical details.

3.1 Introduction

The main challenge we wanted to overcome in this thesis was to develop a material that simultaneously has both magnetic field and inter-particle interactions for microwave photons. The first step we took was to engineer the magnetic field interaction in such a way that it would be compatible with adding inter-particle interactions afterward. With that in mind, we designed our lattice sites in such a way that they can work cryogenically (Chapter 4) and supported coupling to transmon qubits (Chapter 5). First I will discuss theoretically how to make a magnetic field for photons, even though photons have no charge. Then I will show how to implement that theoretical model with 3D microwave cavities. Next I will show in detail the topological effects that emerge when a magnetic field is applied to particles in a lattice, taking advantage of the site-by-site resolution we have with our cm-scale particles. This system is directly compatible with the cQED toolbox [3], as it is composed only of a seamless machined-aluminum 3D resonator array with one Yttrium-Iron-Garnet (YIG) sphere and one Neodymium magnet per plaquette, all of which function cryogenically. Furthermore, the reentrant style of cavities have been successfully coupled to transmons with great results [52].

3.2 Creating an Artificial Magnetic Field for Light

In order to understand how to create an effective magnetic field for a photon, we first have to look at what a magnetic field does to a charged particle, especially in two dimensions. The charged particle is trapped in a cyclotron orbit, and the particle's wavefunction picks up extra phase proportional to the magnetic flux the particle's path encloses:

$$\Delta\phi = \frac{q}{\hbar}\int_A B \cdot \, dr^2 \; = \frac{q}{h}\Phi \tag{3.1}$$

where q is the particle charge, B is the magnetic field, and Φ is the enclosed flux. This is known as the Aharonov-Bohm effect. This relationship is important because it also works inversely- if a particle acquires additional phase when it travels in a closed loop, there is an effective magnetic field acting on the particle. The challenge then becomes finding a way to control the phase of photons as they move throughout the lattice. In Chapter 2 we describe how we make cavities that can shift the phase of photons, and in Figure 3.1a we show how these cavity sites can be patterned so that no matter what loop a particle moves in, the flux per area the particle encloses is the same, which results in a uniform magnetic field for the photons. In a lattice, by measuring the phase acquired when a particle travels around the smallest closed loop (known as the plaquette) in the material, we can immediately calculate the magnetic field the photons experience (Equation 3.3).

Magnetic fields cause nontrivial topology, as can be seen intuitively in a two-dimensional electron gas. Applying a magnetic field to the gas localizes electrons in the bulk into cyclotron orbits. These tightly localized electrons are insulating. However, near the edge of the material, the electrons try to move in the cyclotron orbits, but bounce off the potential barrier of the edge, resulting in a traveling mode of the electron as it skips along the edge. These modes along the edge of the material are conducting, and they only conduct with one

chirality, which is set by the direction of the magnetic field. These modes are resistant to backscattering and disorder, since there are no modes of the opposite chirality supported by the system. The insulating bulk combined with a conducting edge is a key hallmark of a topological insulator.

In this chapter, we build a Chern insulator equivalent to a quarter flux Hofstadter model. The typical form of this Hamiltonian for this model is the following:

$$H = -t \sum_{\mu,\nu} a_{\mu,\nu} a^{\dagger}_{\mu,\nu+1} + a_{\mu,\nu} a^{\dagger}_{\mu+1,\nu} e^{i\alpha\nu} + a_{\mu,\nu+1} a^{\dagger}_{\mu,\nu} + a_{\mu+1,\nu} a^{\dagger}_{\mu,\nu} e^{-i\alpha\nu} \tag{3.2}$$

with a resulting magnetic field of

$$B = \frac{\alpha}{A} \frac{h}{q_e^2} \tag{3.3}$$

This model is one convenient way in which to generate a uniform phase per plaquette that has been successful in systems in which the tunnel coupling phase is controllable. As will be explained in section 2.3, we create a similar Hamiltonian but with a different gauge since we do not directly control the phase on the tunneling term, but rather use interspersed chiral cavities to generate the Berry phase.

3.3 Experimental Setup

To implement a quarter-flux Hofstadter lattice, we build upon the design described in [3]. A central innovation of this work is that while the Peierl's phase which encodes the synthetic gauge field is typically encoded in the tunnel-coupling between lattice sites, in practice the phase can arise from the spatial structure of the sites themselves rather than manipulation

of the tunnel couplers [43, 57]. We engineered the on-site Wannier function of every fourth lattice site to exhibit a 2π phase winding. This ensures that every plaquette contains a phase-engineered site, as shown in Figure 3.1a, and thereby induces a flux per plaquette of $\alpha = \frac{1}{4}$.

The meta-material is milled into a block of aluminum (see Figure 3.1b and Section 2.2.4 for more details) and is composed of three components- (i) fundamental mode cavities; (ii) chiral cavities; and (iii) evanescent couplers. The cavity design (Figure 3.1c) enables machining of the structure from only two sides, and completely removes seam-loss as a source of Q-reduction [52] (see section 2.2.1). Lattice sites are either a single post coaxial resonators oscillating in their fundamental mode with a spatially uniform phase profile, or are three post coaxial resonators with a chiral phase profile designed to produce a synthetic gauge field (section 2.3). The final ingredient is the couplers, which induce the tunneling term in the Hofstadter Hamiltonian (Figure 3.1c). The chiral cavities are designed so that a photon tunneling into- and subsequently out-of- the cavity acquires a phase equal to the angle between input and output arms. When the lattice is arranged as shown in Figure 3.1, a photon traveling in the smallest closed loop (plaquette) acquires a $\frac{\pi}{2}$ geometric phase.

In the fundamental mode cavities, a single post protrudes into an otherwise empty rectangular box. The length of the post sets the frequency of the resonator's fundamental mode to 9.560 GHz (to within 1 MHz), with the next mode at approximately at twice this frequency (see SI section 2.4). The side lengths of the box ensures that its cutoff frequency is higher than the post-mode, resulting in localization of the post-mode even without a lid on the resonator, with a mode-Q determined by the length of the cylinder, until surface-losses dominate.

The second type of cavity exhibits modes whose phase depends on the location in the cavity. This chiral cavity is structurally similar to the fundamental coaxial cavity but with three equal-length posts arranged in an equilateral triangle at the center of the cavity, instead

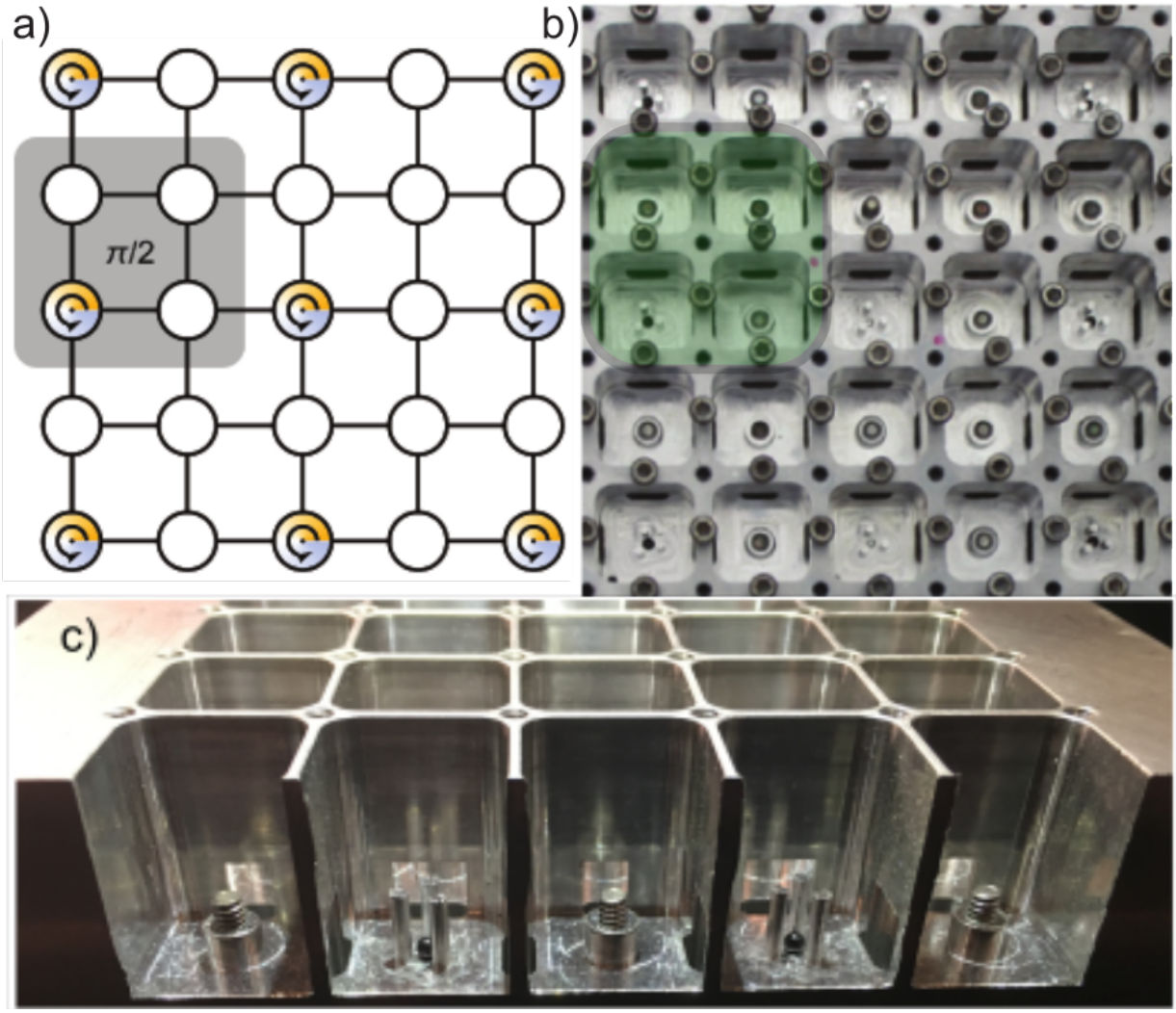

Figure 3.1: Schematic and photograph of microwave Chern insulator lattice. **a.** Schematic of the cavity layout. The white circles denote cavities that do not shift the phase of a photon passing through them, while the cavities with the arrows shift the phase depending on the physical angle between the couplers. This layout guarantees phase of $\frac{\pi}{2}$ per plaquette. **b.**Photograph of a 5x5 section of the lattice measured in the data presented in the paper. The lattice-sites are each tuned to 9.560 GHz $\pm$1 MHz, and coupled evanescently tunnel-coupled with hopping rate 30 MHz $\pm$1 MHz. The typical resonator quality factor for fundamental cavities is $Q = 3000$ and for the YIG cavities is $Q = 1500$. The lattice spacing is 1.96 cm, resulting in a total edge-to-edge (including outer walls) lattice dimension of 24.0 cm. **c.** Side profile of a 5x5 lattice cut so that both types of cavities are visible. The 2nd and 4th cavities are the phase shifting YIG cavities, while the 1st, 3rd and 5th cavities are the fundamental cavities. The couplers are visible in between the cavities as gaps in the cavity walls. They are milled from the opposite side of the lattice as the cavities. This picture comes from our paper [4].

of a single post (Figure 3.1c). These three closely spaced posts constitute three coupled degenerate resonators, and hence behave as a three-site tight-binding model with periodic boundary conditions. The result is one (quasi-momentum $q = 0$) mode in which all posts oscillate with the same phase, and two degenerate modes at a higher frequency (1 GHz higher in this lattice), at $q = \pm\frac{2\pi}{3}$; the electric charge accumulation in these latter two modes travels from post-to-post clockwise or anti-clockwise, respectively.

To break the time-reversal symmetry of the lattice and thereby induce a chirality in the system, it is essential that only one of the two degenerate modes at $|q| = \frac{2\pi}{3}$ couples to the lattice bands. To achieve this, a 1mm YIG sphere is inserted between the three posts (Figure 3.1c). When a DC magnetic field B_{DC} is applied to the YIG, it behaves as a macroscopic electron spin whose the magnetic moment precesses at the Larmor frequency $\omega_l = \mu_B B_{DC}$, and with a handedness set by the direction of the magnetic field ($\mu_B = 28$MHz/mT is the Bohr Magneton). When the YIG sphere is installed between the three-posts of the cavity, where the microwave magnetic field is strongest, the precessing magnetic moment couples strongly to cavity mode which co-rotates ($q = \frac{2\pi}{3}$), and weakly to the one which counter-rotates ($q = -\frac{2\pi}{3}$). Figure 2.8 shows the observed behavior of the $q = \pm\frac{2\pi}{3}$ modes as the DC magnetic field is varied, tuning the YIG frequency through the bare $|q| = \frac{2\pi}{3}$ mode frequency: the YIG induces a large avoided crossing with the co-rotating "bright" mode, a smaller asymmetry-induced avoided crossing in the counter-rotating "dark mode". Fine adjustment of the magnetic field strength can further be used to tune the frequency of the YIG cavities.

To probe the spatial structure of the chiral modes, we insert two antennae into one of the chiral cavities, separated by 45°. Figure 2.8 shows the observed phase difference between exciting one and measuring the other, and the reverse, indicating that the "dark" mode exhibits a phase-difference of 90°, while the "bright" mode exhibits a difference of -90°, consistent with their opposite chiralities.

To build a T-broken model, our engineered Hamiltonian must employ *only one* of these two chiral modes; accordingly, the "dark"-"bright" mode-splitting of $350 - 400$ MHz (depending on B_{DC}) sets the spectral domain into which the engineered Chern-band structure must fit. While the "dark" mode is the better choice in a superconducting resonator, YIG loss is much larger than the bare resonator loss. In the room temperature case technical concerns make the "bright" mode preferable for lattice engineering since it only has modes below it and none above it while maintaining the same quality factor.

The lattice sites are tunnel-coupled by milling out slots between them; because the lowest mode of these slots is above the cutoff of the lattice, these slots couple sites together without inducing radiative loss. The width and depth of the couplers set the tunneling energy, which we tune with a screw (see Figure 2.4) to 30 MHz with precision ± 1 MHz, in accordance with the requirement that the total-band-structure be narrower than the minimum 350 MHz "dark"-"bright" splitting.

3.4 Assembling the Lattice to Create a Uniform Field

Using these cavities, we create an 11x11 lattice (Figure 3.2 arranged in the pattern shown in Figure 3.1a, where the white circles are fundamental cavities and the colored cavities are the YIG cavities. This arrangement causes any plaquette traced in the lattice to acquire a flux per area of $\frac{1}{4}$. We can simulate our lattice using a tight binding model with the appropriate phase added into tunneling rates (see Appendix B for code), both with continuous boundary conditions and as an exact 11x11 lattice. The continuous boundary condition simulation is useful to calculate a band structure, as shown in Figure 3.3.

Next we calculate reflection measurements as a function of frequency off different sites of an 11x11 lattice. We first calculate the reflection off site (5,5), a cavity in the bulk of the lattice. This response is plotted in gold in Figure 3.4. The four bulk bands form symmetrically

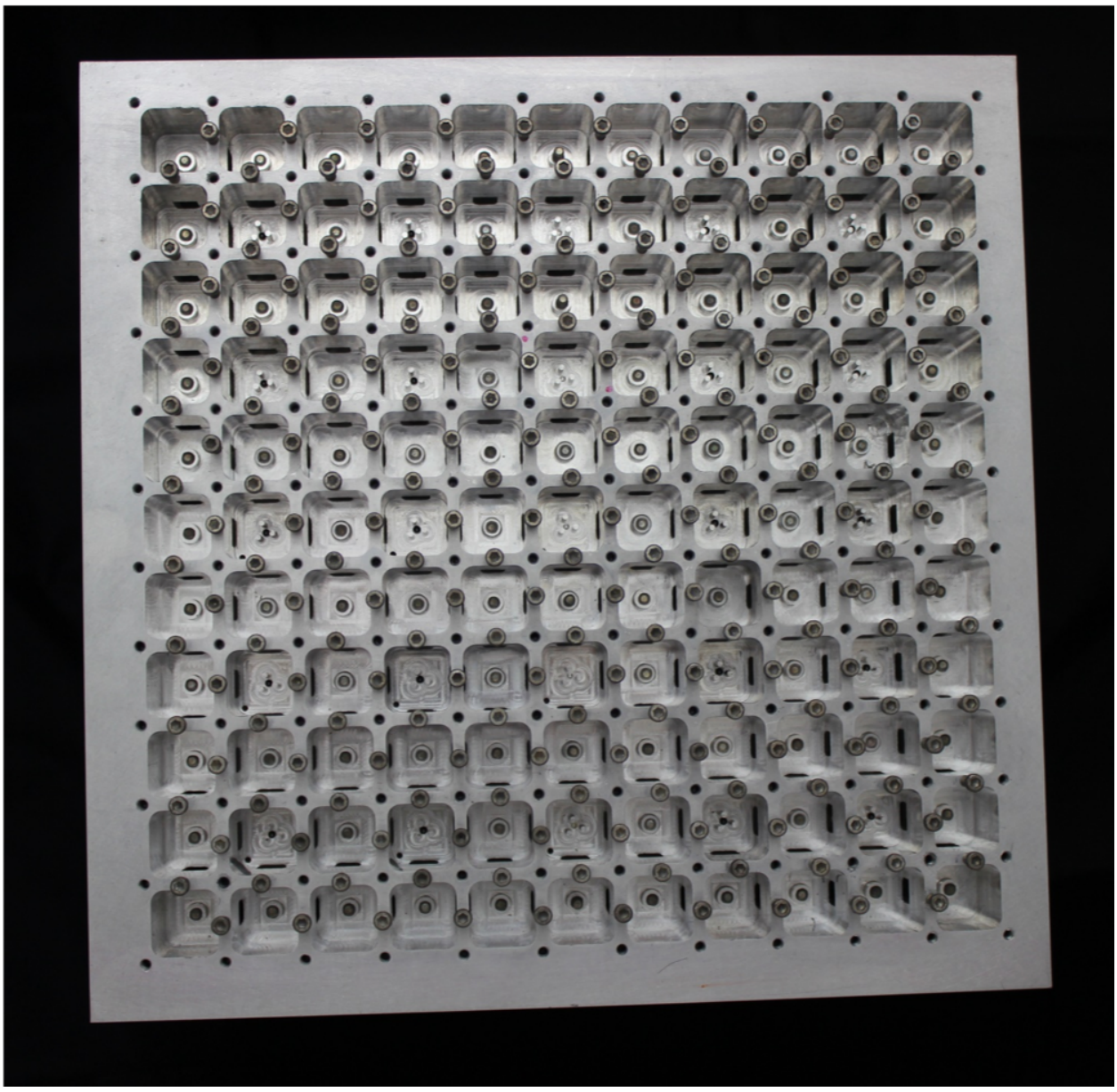

Figure 3.2: 11x11 Lattice from which the rest of the data in the section is taken from.

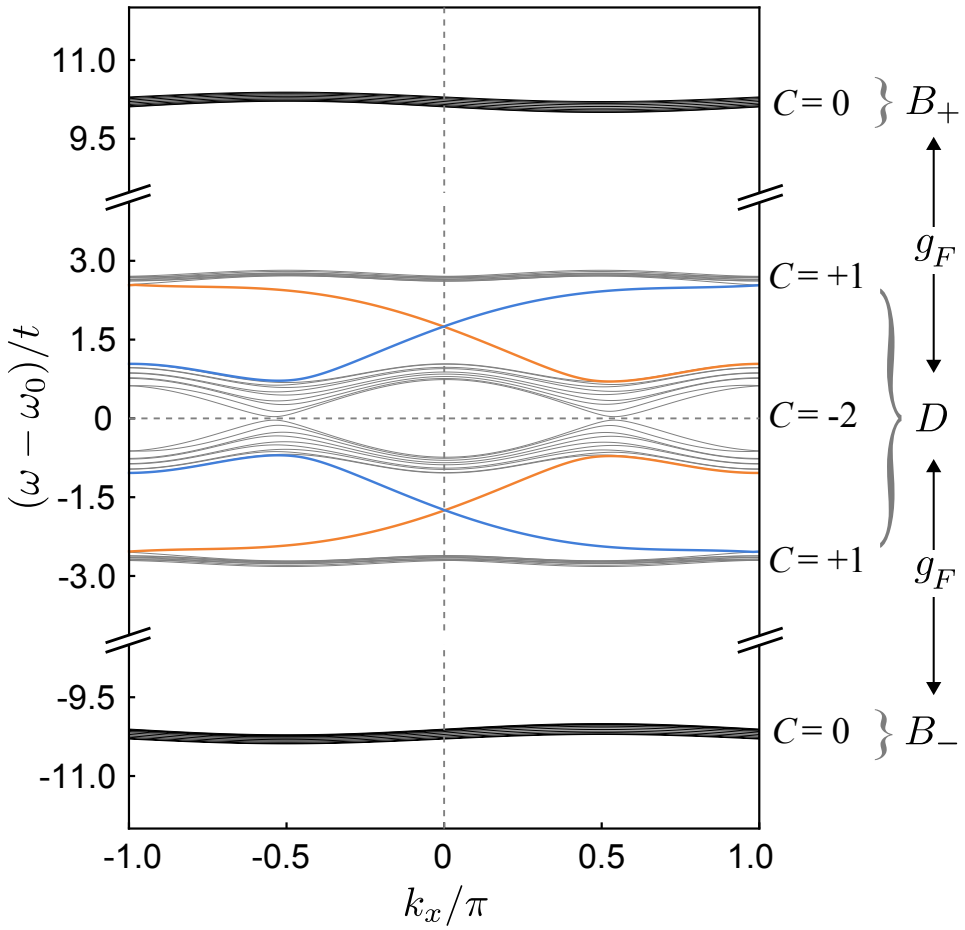

Figure 3.3: Band structure of the Hamiltonian in equation 3.2 calculated using periodic boundary conditions in the x direction, so that there are two edges of the system parallel to the x direction. The higher and lower black bands result from the bright modes in the YIG cavities and are detuned in frequency enough so that they do not appreciably affect the lattice band structure. The four grey bands are the bulk bands of the lattice. In the gap between the bulk bands are where the edge states of the system. The two colors correspond to the top and the bottom edges. The slopes of the chiral modes indicate the direction the modes propagate. On each edge, the modes going one direction are at a different energy than the modes going the opposite. This picture comes from our paper [4].

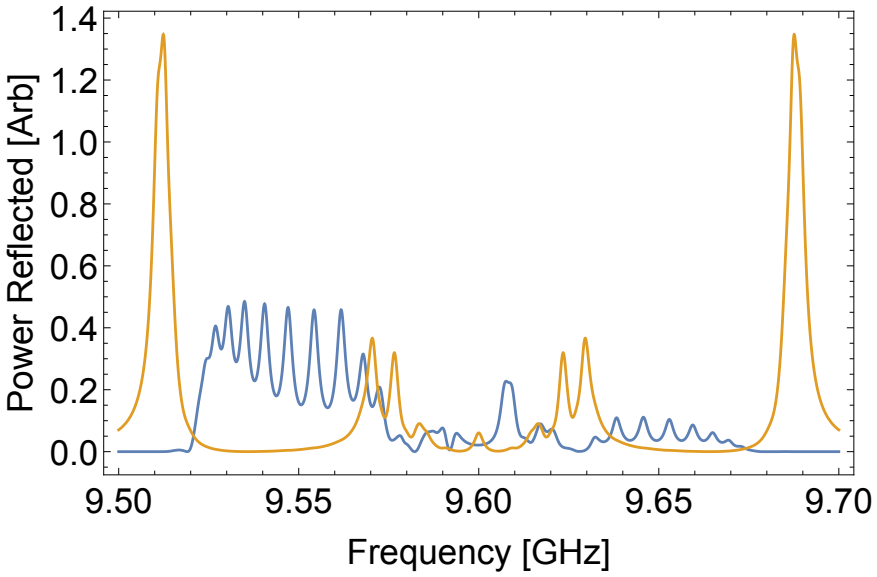

Figure 3.4: Simulated transmission measurements through an 11x11 Chern insulator with the Hamiltonian we are building. The gold curve is the reflection off the (5,5) bulk site, and the blue is transmission from the (1,1) edge site to the (1,10) edge site. The edge modes can be seen in the gap between the bulk bands. This picture comes from our paper [4].

around the bare cavity frequency (9.6 GHz), with two large gaps near 9.55 and 9.65 GHz. When we calculate the transmission through edge site cavity (1,1) to anothe edge site cavity (1,10), we see that there are edge modes located in the band gap of the bulk modes. In fact, the loss in the system shows that the chirality of the upper edge band is different than the lower edge band. One chiral path along the edge takes a much shorter route than the other direction, which means that fewer photons are lost in transit and the transmission for that direction is greater. In order to see that these modes are localized to the edge, we instead excite an edge cavity in the band gap and see the response of the lattice as a function of spatial position. This is shown in Figure 3.5. The red line is the excitation frequency and the plots on the right show the response of the lattice at that frequency when the (1,1) edge cavity is excited. Here the difference in the chirality between the upper and lower band is more clear. These chiral edge modes are hallmarks that indicate the particles are under the influence of a magnetic field.

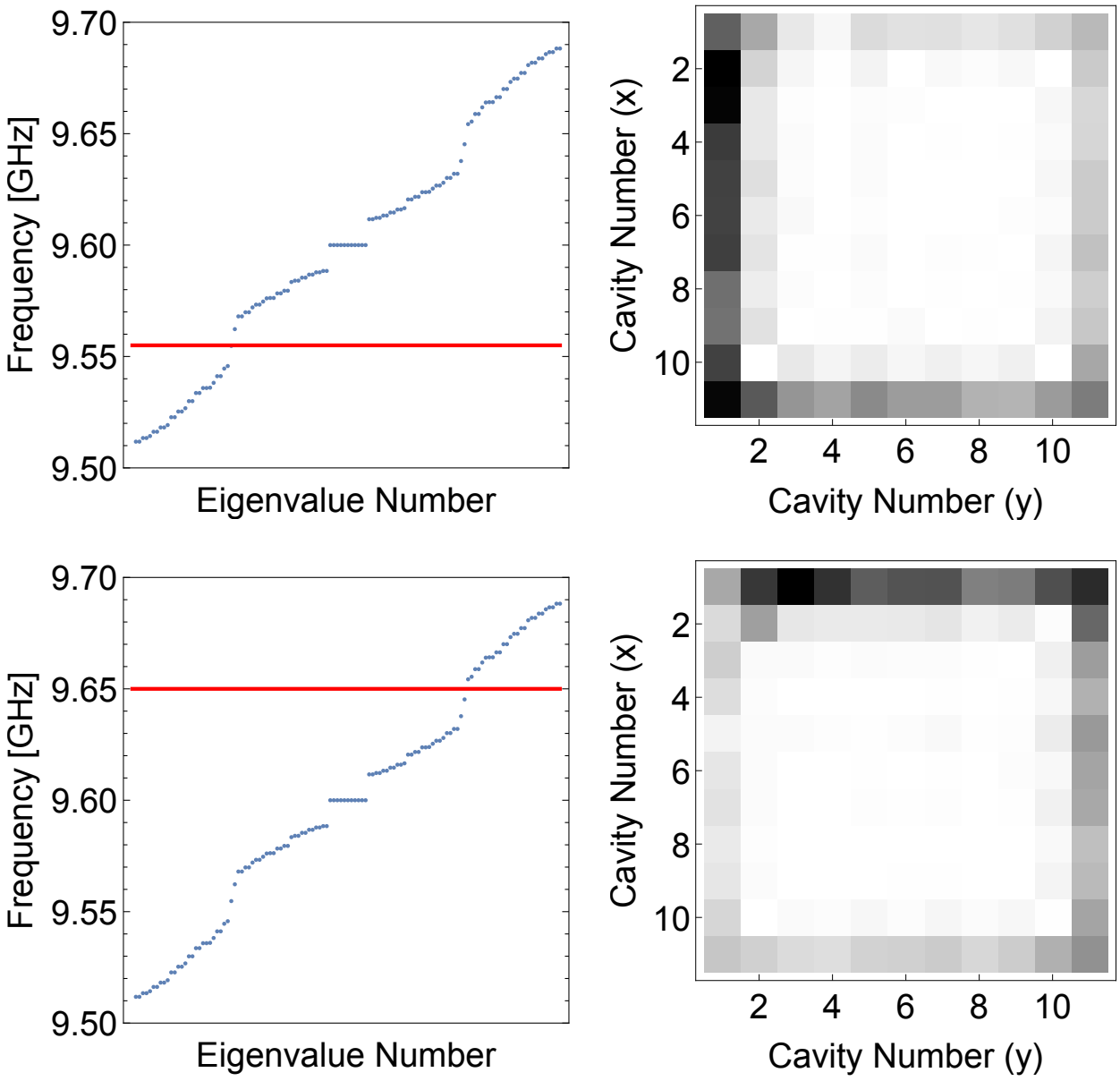

Figure 3.5: **Top.** Spatial response of the lattice when cavity (1,1) is excited at a frequency of 9.555 GHz. The mode is localized to the edge and counterclockwise chiral. **Bottom** Spatial response of the lattice when cavity (1,1) is excited at a frequency of 9.65 GHz. The mode is localized to the edge and clockwise chiral. This picture comes from our paper [4].

3.5 Spectral Properties of a Microwave Chern Insulator

A defining characteristic of a topologically non-trivial band-structure is the presence of an insulating bulk and conducting edges [58]. To demonstrate that our microwave lattice exhibits these properties, we probe it spectroscopically by placing a dipole antenna into each cavity. Figure 3.6a shows a typical transmission spectrum between bulk lattice sites in an 11x11 lattice (pictured in Figure 3.2). We observe energy gaps in the bulk response, within which the edge-localized channels reside, consistent with the computed band structure [3] shown in Figure 3.6b. The chirality of the edge channels results in an asymmetric edge-edge response in the band gaps: the edge modes in the lower- and upper- gaps have opposite group velocities and finite damping, so the accrued decay is smaller when the excitation travels the "short way" versus the "long way".

When the system is excited in the bulk within the band-gap, we observe a localized response as shown in Figure 3.7a, resulting from the absence of resonant modes to excite. On the other hand, when the system is excited on its edge within the band-gap, we observe the delocalized response shown in Figure 3.7b), resulting from the presence of the chiral edge channel within the bulk energy-gap. Decay in the lattice allows us to observe the chirality of the edge mode in the steady state response; at 9.6 GHz, the channel travels counterclockwise, as anticipated from the band structure in Figure 3.6b.

We Fourier transform the complex transmission as a function of position to directly measure the bulk band structure of the lattice. The 2D projection of this band structure is what is plotted in blue in Figure 3.6b.

The site-resolved probes accessible in our system enable us to directly access, for the first time, the dispersion of the edge channel, which we achieve by probing the system edge within the bulk energy gap and measuring the phase accrued per lattice site as a function of frequency (See SI 3.6). Figure 3.6c shows the observed dispersion, overlaid with the

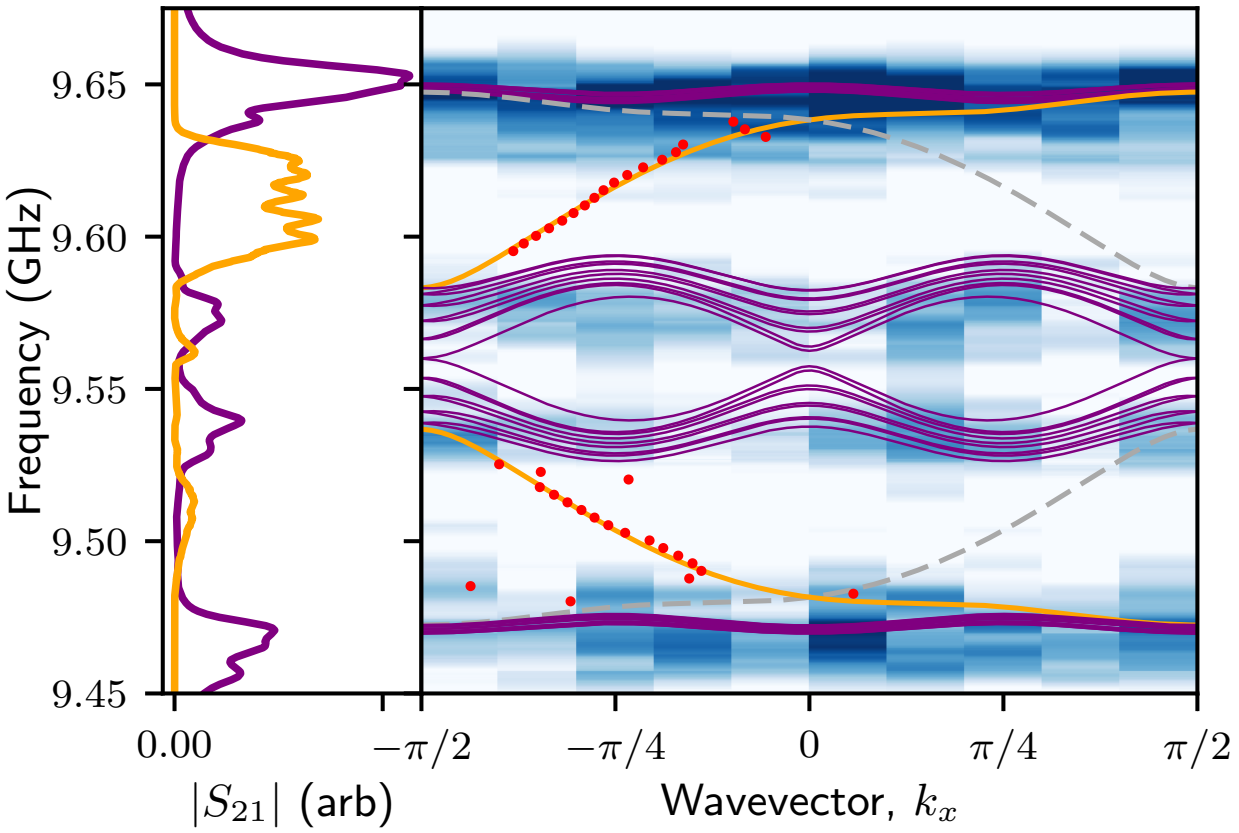

Figure 3.6: **a.** Measured transmission spectrum between two bulk (purple) and edge (orange) sites. The purple trace is the transmission between adjacent cavities in the bulk of the lattice ((5,6) and (6,6) defined from the upper-left lattice corner), while the orange trace is the transmission between cavities on the edge of the lattice (sites (1,1) and (1,11)). The differential response between upper and lower gaps arises from the distance difference for clockwise and anti-clockwise edge propagation between probe and measurement sites. **b.** Projected band structure of both the bulk (blue/white density plot) and edge (red points) of the system, compared with theory for a $\alpha = 1/4$ Hofstadter strip (purple/orange/gray-dashed). The bulk measurement results from a site-by-site measurement of the system response. The dispersion of the edge channel (explained in the SI) is extracted from the measured phase shift between cavities. Within the bulk bands, this phase is sensitive to disorder and overall geometry, resulting in a near-random signal. The bulk-bulk transmission exhibits four distinct bands which arise from the four-site magnetic unit cell. Gaps are apparent between the first and second bands as well as the third and fourth bands. The magnetic unit cell has two sites in each direction, compressing the Brillioun zone to $\left[-\frac{\pi}{2}, \frac{\pi}{2}\right]$. This picture comes from our paper [4].

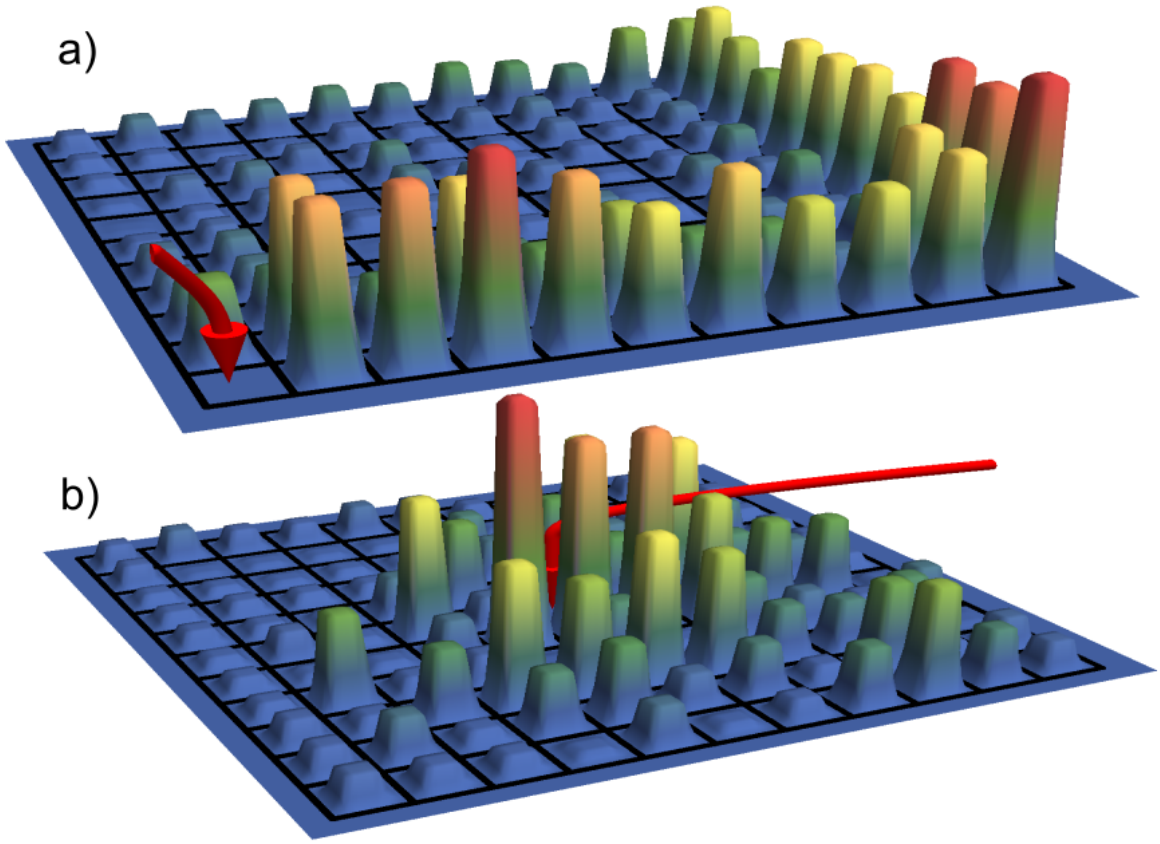

Figure 3.7: **a.** The response of the lattice when a bulk site (red arrow) is excited continuously at a frequency of 9.569 GHz within the upper band. The absence of bulk modes at the excitation frequency results in exponential localization of the response. **b.** The lattice's response to an edge-excitation (red arrow), at the a frequency of 9.622 GHz which is within the band gap. The presence of an edge channel at this frequency results in a de-localized chiral response along the system edge, decaying due to the finite resonator Q's. This picture comes from our paper [4].

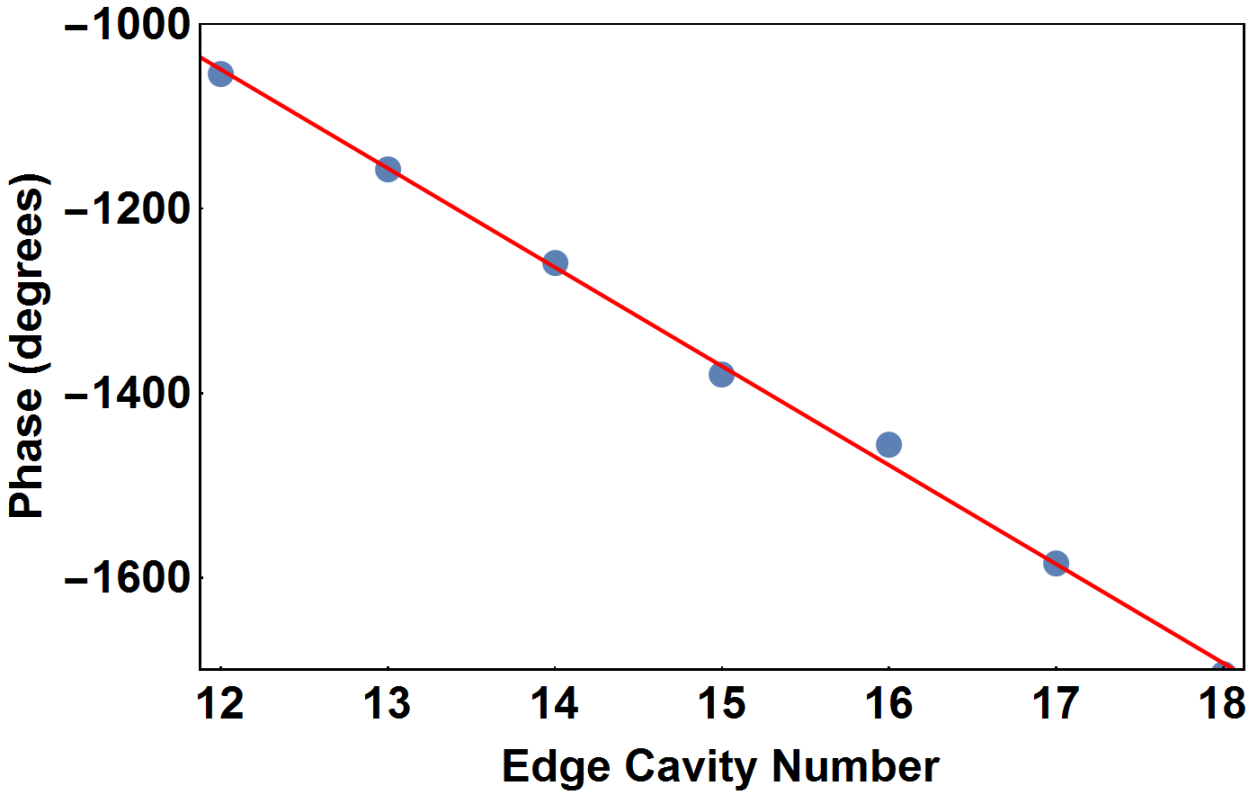

Figure 3.8: We measure the difference in phase between an excited edge cavity and other edge cavities as a function of distance. The edge cavity number starts at 12 and ends at 18 so that only one edge is fit to a line, do avoid additional dispersion introduced by the corner. We choose the side furthest from the the excited cavity to minimize the effects of direct coupling. For the frequency shown here ($\omega = 2\pi \times 9.61$ GHz) the lattice momentum is half the slope, or -54 deg per cavity. This picture comes from our paper [4].

theoretical prediction, showing good qualitative agreement.

3.6 Dispersion of the Edge Channel

The dispersion an edge channel can be measured directly from the evolution of the phase response along an edge of the lattice, when the system is excited on an edge within the bulk band-gap. In a square lattice, the dispersion is constant along a side but changes near the corners, so we examine the phase response on non-corner sites along a single side of the lattice (i.e. sites (11,2) to (11,10)). Plotting the phase shift as function of distance

between the excitation port and the measuring port yields a line with slope equal to the lattice momentum (see Figure 3.8 for a sample data set). In our measurements, we subtract the S12 direction from the S21 direction in order to eliminate the phase shifting from cable length and connectors. This subtraction means that the slope of the line is actually twice the lattice momentum. The S12 excitation moves around the lattice the opposite direction as the S21 excitation, so they travel a different distance. When S21 is subtracted from S12, this discrepancy manifests itself as a constant offset proportional to the perimeter of the lattice; the slope of the phase vs distance plot is unaffected. The phase shift per cavity can be a significant fraction of 2π, so phase unwrapping is necessary to recover the slope. Using this technique at a frequency within the bulk bands results in a near-random signal since this phase at that frequency is sensitive to disorder and overall geometry.

3.7 Dynamics of Microwave Chern Insulator

A major advantage of using microwave photons is that time-resolved transport measurements are possible. Instead of exciting the lattice with a constant signal from the network analyzer, we can also pulse a cavity on the edge and watch the pulse move in time with an oscilloscope. We mix a sinusoid of 9.6 GHz and a Gaussian with a width of 75 ns and excite the (1,1) cavity. Then we measure the response of each cavity as a function of time after the initial pulse. Figure 3.7c plots the response of the edge cavities as a function of time. The pulse travels in one direction with a well-defined constant slope. There are no backscattering modes due to the protection provided by the topology of the system. The pulse is visible for two cycles around the whole lattice. The group velocity is measured to be $0.32 \pm .04$ cavities/ns. This is consistent with the group velocity $\frac{\partial \omega}{\partial k}$ measured from the slope of the dispersion line at 9.6 GHz ($0.328 \pm .002$ cavities/ns). The pulse is short enough that there are some frequency components of the pulse that excite the bulk modes, and these can also be seen in the data. At the time where the pulse starts, a small excitation over all the

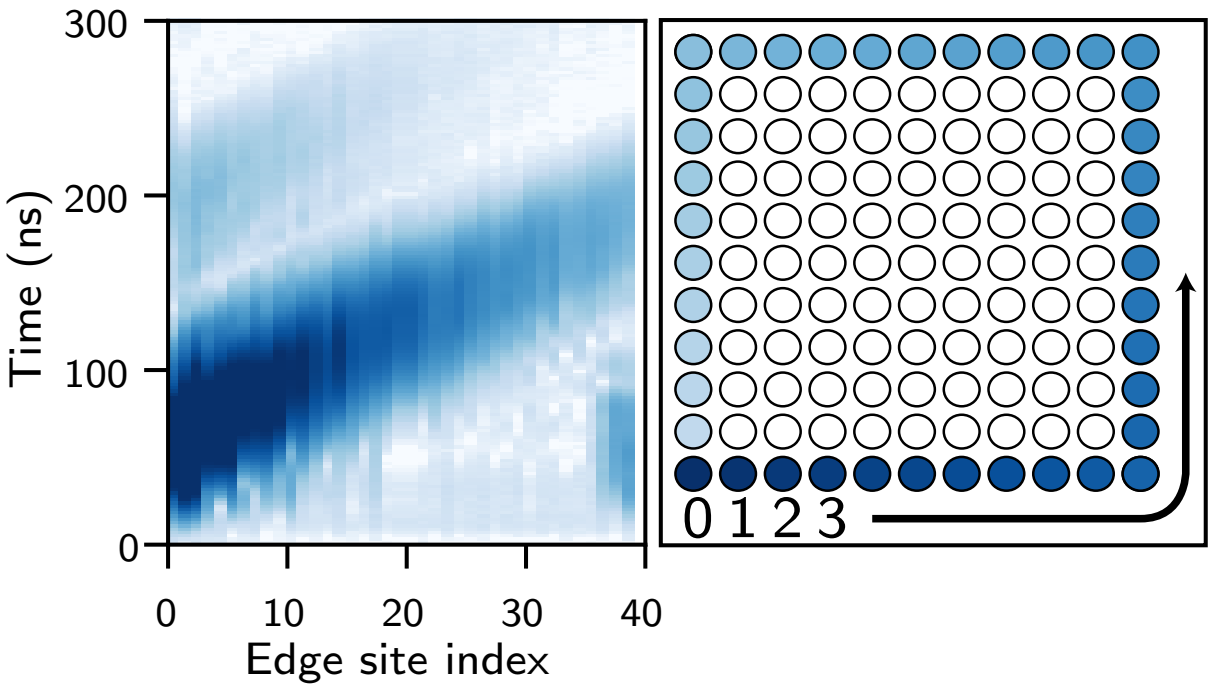

Figure 3.9: Spatio-temporal response of the edge cavities to a 50 ns pulse centered on 9.6 GHz. The x-axis is the indexed cavity number of each of the 40 edge sites, and the y-axis is time. The brightness reflects the intra-cavity intensity. The chirality of the edge channel is reflected in the unidirectional travel of the pulse. The weak stationary response results from a small Fourier-broadened excitation of bulk modes. This picture comes from our paper [4].

cavities does not move as a function of time. This is consistent with bulk modes. A video of pulse propagation can be found in the online supplementary materials. In this video, the measured response is renormalized at each time before plotting, so that even after decay the pulse can be seen clearly.

3.8 Photonic Tunnel Junction

Looking forward to exploration of strongly interacting topological phases [3], it will be essential to fabricate meta-material structures which operate as spatial interferometers [59, 60]. Such devices afford direct sensitivity to the charge and statistics of edge excitations through response of the interference fringe to magnetic flux and enclosed anyons, respectively.

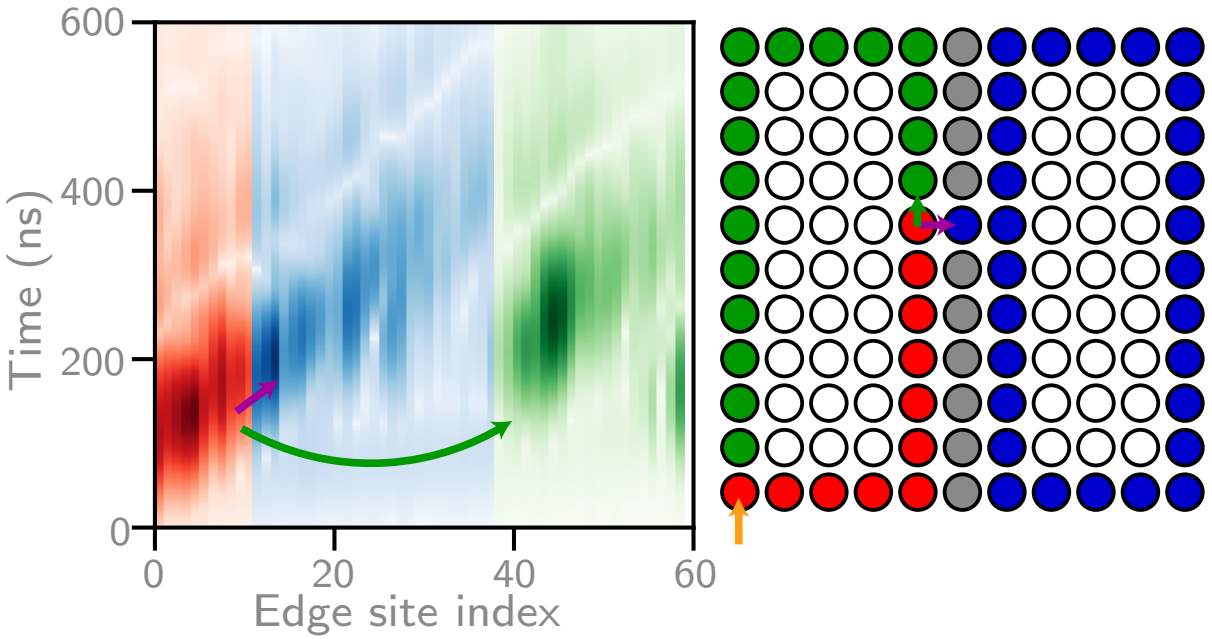

Figure 3.10: A wall is built into the lattice by detuning all but one cavities in the sixth row, separating the lattice into two 11x5 lattices connected by one cavity. This effectively makes a beam-splitter for running wave edge modes, as shown schematically at **right**. When the lattice is pulsed at 9.6 Ghz (in the top band gap), the response is shown in the figure on the left. The pulse splits when it reaches the gap in the wall (end of the red), transmitting most of the pulse to the green part of the lattice and some of the pulse into the blue, unexcited 11x5 sublattice. This picture comes from our paper [4].

As a first step towards this objective, we harness the extraordinary flexibility of our platform to realize a photonic tunnel junction, analogous to half of an solid-state edge-channel interferometer [20]. We realize the tunnel-junction by detuning a single column of lattice sites in our 11x11 sample, leaving only a single site in the center of column at its original frequency; this produces a "wall" between two sub-samples, with a narrow gap through which photons may tunnel.

Figure 3.10 shows this arrangement; a propagating edge excitation may either tunnel across the gap and stay in the original ring in which it was traveling, or continue along the edge into the neighboring ring, akin to a chiral-edge beam-splitter. Results are shown in Figure 3.10 for an excitation starting at cavity site (1,1)- it bears mentioning that while a fraction of the excitation remains in the original ring and a fraction hops to the other ring, none is

back-scattered, illustrating robustness of the edge channel to disorder. In the future, we plan to couple the central site to a transmon qubit. This would make that site nonlinear with photon number, so that when the site is excited, the cavity moves off resonance. This would effectively make the site a wall, and the rest of the pulse would stay in the left side of the lattice. However, the qubit could then emit into the right side, not only making a single photon source, but also trapping that single photon into a chiral edge mode.

3.9 Conclusion

We have demonstrated a complete toolbox for the development of low-loss topological microwave lattices, and harnessed this toolbox to realize a quarter flux Hofstadter model. The resulting synthetic material is be probed site-by-site, revealing an insulating bulk and topologically protected chiral edge channels. We showcase the flexibility of the approach by reconfiguring the lattice to act as a tunnel-junction, pointing the way to anyon interferometry once circuit quantum electrodynamics tools provide interactions between lattice photons.

Looking ahead, the next step is to marry these microwave resonator arrays with the tools of circuit quantum electrodynamics [42], thereby inducing on-site interactions. These interactions correspond to a Hubbard U in the Hofstadter-Hubbard model, immediately enabling studies of fractional quantum hall phases of interaction photons [3]. Because the demonstrated lattice is already low-loss at room-temperature ($\sim$ 3.5 MHz linewidth), the typical transmon qubit anharmonicity of 200 MHz [61] is sufficient to induce strong correlations between lattice photons. To prepare the photons in low entropy phases of the resulting models, it will be crucial to harness state-of-the art theoretical tools to populate these models near their many-body ground states. For small systems, this will rely upon spectroscopically resolved excitation of many-body states [23], while for larger systems engineered dissipation [62, 63, 13, 64] will allow for preparation of incompressible phases. In summary, the

platform opens many exciting prospects at the interface of topology, many-body physics, quantum-optics, and dissipation.

CHAPTER 4

ADAPTING THE CHERN INSULATOR FOR CRYOGENIC TEMPERATURES

4.1 Introduction

Designing a Chern insulator that works at cryogenic temperatures has a several benefits that can make the system an incredible tool for studying both quantum materials and chiral quantum optics. We use dilution refrigerators to cool samples to below 20 mK. The first benefit of cooling cavities to these temperatures is that we can make the lattice out of superconducting metal, so that the surface losses of the cavity are greatly reduced. Shown in Figure 4.1 is a picture of a niobium lattice. Since surface losses are the dominant loss source at room temperature, we can reach much higher quality factors for 3D cavities. Some of the best quality factors achieved in our lab for similar cavity geometries are as high as ~100 million. Higher quality factors mean that our particles will live longer, which is important since we want the interesting interactions, not particle loss, to dominate the physics simulated and observed. The frequency of particle loss needs to be much smaller than the other interaction frequencies in our system, such as tunneling, magnetic field strength, and inter-particle interactions. The other interesting benefit to cooling the Chern insulator to 20 mK is that we can then access quantum physics. First, we can couple Josephson junction transmon qubits (see chapter 5 for more details on qubits) to lattice sites. These qubits both have large single photon nonlinearity (~300 MHz) and couple strongly to 3D cavities. When a qubit couples to a lattice site it hybridizes and the lattice site inherits some of the nonlinearity. This nonlinearity then creates a blockade interaction, as a cavity shifts in frequency after absorbing a photon, so that another photon of the same frequency cannot excite the lattice site and thus is repelled. With this in mind the first step towards making our

photonic material quantum is to make the Chern insulator work at cryogenic temperatures. Achieving this requires sending magnetic fields through superconductors without destroying the quality factor of the cavities and designing a new way to tune the cavities.

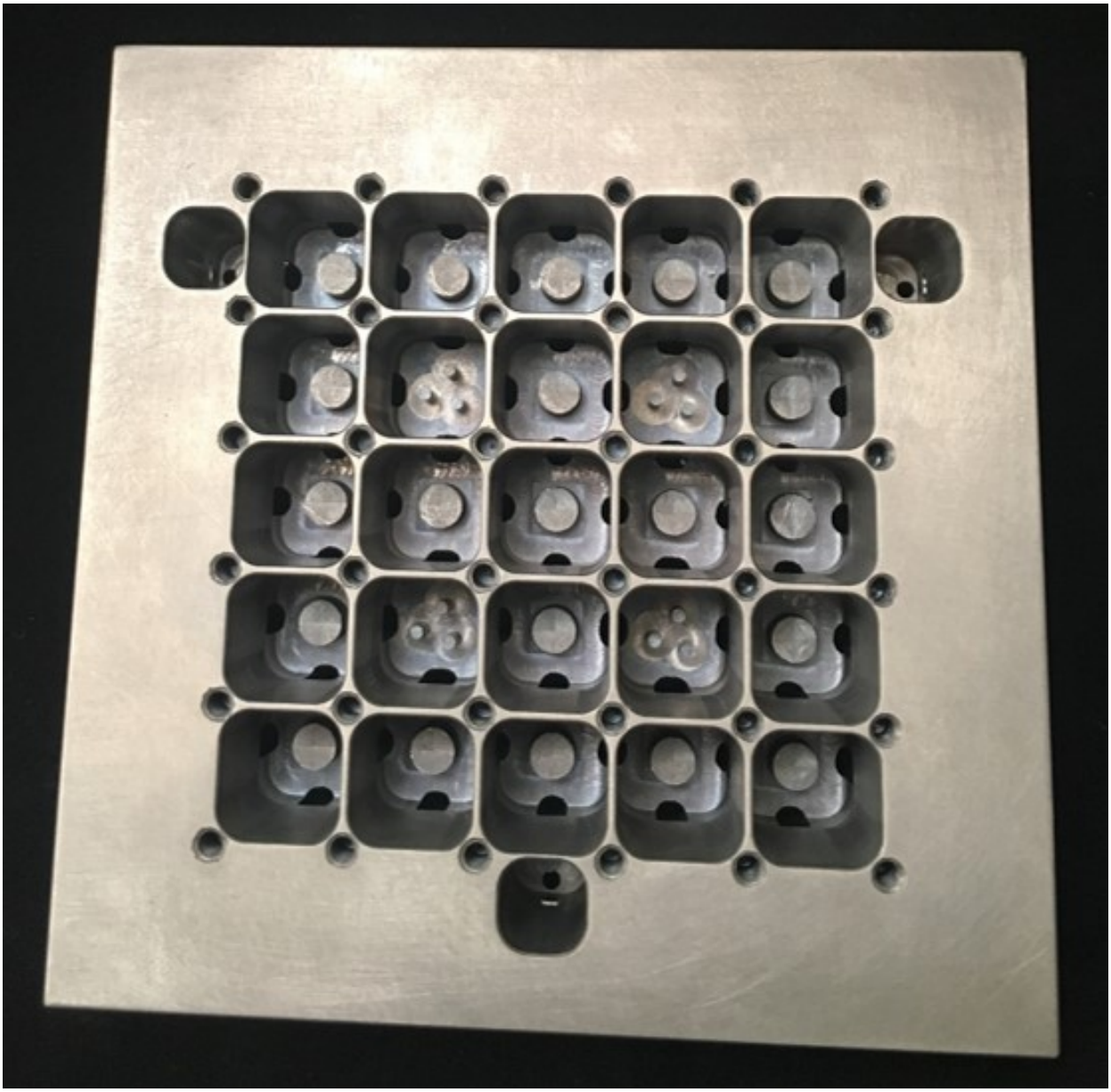

Figure 4.1: The 5x5 Chern insulator lattice made out of niobium so that it superconducts. On the edge of the lattice are three additional cavities. They are higher in frequency (10 GHz) and will be used later when we add qubits to the lattice.

4.2 Cryogenic Phase-Shifting Cavities

The first major challenge to making a Chern insulator out of superconducting cavities is to modify the design of the phase-shifting cavity so that it is superconducting and high quality factor, but also can couple strongly to a YIG sphere that is biased with a magnetic field. This is difficult for several reasons. First, magnetic fields either are repelled by superconductors or they pierce them and create normal regions that are lossy (see Figure 4.2). Second, the size of the magnetic field must be accurate to correctly bias the YIG sphere. Last, the YIG sphere must be mounted so that the frequency of the cavity is accurate and controllable, but the cavity quality factor is maintained (glues and pastes add large dielectric losses).

We first made three post cavities out of niobium and measured their quality factors as a function of temperature and magnetic field. We made single cavities that were small enough to fit in a Quantum Design PPMS fridge. This fridge can cool 1-inch-diameter samples (shown in Figure 4.2a) to 2 Kelvin in 3-4 hours,a capacity which is convenient when iterating quickly. Additionally, the PPMS is equipped with an electromagnet that can generate uniform magnetic fields up to 7 Tesla, which are much larger than the bias fields required on the YIG sphere (0.3 Tesla). In Figure 4.2b, I show the quality factor of a three-post cavity without a YIG sphere and no applied magnetic field as a function of temperature. The maximum quality factor of 1.5 million is reached at 2K, though at lower temperatures (20 mK) reached in the dilution fridge and surface etching of niobium we achieved cavity quality factors of 20 million.

If the field is instead applied after the cavity has transitioned to a superconducting state, then at field below the critical field (~1800 Gauss) the superconductor repels the field and no field reaches inside the cavity. At fields greater than the critical field, the superconductor breaks down and the cavity quality factor plummets. Even if the field is then turned off, the field stays trapped in the superconductor and the cavity retains it low quality factor.

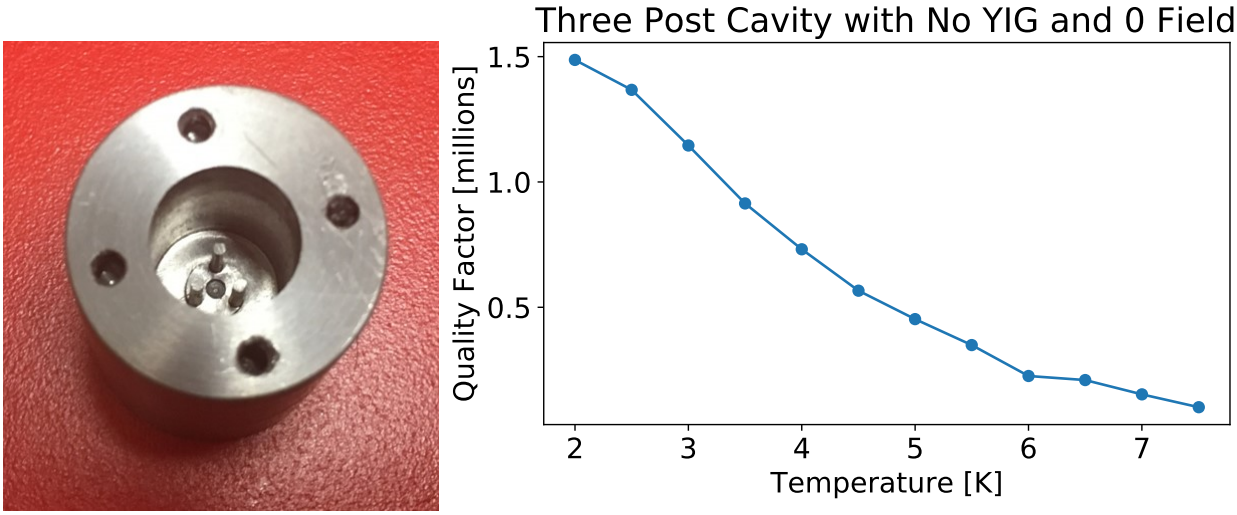

Figure 4.2: **Left.** Niobium 3 post cavity used to test how to achieve high quality factors with a YIG sphere in the cavity that is biased with a magnetic field. In the center of the 3 posts is a small indentation in which the YIG will rest. **Right.** Temperature dependence of the quality factor of the niobium cavity without and YIG sphere or field. This set the limit on the maximum quality factors we can obtain in these cavities to ~1 million (unless further surface treatment techniques are implemented).

This repulsion of magnetic fields makes developing a method of tuning the field on the YIG sphere particularly difficult.

Next, we look at the effect of a magnetic field on the three post cavity. In Figure 4.3 I show the quality factor of a cavity that is cooled in a magnetic field. For every data point the cavity is warmed above the superconducting transition point, the magnetic field is changed, and then the cavity is cooled in the magnetic field. The quality factor of the cavity quickly drops with increasing magnetic field. The field required on the YIG sphere is approximately 2500 Gauss: at those fields the quality factor of the cavity drops to below 20,000. Already we learn that simply applying a strong field to tune this YIG into resonance will not work for the cryogenic lattice. Next, we add a YIG sphere into the cavity and measure the effects on the quality factor without a magnetic field. Fig. 4.3 shows that the quality factor is somewhat worsened, but still greater than 300,000 when a YIG sphere is added to the cavity. This means the YIG sphere has some dielectric loss that will limit us from going to much higher quality factors. This is a different effect than the loss caused by coupling to the YIG mode

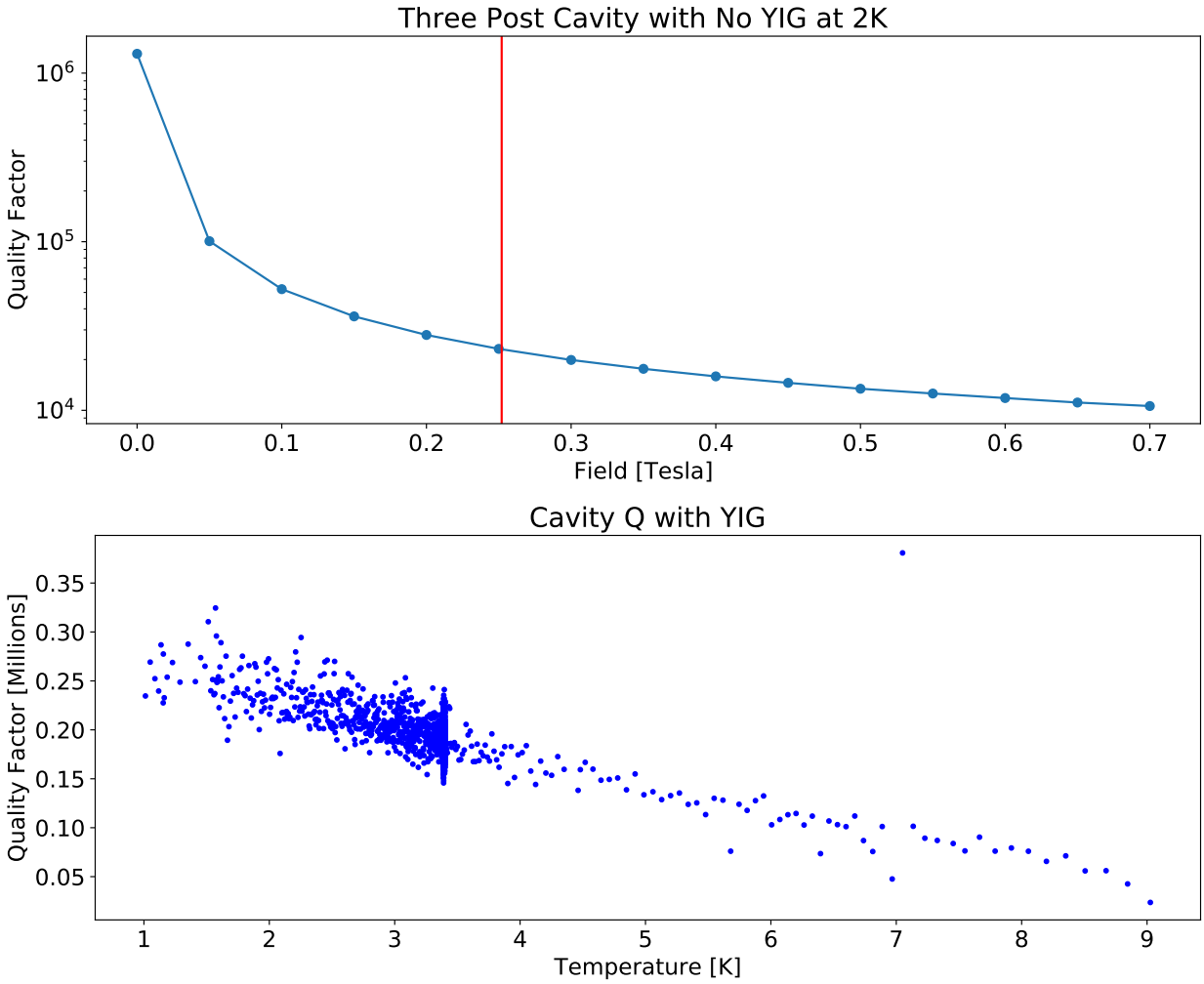

Figure 4.3: **Top.** Quality factor of a three post cavity as a function magnetic field. For every measurement, the cavity is warmed above the superconducting transition, then the cavity is cooled within the magnetic field and the quality factor is measured. The quality factor dies far below the field that tunes the YIG to the cavity resonance. **Bottom.** Quality factor of the 3 post cavity with a YIG sphere as a function of temperature. The YIG sphere lowers the quality factor of the cavity but the quality factors still reach ~300 K.

which will be examined later in this section. These results mean that if we can solve the problem on how to route enough field to the YIG sphere without trapping too much magnetic field in the niobium, then we can possibly achieve quality factors of around 300,000, which is ~100 times better than achievable at room temperature and corresponds to lifetimes around 200μs.

Before solving this problem, we wanted to make sure that the YIG cavities' phase-shifting properties still behave similarly at cryogenic temperatures. In Figure 4.4, we plot the frequency and phase of the modes in a YIG cavity as a function of magnetic field by measuring transmission through the YIG cavity that are $\frac{\pi}{4}$ radians apart from each other. As seen in the room temperature phase-shifting cavities, we break the degeneracy between the chiral modes. The quality factor of these modes is only 20,000, a factor of 5 times larger than the quality factor at room temperature. However, the phase shift in the cavity with even minimal (1000 Gauss) applied field is still equal to the angle between the transmission ports, which means the cavities can work at cryogenic temperatures.

While many ideas to increase the YIG cavity quality factor were tested, we settled on using small permanent magnets that were placed as close to the YIG sphere as possible without being in the cavity. Fig. 4.5 shows a schematic of the setup. This minimizes the magnetic field in the superconductor and localizes most of the field within the YIG sphere. However, using small permanent magnets ($\frac{1}{16}$ inch diameter and length) to get to 3000 Gauss at the center of the YIG is not possible. We found that if we maximized the YIG-to-cavity coupling, then even if the magnetic field was not strong enough to tune the YIG mode into resonance with the degenerate chiral cavity modes, the splitting between the two chiral modes would be large enough that we could maintain site-to-site couplings much larger than our disorder. At cryogenic temperatures we estimated our disorder to be ~1 MHz (more details on this in section 4.3), so we set a minimum on the site-to-site coupling to 15 MHz. This means that the chiral modes must be split by around 200 MHz to keep the frequency shifts from

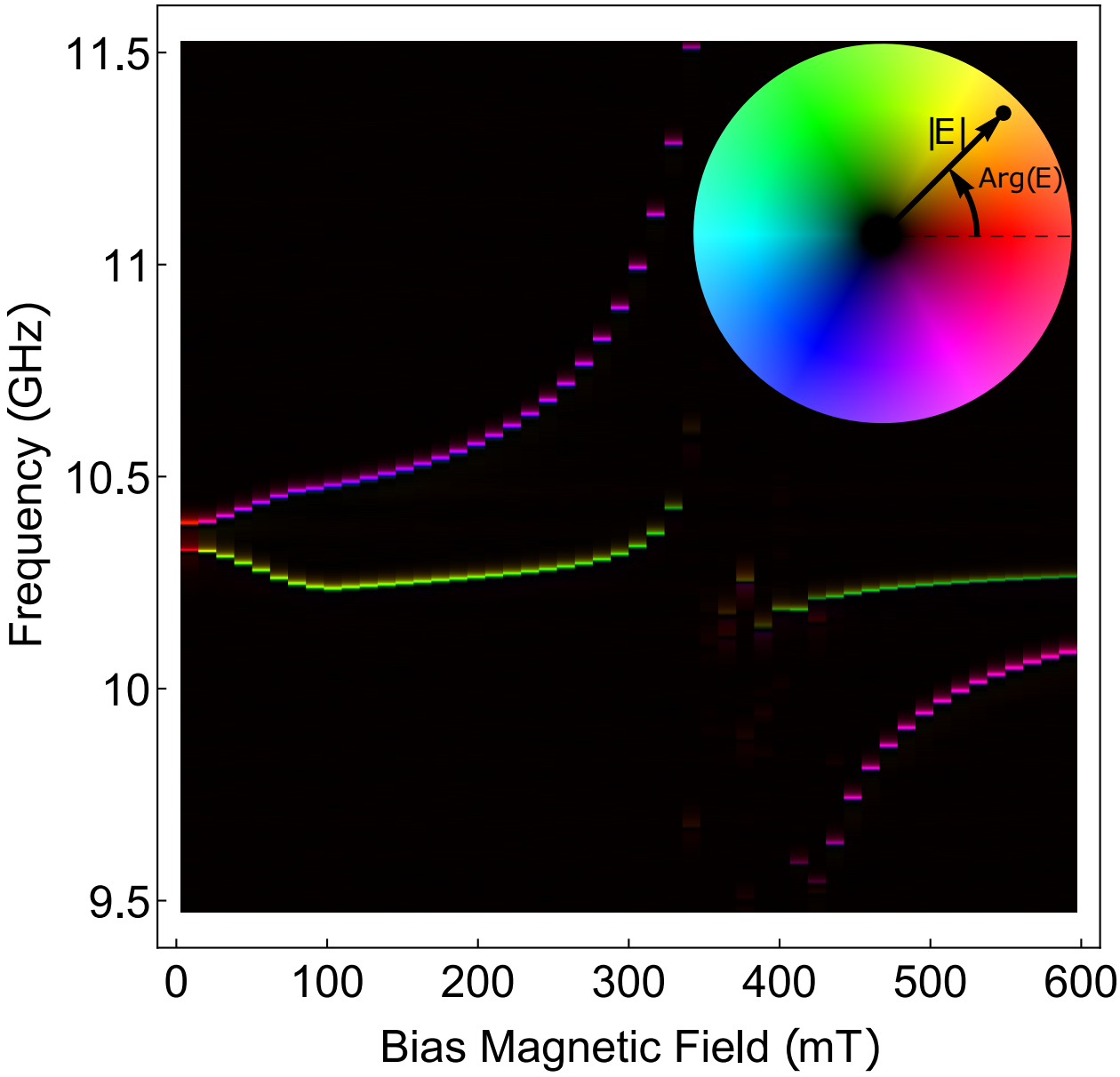

Figure 4.4: Magnitude and Phase of transmission through a superconducting YIG cavity as a function of magnetic field between two antenna with $\frac{\pi}{4}$ radians between the referenced from the center of the cavity. At zero field, the two mode are near degenate and are red, which indicates that there is zero phase shift in transmission. As the field is increased, the modes split in frequency and change color to purple and green. This illuminates the time-reversal symmetry breaking between the two modes. The difference in phases arises from the chiralty of the two modes, since one mode will take the "shorter" route between the antenna, while the other takes the "longer" route. The phase has an additional factor of two since we are subtracting the transmission of S12 from S21 to eliminate cable noise.

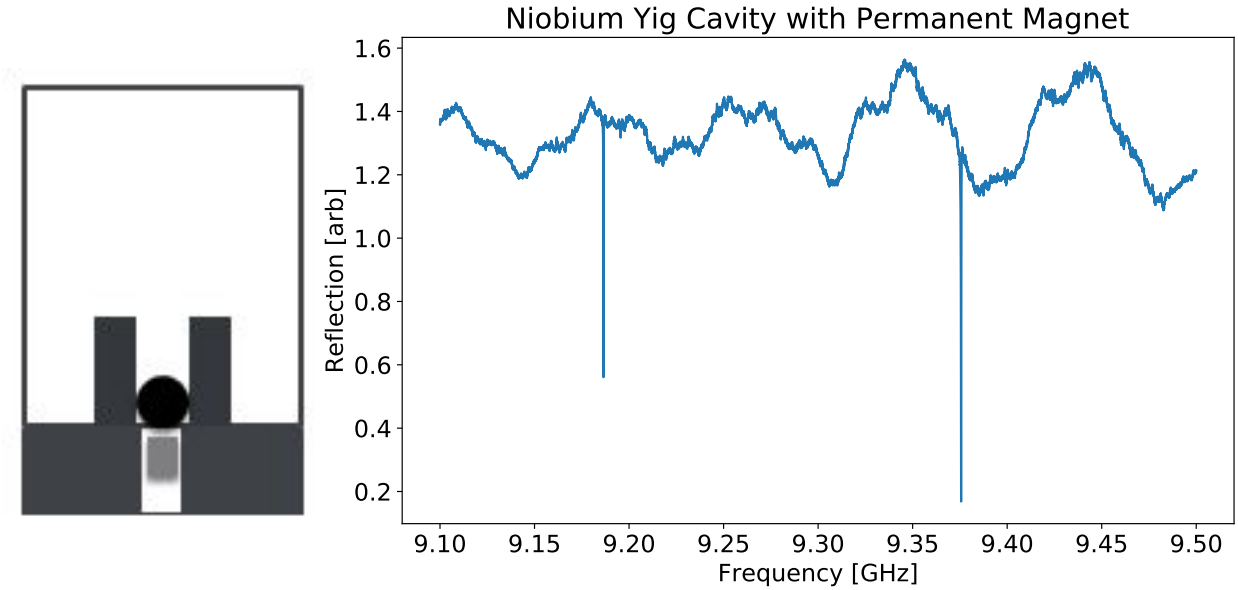

Figure 4.5: **Left.** Schematic of how we applied magnetic field to the YIG without destroying the cavity quality factor. A $\frac{1}{16}$ inch diameter hole is drilled into the niobium on the opposite side of the cavity so that the hole almost breaks into the cavity. .020 inches of material is left behind, and a neodymium magnet is put into the hole. This biases the YIG sphere, but applies less magnetic field into the critical areas in the cavity (the tops of the posts). **Right.** The YIG is biased but it is not on resonance, so the only two modes seen are the dark mode (lower frequency dip) and the bright mode (higher frequency dip). The coupling between the YIG sphere and the cavity is large enough so that the modes are split by 180 MHz. Since less field is applied the quality factor of the cavity still reaches ~200000. The shape of background of the measurement is due to impedance mismatches between wires and connectors in the measurement apparatus, specifically because these impedance mismatches change as a function of temperature so they cannot be calibrated out.

off-resonantly coupling to the out-of-band chiral modes below 1 Mhz. Figure 4.5 shows both a schematic picture for the magnetic configuration and the transmission through the biased cavity while at 2K. Even though the splitting has been halved to 200 MHz, the quality factor of the modes now reaches 200,000, a value 100 times better than room temperature lattices.

4.3 Tuning Cavities at 20 mK

After designing a chiral YIG cavity that works in a dilution refrigerator, we developed a technique to tune the cavities to the same frequency. This is difficult for two main reasons. First, the cavities shrink as they cool, which changes the cavities' frequencies differently from cavity to cavity. Second, actively tuning the cavity is challenging while it is in the dilution refrigerator since the lattice is physically inaccessible to tune. Furthermore, even if the sites were tunable, measuring individual bare site properties to know which site to tune is difficult when all of the sites are coupled.

We first tested using screws similar to how we used them in the room temperature Chern insulator. However, we had difficulty stabilizing the screws so that the cavities consistently cooled down to the same frequency and quality factor. With superconducting screws made out of aluminum, we noticed that the contact between the screws and cavities changed between cooldowns, which would change the cavities' frequency and quality factor. Instead, we tried using dielectric screws. These performed somewhat better but still were susceptible to inconsistency over time and cooldowns. We decided that instead of using screws to tune lattice sites, we would semi-permanently tune sites by sanding down the post of each cavity until the cavity was at the right frequency. Although a more tedious method at first, this resulted in cavities maintaining precise frequencies over periods of time longer than we were measuring them (months). If a cavity was sanded down too much, small amounts of indium (a soft superconductor) can be pressed on top of the post. This allows for gradual tuning of

the cavity to both higher and lower frequencies. The same techniques can be used to tune the YIG cavity as well, though care must be taken to both not break the smaller post and balance the tuning of each post in the cavity. In an extreme situation where one post is tuned much more than another post the degeneracy of the modes will be broken in a non-chiral basis, which would make the cavity not phase shift like it is required to in order to generate the magnetic field.

Once we had a way to tune the cavities consistently, we then solved the issue of the cavity frequencies changing as the lattice cooled. Since metal contracts as it cools, the frequencies of the cavities are higher at cryogenic temperatures than at room temperature. Also, the cavities shift frequencies differently depending on what type of cavity (YIG or fundamental) and where it is in the lattice (corner, edge or in the bulk). However, we found that from cooldown to cooldown the shift stayed the same, so we measured the shift of each type of cavity and then compensated for the shift differential at room temperature. This made it so that the lattice sites actually tune into degeneracy as the lattice cools.

4.4 Measuring the Chern Insulator

Once the lattice is tuned, we then have to measure it. This is also more difficult in a dilution refrigerator since both radio frequency lines and switches are more costly in space, money, and time. To make this easier, we made a 5x5 lattice so that there are as few sites as possible while maintaining a definite bulk and edge. In order to measure the lattice, we again put antennas on every site. Each antenna is undercoupled, with a coupling Q (see section 2.5.1 on coupling Q's) of approximately 10^6 to a single uncoupled site, while the internal Q's are $\sim 2 * 10^5$. Upon coupling the cavities, the coupling Q varies greatly between modes since they have different spatial profiles, but they are always more than the original coupling Q since the maximum coupling to the antenna happens when the mode is fully located on the site with

the antenna. These antennas are then wired to switches that are also cooled to cryogenic temperatures. The switches that worked at these temperatures were Radiall 10 way switches, part number R573412045. We used two 10-way switches so that we could measure most of the 25 sites of the lattice. For a picture of the setup, see Figure 4.6. These switches were then routed through a directional coupler so that we could perform both reflection measurements and transmission measurements on the lattice, although transmission could only be done between sites connected to different switches. Out of the five last sites not connected to the switches, four of them were the YIG cavities. We wired input lines to these cavities. For the last fundamental site not connected through the switches, we used a circulator and our last output line so that we could also do reflection measurements on this site. This site was a corner site and the site we later used to pulse the edge modes of the Chern insulator. Having one site not on the switches allows us to measure transport from that site to all the other sites instead of just to half of them.

We then followed a procedure similar to that used in measuring the room temperature lattice. We measured transmission through the lattice and reflection on the lattice using all of the possible ports. In Figure 4.7 we show results measuring reflection on the center site $(3, 3)$ of the lattice and compare them to a reflection on the edge site $(5, 1)$. Since the number of sites decreased and the quality factor of the modes increased compared to the room temperature lattice, the individual modes of the lattice are now resolvable spectroscopically. According to calculation of the band structure there are three edge modes in each gap between the bulk bands (shown in Figure 4.7). In the data we see the four bulk bands at 8.985 GHz, 9.02 GHz, 9.051 GHz, and 9.083 GHz. The peak in the center of both spectra at 9.037 GHz is from the 5 degenerate modes near the Dirac cone formed from the two middle bulk bands touching at certain momenta. This mode being at the center of the spectrum is consistent with simulations and is the frequency to which we tuned the lattice. The modes in between the larger bulk bands are delocalized since their momenta are fixed. In between the two lower frequency bulk bands are three edge modes at 8.996, 9.004, and 9.010 GHz. In between the

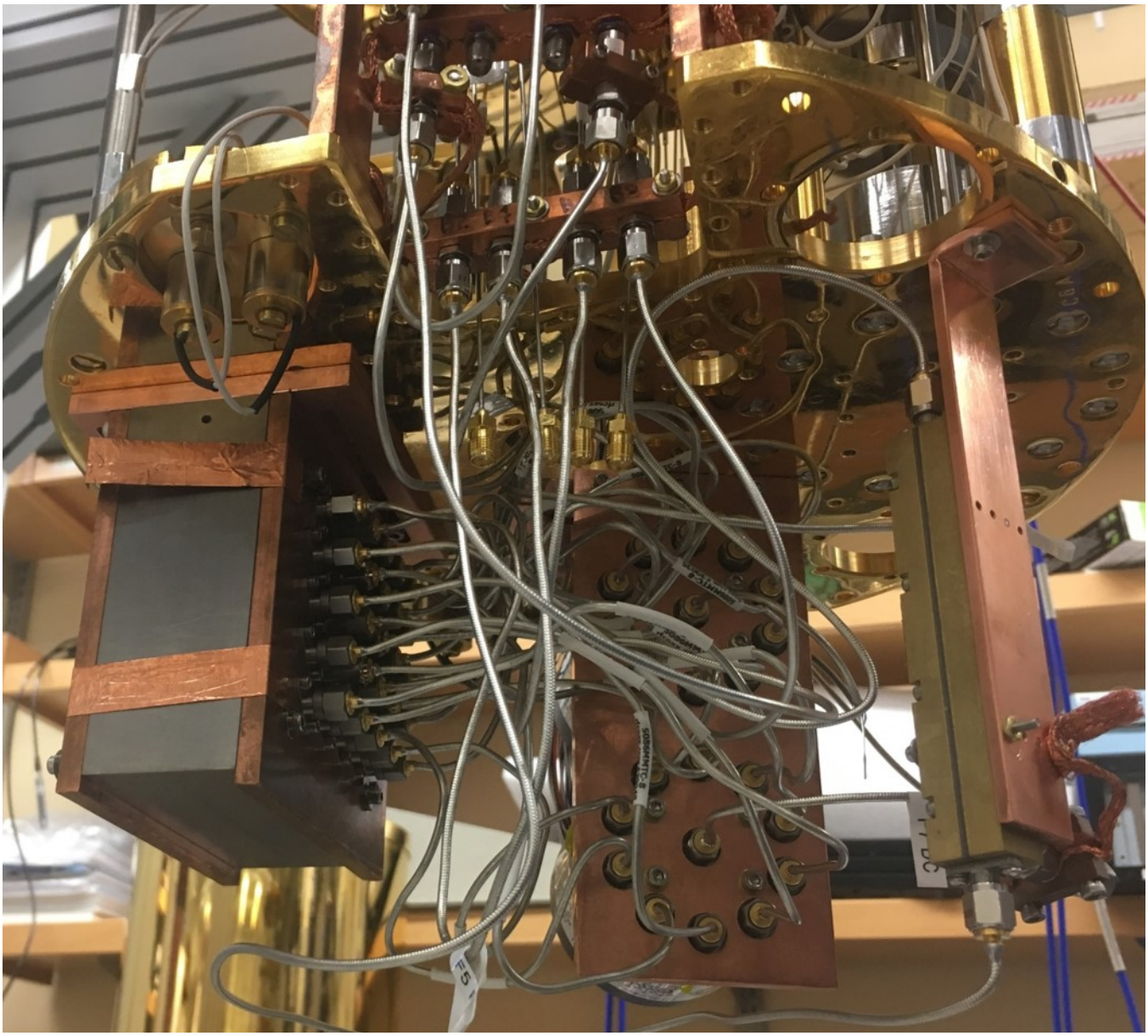

Figure 4.6: Physical setup of the tuned cryogenic lattice. On the left is the lattice with coaxial wires attached to SMA antennas mounted on top of every lattice site. The coax cables are routed through the ten way switches in the middle of the picture to minimize the number of through lines needed (lines running all the way through the fridge). On the right is the directional coupler that allows us to perform reflection measurements from a single SMA antenna.

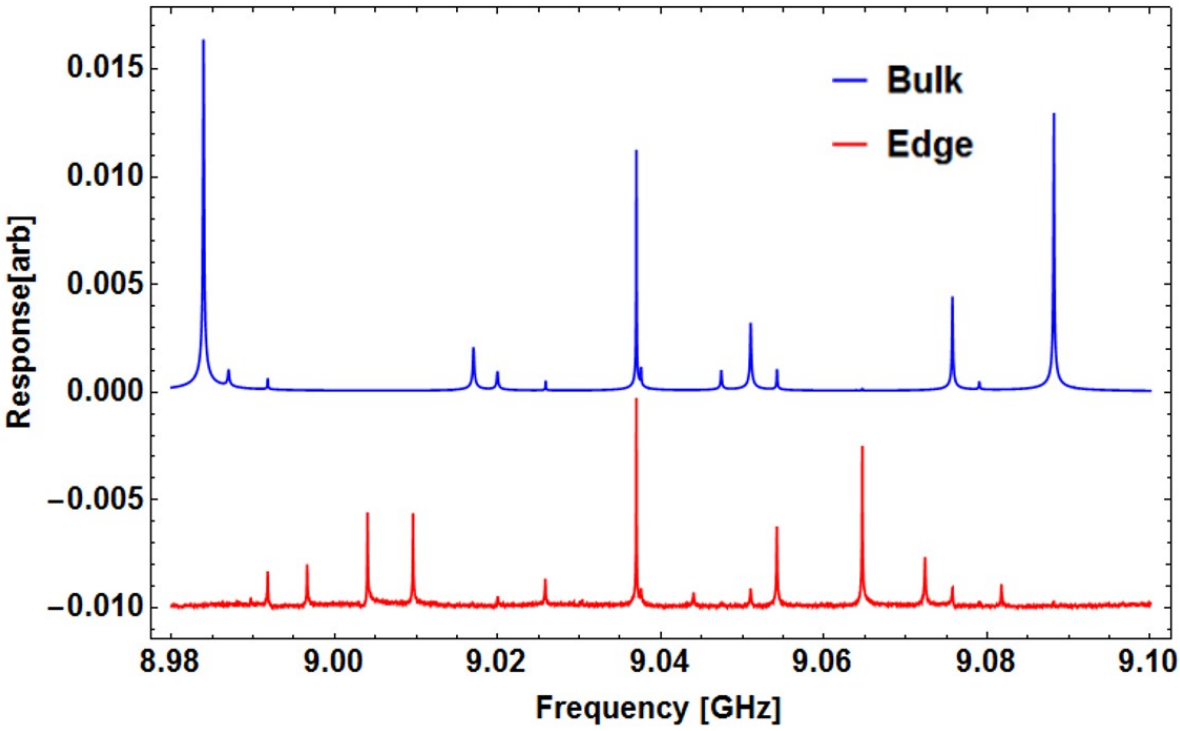

Figure 4.7: Reflection measurements on the lattice in different locations. The blue is a reflection on the middle site (3,3). The four bulk bands and the modes near the Dirac mode can be seen, with large gaps in mode between the first and second modes and the third and fourth mode, as predicted from band structure calculations (see Figure 3.3). The red plot is a reflection measurement on the edge site (5,1). The modes represented most strongly are in the gaps of the bulk reflection and the ones near the Dirac cone. The modes are the chiral, protected edge modes.

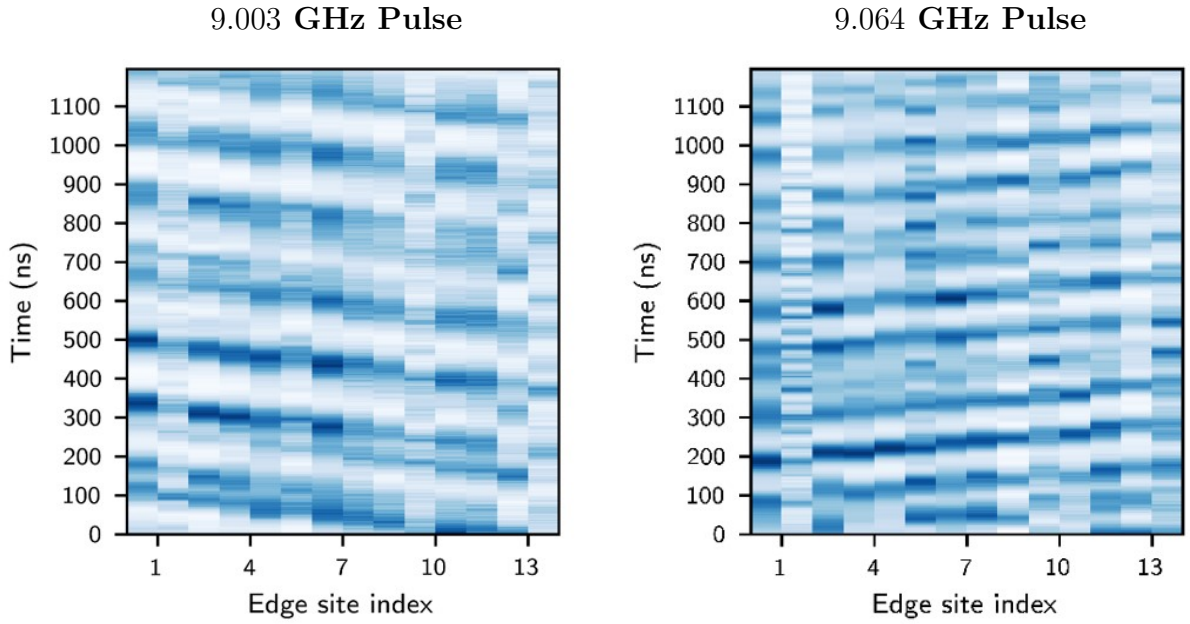

Figure 4.8: **Left.** We pulse edge site (1,1) of the lattice in the lower band gap at an edge mode frequency of 9.003 GHz (see Figure 4.7) with a Gaussian pulse of width 80 ns. The blue is the response as a function of time and which edge site. The edge site index is unwrapped around the lattice just like in the similar result at room temperature in chapter 3. The pulse moves around the edge in only one direction, demonstrating the chirality and time-reversal symmetry breaking of the edge channel. For this frequency, the pulse takes ~160 ns. **Right.** We then pulse the same lattice site at 9.064 GHz, exciting the edge modes in the upper band gap. These modes have opposite chirality, as can be seen by the different slopes of the pulse in the two plots. The pulse at this frequency also travels with a greater velocity, completing a round trip in ~100 ns, though there is some interference, possibly caused by the short pulse exciting other modes in the lattice and due to the length of the pulse being comparable to the time it takes for the pulse to travel around the lattice.

two higher bulk bands are two peaks at 9.065 and 9.072 GHz. The taller peak at 9.065 GHz is likely two degenerate edge modes, as predicted by simulation.

To further test that these are chiral edge channels, we again take advantage of the ability to pulse the lattice at the frequency of the edge channels (see Figure 4.8). Pulsing the lattice allows us to observe transport as a function of time, verifying that these modes can transport photons chirally, which is a signature feature of a Chern insulator. To generate the pulse we mix a sinusoid at the lattice frequency we are exciting and a Gaussian pulse with a width of 80 ns. This pulse time is long enough that it excites only the modes in the lower band

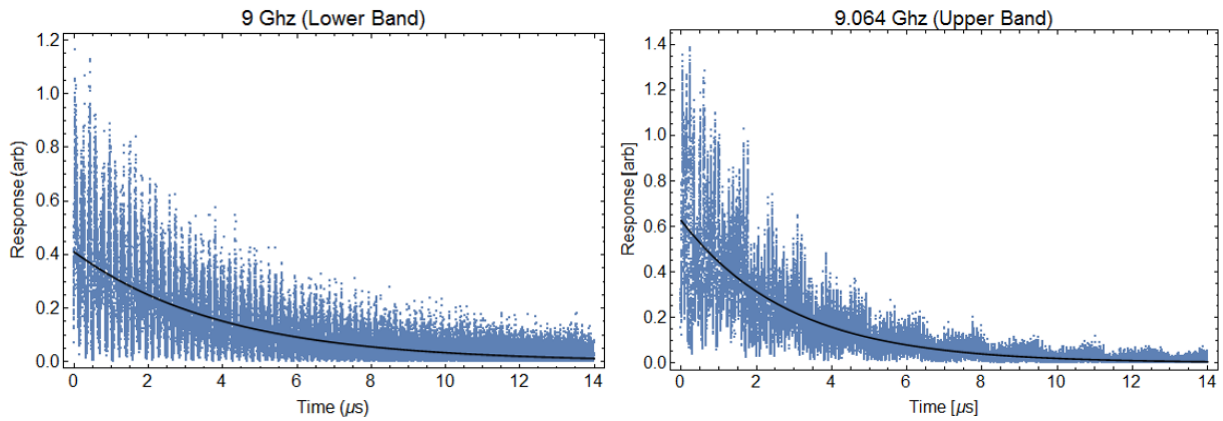

Figure 4.9: **Left.** The response on a single site as a function of time after a pulse is input into the edge mode at 9 GHz. Instead of fitting the function exactly, we bin the data and fit it with an exponential to get an estimate of the decay time of the edge channel. For these modes, the decay time is 4.0μs **Right.** Similar measurement but for the upper edge band at 9.064 GHz. The lifetime of this mode is 2.9μs

gap, but is short enough that it concludes before the pulse travels around the lattice. We excite the $(1, 1)$ cavity and measure the response of each cavity as a function of time after the initial pulse. Figure 4.8 plots the response of the edge cavities as function of time when we excite the $(1, 1)$ cavity at both 9.004 GHz and 9.064 GHz. Both excitations are chiral, but they have the opposite chirality. This can be seen from the opposite slopes of the pulse for each of the edge modes. The slopes of the lines represent the velocity of the pulse. For the 9.004 GHz pulse, the velocity is 0.09 sites/ns, while for the 9.064 GHz pulse, the velocity is 0.16 sites/ns. The amplitude can be binned and then fit to an exponential decay function to calculate the lifetime of the mode, as shown in Figure 4.9. The lifetime of the 9.064 Ghz edge mode is 2.9μs while the lifetime of the 9.004 Ghz edge mode is 4.0μs. The difference in the edge modes' velocity is still not understood. Since there are only three edge modes, the slope the dispersion is not as well defined, but the total gap size of the modes are similar, so the slope should not vary much. A video of the pulse propagating through the lattice can be found online at https://www.youtube.com/watch?time_continue=13&v=-mpLZylrfEQ or on the Simon lab website.

4.5 Conclusions

The technical innovations discussed in this section were major steps in the work towards making quantum topological materials out of photons. We designed and created a Chern insulator that not only works at cryogenic temperatures, but also has cleaner dynamics and better parameters than any other system. The particles have lifetimes of microseconds while all the other important timescales (tunneling, nonlinearity of the qubits, and interaction energy) in the system are tens of nanoseconds or less. Furthermore, this system is completely modular, allowing for different sized lattice or the addition of other features as needed.

There is a lot of room to improve the cavity lifetime, the time-reversal symmetry breaking, and the tuning. Both of the first issues are limited by the way we apply magnetic field to the YIG sphere. By coming up with a better way to funnel magnetic field to the YIG, we could both increase the field on the YIG and decrease the field causing normal regions in the superconductor. There are implementations of a superconducting magnetic "hose" [65] that would be compatible with the YIG cavities, if a hole was drilled all the way through the niobium to the YIG. This cannot be done with just a magnet since a magnet being anywhere near the cavity mode destroys the cavity quality factor. The methodology for tuning the lattice can be upgraded as well, though this requires adding magnetic coils to either replace or enhance the permanent magnet in each YIG cavity. Tuning the fundamental cavities is quite easy since they all shift in frequency in a consistent way (after taking into account the location in the lattice), but tuning the YIG cavities is more difficult since the YIG is only held in place by the magnet itself. Adding a coil would allow the frequency of the YIG site to be tuned, though this preferably would be done while the whole lattice is tuned so that the lattice would not have to be warmed up again. This means that either the lattice would need some way to block or detune the YIG cavities' neighbors, or the Hamiltonian tomography needs to be upgraded to apply to the YIG cavity [56].

CHAPTER 5

COUPLING QUBITS TO THE CHERN INSULATOR TO ENGINEER PARTICLE INTERACTIONS

The final piece of the material simulation toolbox we developed was nonlinear lattice sites that can be used to induce effective particle-particle interactions. This last component is necessary to access quantum phenomena in materials, since nonlinear lattice sites allow you to control the number of photons in each mode, and create interactions that entangle particles. The nonlinearity is achieved by coupling a transmon qubit to the lattice sites. Transmons are essentially LC resonators with nonlinear inductors (see section 5.1 for details on how the qubit was designed). The nonlinearity in the inductor causes the LC resonator to have large anharmonicities (~300 MHz in our qubits). These anharmonicites are significantly larger than the tunnel coupling between lattice sites, which means that only one particle can be in a particular mode because the 2 photon state of any mode will be outside the band structure of the lattice. To achieve these large anharmonicities the transmon has to replace the linear lattice site resonator; otherwise the anharmonicity of the lattice site will be reduced because the hybridization with the linear resonator essentially divides the anharmonicities between the two modes. While this is possible (see Chapter 6), the work discussed in this section will instead focus on dispersively coupled transmons. In this setup, the transmon is detuned from the lattice site by ~1 GHz, so the lattice site mode is weakly hybridized with the anharmonic transmon mode. This configuration is a good intermediate step with which to work since the lattice can be largely unmodified while the interplay between nonlinearity and chiral modes can still be explored.

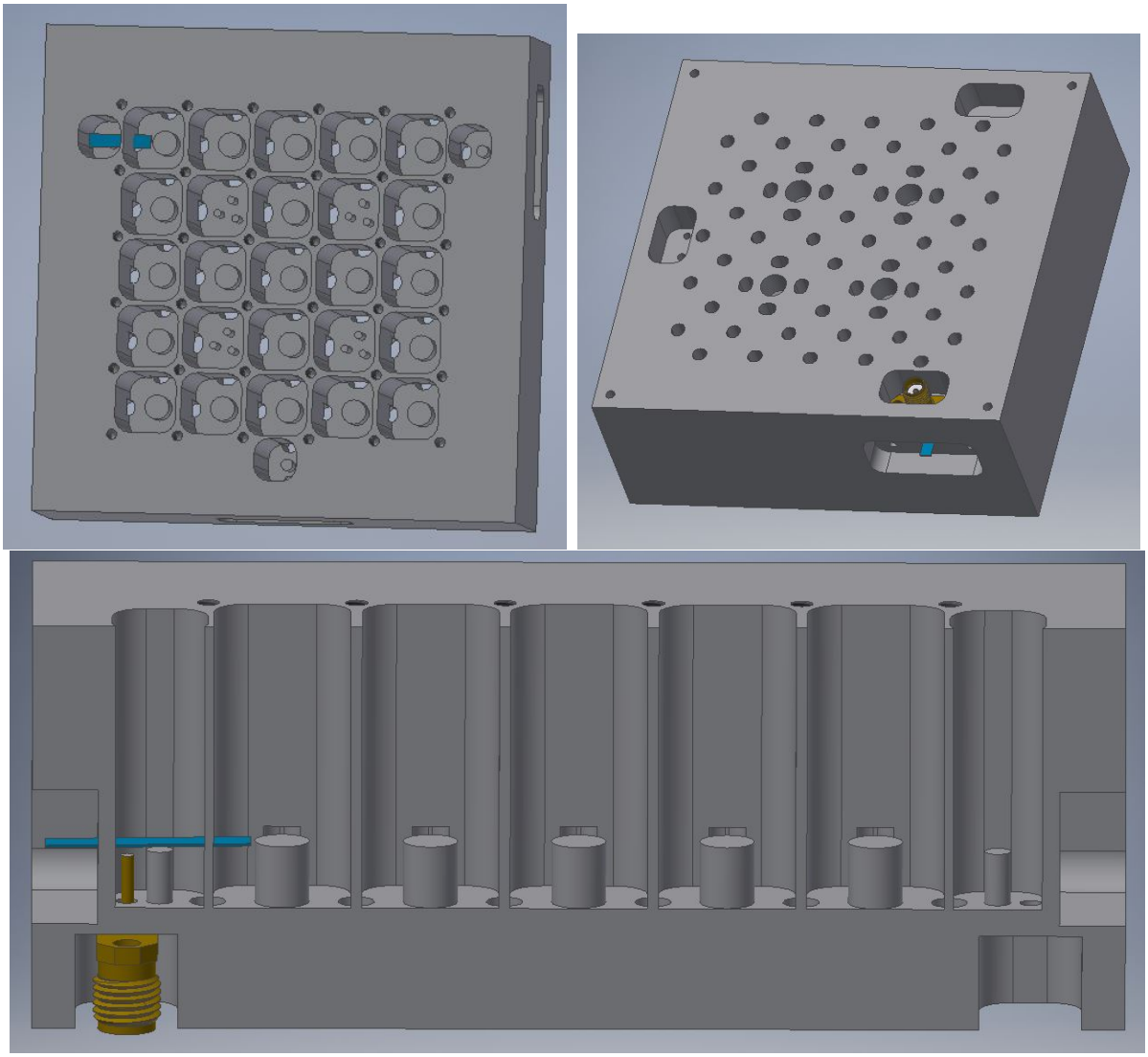

Figure 5.1: **Top Left.** Top down view of a 5x5 lattice with a single qubit coupled to an edge site resonator. The top left cavity has a sapphire chip (blue) inserted such that some of the qubit is in the latttice site cavity and some is in the the smaller readout resonator cavity on the edge. Also in this particular lattice design are three other readout cavities in case we wanted to couple more qubits to the edge sites. **Top Right.** Bottom view of the lattice. The SMA antenna that couples to the readout cavity is mounted in an inset so that the dipole antenna is short enough so that it has no modes near the cavity frequencies. The qubit is clamped in place via a copper part that screws into the inset with the sapphire chip coming out of it. This allows us to put a separate copper piece over this inset to further make the cavity light-tight. All of the holes in the cavity are then covered with thermalized copper lids that are sealed tight around the cavity with indium. **Bottom.** Cross sectional cut through the lattice so that the inside of the lattice can be seen. The qubit protrudes into the cavity so that the junction sits in the coupler between the readout resonator and the lattice cavity. Pads of the qubit extend into each cavity to couple to the cavities.

5.1 Designing the Qubit

The qubit systems we use are often called 3D qubits since they consist of 1 or more 3D microwave cavities coupled to a transmon qubit. Figure 5.1 is a diagram of the setup and Figure 5.2 shows a model of this setup in the software (ANSYS HFSS) that is used to solve for the qubit and cavity parameters. The transmon is suspended between two different cavities. The cavity on the right represents the lattice site to which the qubit is coupled and the cavity on the left is the readout cavity of the qubit. The readout cavity is tuned to higher frequency than both the qubit and lattice, but the coupling Q of the readout cavity is much lower so that photons can be taken more efficiently out of this cavity. The frequency of this cavity changes depending on the qubit state. This allows us to measure the state of the qubit nondestructively by measuring reflection or transmission through the readout cavity. This is discussed in more detail in section 2.5.1. We suspend the transmon in the lattice so that one pad of the qubit reaches into the readout cavity while the other reaches into the lattice cavity. This allows the qubit to couple to both resonators. The amount of the coupling to each resonator can be controlled by changing either pad. Using HFSS to calculate the admittance of the cavity near the junction position allows us to solve for the parameters of the qubit using the black box code [5].

Designing a 3D qubit is challenging because many important parameters need to simultaneously be controlled. Fortunately, there are quite a few ways to control these parameters, though often changing one design feature affects several of the qubit parameters. The following list is a comprehensive description of these parameters that also will serve as a definition of terms for the rest of this section. A table explaining the important terms follows:

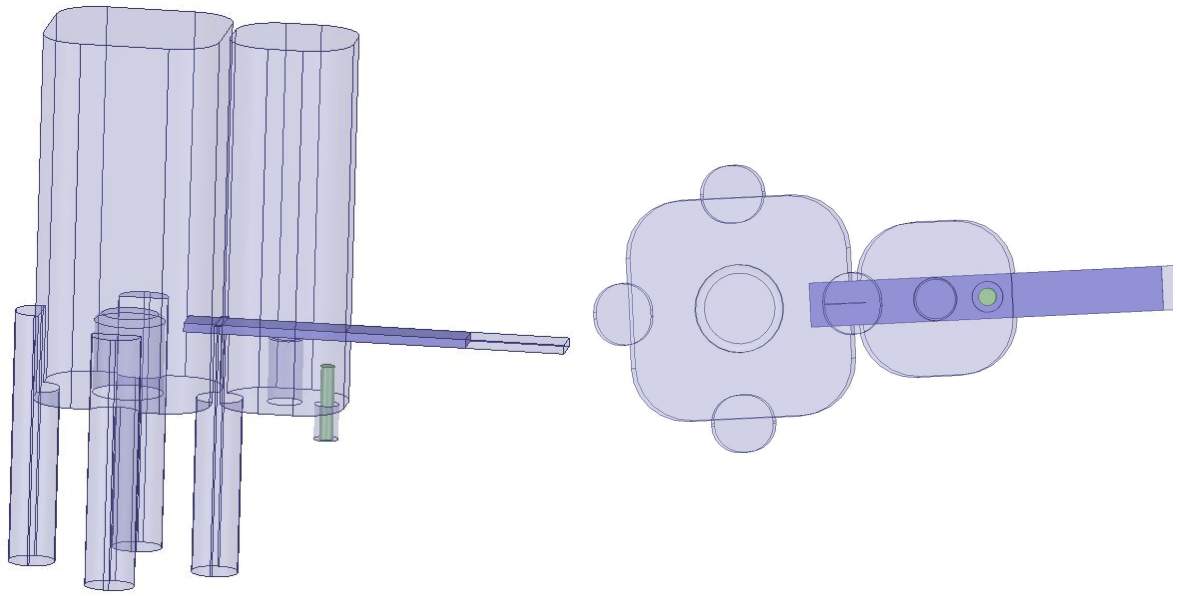

Figure 5.2: HFSS schematics of the qubit-cavity system with only one lattice site. These simulations are used to calculated the admittance at the location of the qubit. The admittance is used in conjunction with the black box code [5] to calculate the relevant parameters of the qubit. The second plot is the qubit system viewed upside down so that the actual pads of the qubit can be seen within the coupler between the readout and lattice cavity.

Independent Design Parameters:

ω_l Frequency of the lattice cavity. This is controlled most directly by the length of the post of the cavity, though it changes depending on how much the qubit is in the cavity, due to the high dielectric constant of sapphire and the coupling to the qubit.

ω_r Frequency of the readout cavity. This is also controlled by the length of the post in the readout cavity.

E_C The energy stored in the capacticance of the transmon. This is controlled largely by the size and geometry of the pads of the qubit

E_J The energy stored in the Josephson junction. This is set by the resistance of the junction, which is determined by the junction area and the thickness of the oxide layer between the junction pads

g_l Coupling of the lattice cavity mode to the transmon. This is largely controlled by how much the pads of the transmon align with the electric field of the lattice cavity.

g_r Coupling of the readout cavity mode to the transmon. This is largely controlled by how much the pads of the transmon align with the electric field of the readout cavity.

Q_c Coupling quality factor determined by how strongly the measurement antenna is coupled to a cavity.

Q_l Internal quality factor of a cavity mode.

Dependent Parameters

$2\chi_l$ The amount the frequency the lattice mode changes when the transmon is excited from the g to the e state. Determined by $\chi_l = \frac{g_l^2}{\Delta_l} * \frac{\alpha}{\alpha+\Delta_l}$, where Δ_l is the frequency difference between ω_l and ω_q

$2\chi_r$ The amount the frequency of the readout mode changes when the transmon is excited from the g to the e state. Determined by $\chi_r = \frac{g_r^2}{\Delta_r} * \frac{\alpha}{\alpha+\Delta_r}$, where Δ_r is the frequency difference between ω_r and ω_q

α Nonlinearity of the transmon. This is the energy difference between the transmon energy levels. This is equal to E_C

ω_q Frequency of the g to e transition of the transmon. This is set by E_J and E_C by the formula $\omega_q = \sqrt{8E_JE_C} - E_C$

K_l Self Kerr shift of the lattice mode. This is the difference in energy between the $0 \longrightarrow 1$ transition and the $1 \longrightarrow 2$ transition of the lattice mode, caused by coupling to the anharmonic transmon. This can be calculated by $K_l = \frac{\chi_l^2}{\alpha}$

K_r Self Kerr shift of the readout mode. This is the difference in energy between the $0 \rightarrow 1$ transition and the $1 \rightarrow 2$ transition of the readout mode, caused by coupling to the anharmonic transmon. This can be calculated by $K_r = \frac{\chi_r^2}{\alpha}$

To plan the design parameters of the qubit, we first must look at constraints due to the lattice. The frequency of the lattice is set to ~9 GHz by the frequency of the YIG cavities. For the first iteration of tests we want the transmon to be off resonant to the lattice, so that it is not its own lattice site but is just imparting its nonlinearity to a lattice site. Thus we set the qubit frequency at ~8 GHz and the readout resonator frequency to 10 GHz so that both the transmon and the readout resonator are detuned by 1 GHz, which keeps the Purcell loss from the low quality factor readout resonator low but keeps the detuning low enough that the transmon can interact with the lattice modes.

With the frequency set, the next parameters to decide are the E_J, E_C, g_r,and g_l. The ratio of E_J to E_C sets the lifetime limit caused by the charge noise [10] and needs to be greater than ~75 in order to keep the lifetime of this loss channel above 100μs. Considering that

ratio combined with the frequency formula for the qubit, we settle on a E_C of ~300 MHz and E_J of 24.7 GHz. This gives a qubit frequency of 8 Ghz and $\frac{E_J}{E_C}$ of 82. Next, to get the E_c to the right value we change the pad sizes of the transmon. However, the couplings to each of the 3D cavities are also determined by the pad geometry. Using a finite element solver (ANSYS' HFSS), we can adjust the position of the qubit and the shape of the pads until E_C, g_r, and g_l reach the correct values. Aligning the pads of the qubit more with the cavity fields increases the couplings and decreases the E_C (increasing capacitance lowers E_C), while increasing the pad size of the qubit in a direction that does not align with the electric field of the cavities largely just decreases E_C. Thus by shaping the pads all of the parameters can be tuned to desired values. A large g_r and g_l are useful since these determine many important factors in the 3D qubit, such as the Self Kerr shift of the lattice mode and the photon swap rate between the qubit and the lattice, but there are also drawbacks to making them too large. Since the readout resonator is lossy, having a large g_r can Purcell limit the lifetime of the transmon. The Purcell limited lifetime from the readout resonator can be calculated as following:

$$t_P = \frac{\Delta_r^2}{g_r^2} * \frac{Q_r}{2\pi c \omega_r} \tag{5.1}$$

We do not want to be limited by Purcell loss, so we set a g_r of ~75 MHz to keep the Purcell limit t_1 at 100μs. Purcell loss due to g_l is also a factor, though it is less important since the lattice mode has a high quality factor. For the first iteration of experiments we used a g_l of 125 Mhz since this allows swap times between the transmon and lattice site of 100 ns (much lower than particle lifetimes), while still minimizing Purcell loss and keeping the system well within the well-understood dispersive limit. This coupling size could be increased for better performances.

One last important factor is the coupling of the measurement antenna to the cavity modes.

For the readout cavity, a Q_c of ~20000 is desirable since it gives fast readout times while not Purcell limiting other modes in the system. However, coupling this strongly to the mode can be difficult for different cavity geometries. For this system, the antenna is inserted through the bottom of the readout cavity as shown in Figure 4.6. In order to couple strongly to the mode, the antenna needs to be close to the post, as that is where the electric field is the strongest. However, if an antenna is too long, then it will support modes near the resonance frequencies of the system. These modes will naturally have an extremely low quality factor (~10) and will drastically limit the lifetimes of the system. By inserting the antenna through the bottom of the cavity rather than mounting it on a lid on the top of the cavity, we can get the desired Q_c while not generating any antenna modes near the frequencies of our system.

5.2 Fabrication of the Transmon

The transmon is made by depositing aluminum onto a sapphire wafer using a procedure that involves only a single patterning and deposition step. The junctions are Manhattan-style junctions. The specific recipes can be found in Appendix A.

5.3 Cavity QED with a Single Transmon Dispersively Coupled to a Single Decoupled Lattice Site

The first experiment coupled a transmon to a single site of the lattice while the rest of the lattice was detuned. Effectively, this was a system with only one lattice mode. As stated in section 5.1, we coupled the qubit to both a readout resonator and storage resonator. The transmon chip was clamped in a copper holder that is then mounted on the side of the niobium lattice. There is one measurement port strongly coupled to the readout cavity which means that all of the measurements performed are reflection measurements. The

sample was then cooled in a dilution refrigerator to 20 mK. The Hamiltonian for the system in the dispersive limit ($\Delta >> g$) is given by [10]:

$$\frac{H}{\hbar} = (\omega_r + \frac{g_r^2}{\Delta_r}\hat{\sigma}_z)\hat{a}_r^\dagger\hat{a}_r + (\omega_l + \frac{g_l^2}{\Delta_l}\hat{\sigma}_z)\hat{a}_l^\dagger\hat{a}_l + \frac{1}{2}(\omega_q + \frac{g_r^2}{\Delta_r} + \frac{g_l^2}{\Delta_l})\hat{\sigma}_z \tag{5.2}$$

This Hamiltonian illustrates why this design is a convenient system in which to study a qubit. Grouping the $\hat{a}^\dagger\hat{a}$ terms, we can then read off the frequency of the mode that is mostly readout cavity.

$$\omega_{dressed} = \omega_r + \frac{g_r^2}{\Delta_r}\hat{\sigma}_z$$

This frequency of the cavity that is now modified because it is coupled to the transmon is known as the dressed state of the cavity. The frequency shift of $\frac{g^2}{\Delta}$ is dependent on how many photons are trapped in the transmon, because the frequency of the transmon changes with photon number, which changes Δ. This allows us to measure the state of the qubit by observing the frequency of the readout cavity. However, the transmon is not just a two level system, and the higher levels both influence the dressed frequencies of the resonators as well as play a part in photon swaps between cavities. Intuitively, a transmon is in the first excited state now has access to both the ge transition and the ef transition, so that now both transitions Stark shift the cavity mode. If a single extra level is taken into account, the number frequency shift changes to [66]:

$$\chi = \chi_{ge} - \frac{\chi_{ef}}{2}$$

$$\chi = \frac{g^2}{\Delta_r} - \frac{(\sqrt{2} * g)^2}{2 * (\Delta_r + \alpha)}$$

$$\chi = \frac{g^2}{\Delta_r}\frac{\alpha}{\Delta_r + \alpha} \tag{5.3}$$

As for the transmon mode, it also has a dressed state in this system:

$$\omega_{ge} = \omega_q + 2\frac{g_r^2}{\Delta_r}(\hat{a}_r^\dagger \hat{a}_r + \frac{1}{2}) + 2\frac{g_l^2}{\Delta_l}(\hat{a}_l^\dagger \hat{a}_l + \frac{1}{2}) \tag{5.4}$$

The qubit frequency is also sensitive to the number of photons in both the readout cavity and the lattice. This is useful to measure the number of photons in the lattice modes.

For the first set of measurements, a qubit is coupled to a single lattice site with no magnets present in the lattice during these measurements. Later in this section we compare these results to measurements with the exact same setup except with magnets placed in the lattice in the locations which allow them to tune all the lattice sites to the same frequency. To reiterate, these measurements still have a qubit coupled to a single lattice site, but all other sites are detuned.

The first measurement that is done is single-tone CW (continuous wave) spectroscopy by a PNAX network analyzer. The network analyzer tones are constant tones that are easily swept in power and frequency which makes preliminary measurements to map out the frequencies of the modes quick and easy. A single tone is swept in both frequency and power near the frequency of the readout resonator. Results from such an approach are shown in Figure 5.3, which were taken with a separate sample than the rest of the data. Single-tone was only done with the pulse setup for the qubit that we ended up coupling to the lattice. At low powers, the linewidth of the resonator is measured to be 0.5 MHz, and Q_c is measured to be 20,000. The readout resonator is nonlinear as expected, with three separate behavioral regimes. At the lowest powers, the readout resonator is linear. At higher powers, the resonator becomes nonlinear until it eventually snaps into the bare cavity frequency of 8.884 GHz. The shift

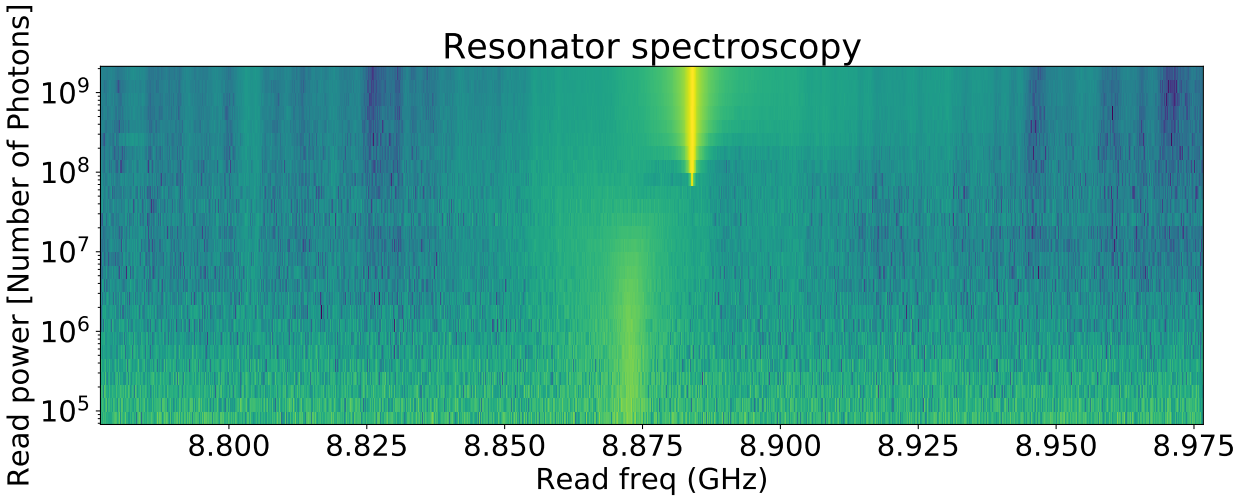

Figure 5.3: Single tone spectroscopy of a resonator coupled to a qubit. This is a different sample than will be used later. No magnet is in this particular sample, and there is only one cavity mode which has a low coupling quality factor. The frequency of the resonator is broad and lower frequency at low powers, but at high enough powers it snaps into the saturated high power peak.

between low power and high power is $\frac{g_r^2}{\Delta_r}$. Here we measure a shift of 11 MHz, which when combined with the measurement of Δ_r in the next plot yields a g_r of 118 MHz. The added magnetic field has no noticeable effect on the readout spectroscopy.

Next, we use two-tone spectroscopy to measure the frequency of the qubit. We input a constant tone at the readout cavity frequency in the low power regimes (still 18 million photons at the cavity), then sweep a tone near the qubit frequency. The response at the frequency of the readout cavity is measured. If the transmon mode is excited, then the readout cavity frequency will change, which will change the response at the orignal readout frequency. This allows us to map out the transmon modes of the system. Plots of a two tone spectroscopy measurement are shown in Figure 5.4. At low power, we can see the transmon transitions. The highest frequency transition is the $g \longrightarrow e$ transition at 7.814 GHz. The next highest frequency is the $e \longrightarrow f$ transition. The separation between the two modes is measured at 352 MHz. This is α, the anharmonicity of the qubit. We can also switch the two tone spectroscopy around by putting a constant tone on the qubit frequency and then

sweeping the second tone and measurement port near the readout cavity. This allows us to see the frequency shift of the resonator when the qubit is excited. This frequency is the χ shift which can be used to back out g_r. We measure a χ shift of 225 MHz and a g_r of 75.

The next stage of measurement involves setting up pulse sequences. To do this we use a PXI Chassis. The setup generates pulse trains at up to four different frequencies. For the first few measurements, we use only a tone at the readout cavity frequency and a tone at the qubit frequency. In order to test the setup, we first sweep a single tone near the readout cavity frequency. The response is shown in Figure 5.5. The two curves are the I and Q quadratures from the mixers. From the readout spectroscopy we get a frequency of 10.5835 GHz to monitor during the next qubit measurements.

After the readout resonator is located, we look for the qubit by sweeping a pulse near the qubit frequency and measuring if there is a change in transmission of the readout cavity. The results of this measurement with different pulse powers are shown in Figure 5.6 for setups both with a magnet and without a magnet. Using the pulse setup, we measure a qubit frequency of 7.814 GHz. The response in the I quadrature is much stronger than the Q response. This means the χ shift changes the response more since it is small compared to the linewidth of the readout resonator. From here forward we will plot only the response in the I quadrature. To measure the χ shift, we also pulse the qubit and then do a frequency sweep measurement near the readout resonator. This is shown in Figure 5.5b. The amount the peak shifts compared to the measurement in Figure 5.5 is a direct measurement of the χ shift. For this setup we measured a shift of 450 kHz or $\chi = 225$ kHz.

Once this frequency is found, we make a Rabi measurement. For this measurement we pulse the cavity at the qubit frequency and measure out on the readout cavity as a function of the length of the pulse. The results are shown in Figure 5.7. The qubit Rabi flops between the g and e state at a frequency that is dependent on the power applied. The Rabi frequency is useful because it provides information on the pulse time and power which most

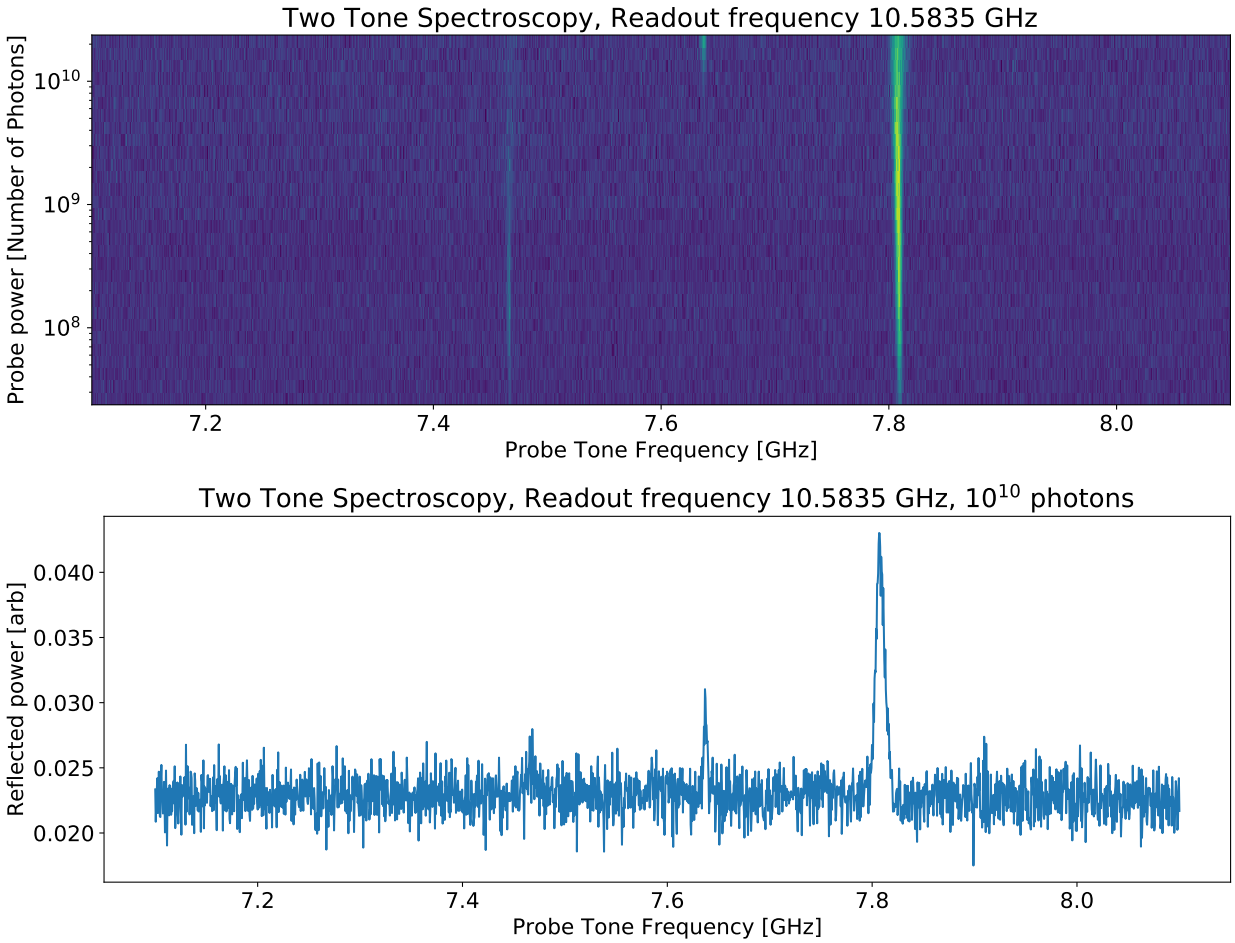

Figure 5.4: **Top.** Two tone spectroscopy of the qubit coupled to the readout resonator. A constant tone is input into the readout cavity at 10.5835 GHz and the response at this frequency is measured. A second tone is swept near the qubit frequency. When the qubit is excited, it shifts the frequency of the readout resonator and the measured response at the readout frequency. The power of the qubit probe is then swept to see high power two photon transistions. **Bottom.** A single slice of the previous measurement at a power of 10^10 photons.

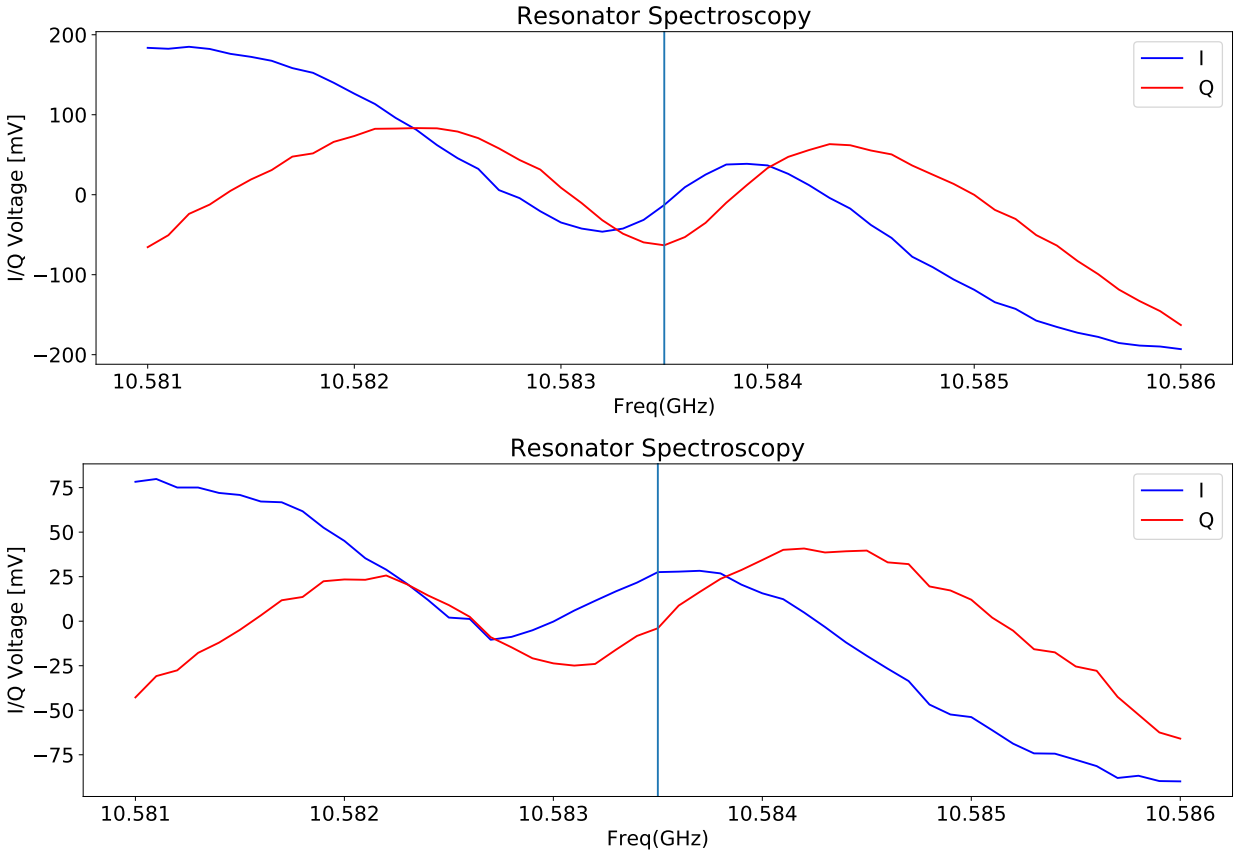

Figure 5.5: **Top.** Pulsed resonator spectroscopy of the readout cavity. The resonator frequency is at 10.5835 GHz. **Bottom.** Pulsed resonator spectroscopy preempted by a π-pulse at the qubit frequency. The shift is 450 kHz and equal to 2χ. Using equation 5.3, we calculate a g_r of 75 MHz.

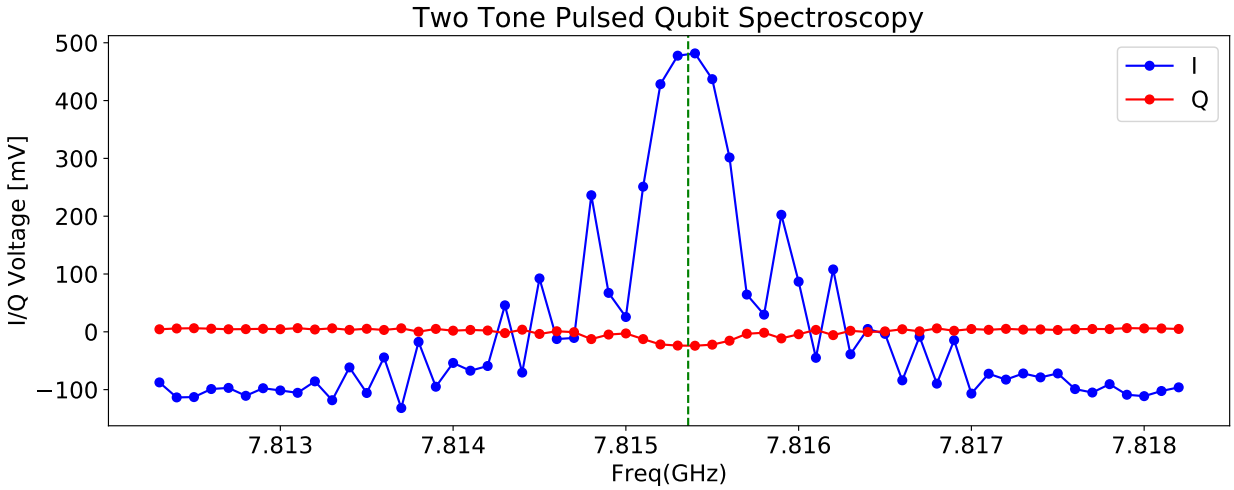

Figure 5.6: In the plot we show the response of the system to sweeping a pulsed tone near the qubit frequency we measured in Figure 5.4 (~7.815 GHz) and then immediately measuring the transmission through the readout resonator. The two curves shown are from the I and Q ports of a mixer, since the response is mixed down to DC in order to be measured by the PXI setup. We measure a qubit frequency of 7.81536 GHz from this measurement.

efficiently switch the qubit from the g to the e state. With these parameters we can then do a t_1 measurement and a Ramsey experiment. The t_1 measurement involves π pulsing the qubit to the e state, then measuring how long it takes the qubit to decay by measuring the readout resonator as a function of time. The qubit t_1 plots for both lattices with a magnet and without a magnet are shown in Figure 5.8. The t_1 of the lattice without the magnet is 9 μs, while the t_1 with the magnet decreased to 3 μs. This t_1 is substantially lower than state of the art (in our lab we have routinely made qubits $> 100\mu$s t_1), but still substantially longer than swap times (see later in the section) and lattice tunneling times ($\sim$ 50 ns without a topological band structure, $\sim$ 7 ns in the chiral edge modes).

Next, we measure t_2 of the qubit using a Ramsey measurement. This involves first $\frac{\pi}{2}$ pulsing the qubit to the g+e state, then waiting for a variable amount of time, and then $\frac{\pi}{2}$ pulsing the qubit once again. This measures the dephasing rate of the qubit. We measure a dephasing rate in the magnet-free sample of 7μs, which is lower than the t_1. This means our limiting source of loss in this sample comes from dephasing, not decay from e to g. For the sample

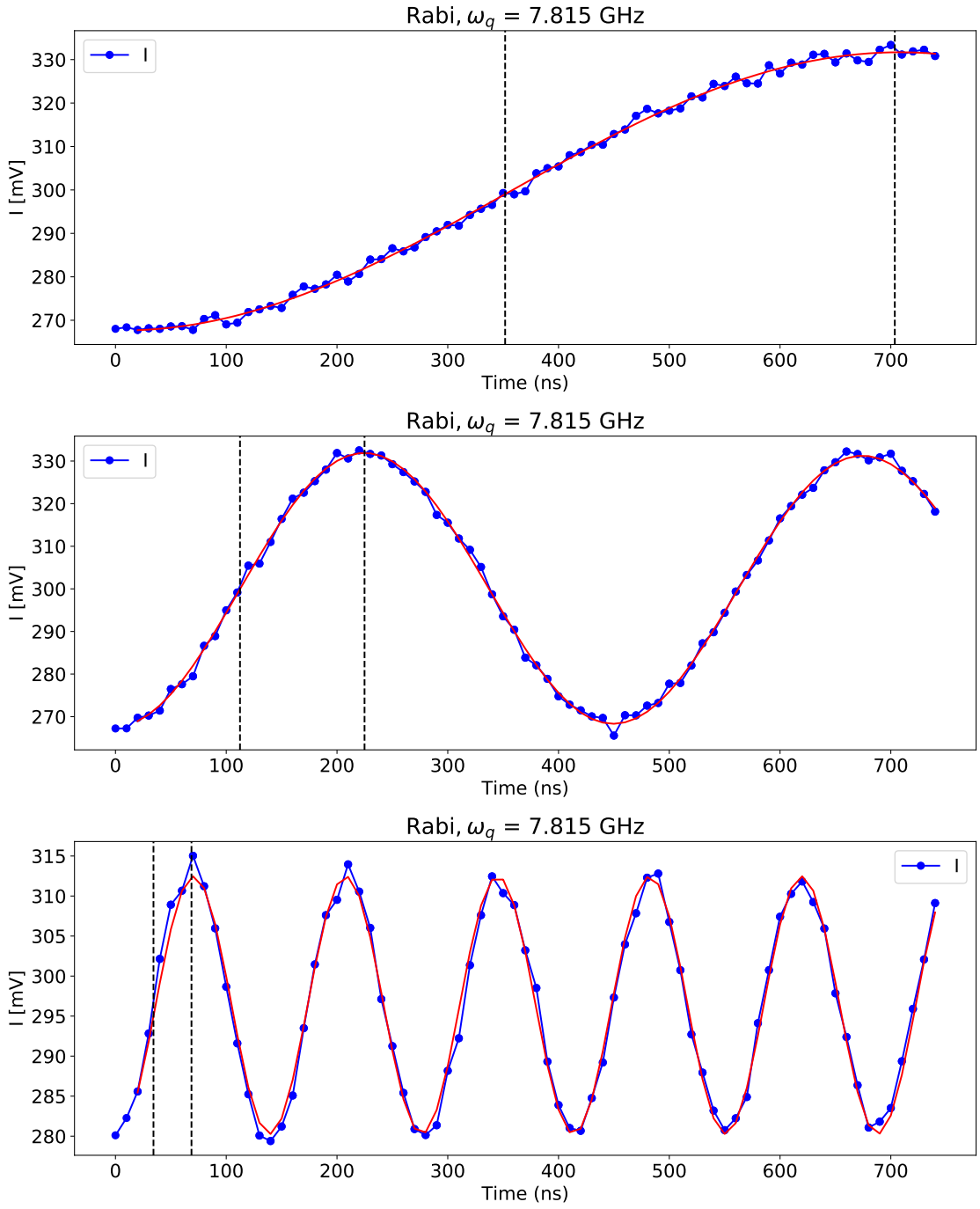

Figure 5.7: Rabi oscillations of the transmon $g \longrightarrow e$ transition. The transition frequency is pulsed for a swept time and then the transmission through the readout cavity is measured immediately afterward. Plots from top to bottom show increasing the power of the drive on the transition. Stronger drives result in faster oscillations.

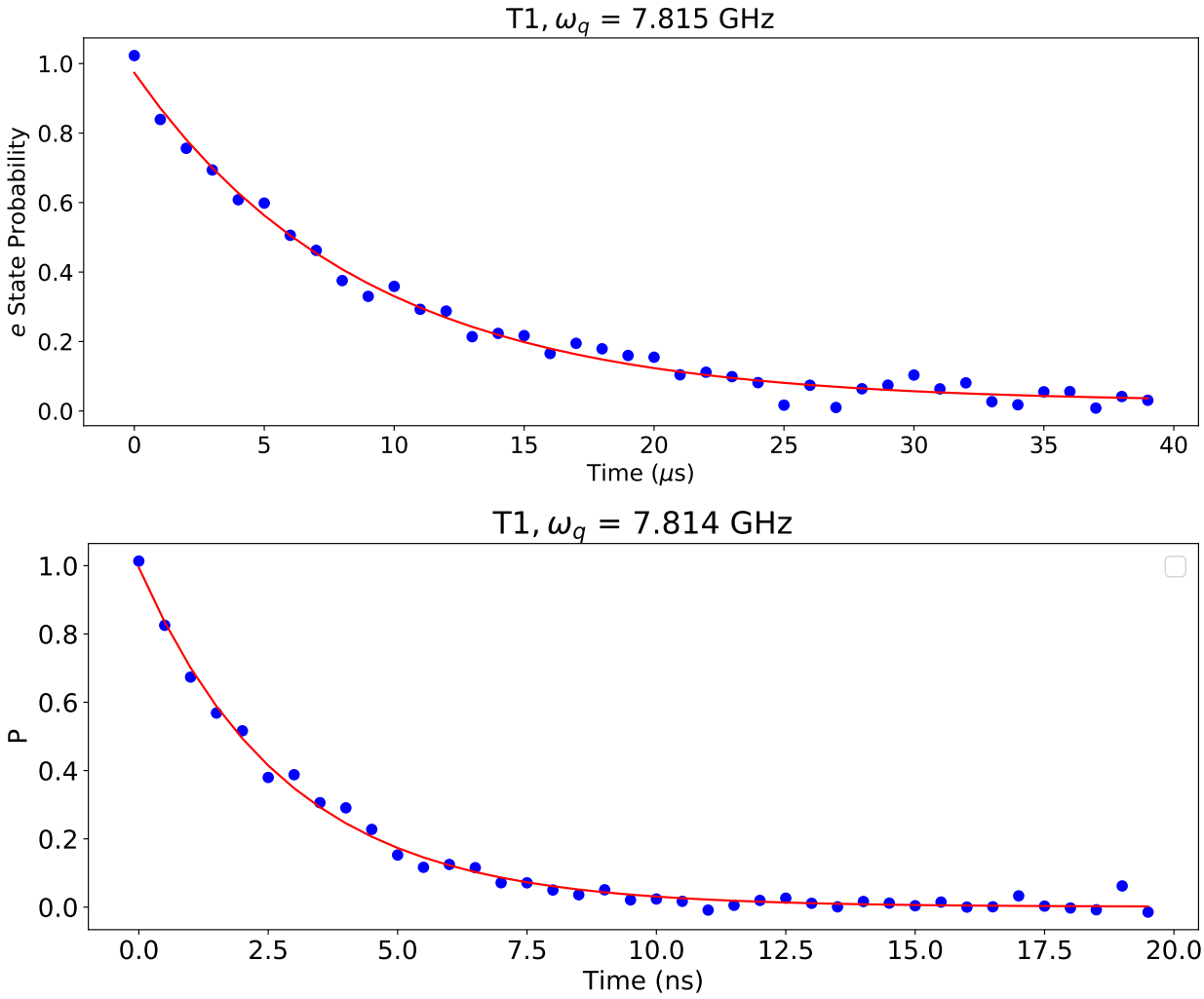

Figure 5.8: t_1 measurements of the transmon mode. The qubit is π-pulsed to the e state, then the transmission through the readout cavity is measured after a varied time. The qubit decays exponentially as a function of time, and this can be fit to extract the t_1. **Top.** t_1 measurements with no magnet in the lattice. The t_1 is 9μs. **Bottom.** t_1 measurements with a magnet in the lattice. The t_1 drops to 3μs.

without the magnet, the t_2 is measured to be 4μs, which is higher than the t_1 in this sample. Also, the Ramsey measurement can measure the frequency of the qubit accurately. The frequency of the fringes are set by the difference between the qubit frequency and the drive frequency, so the Ramsey measurement is an accurate measurement of the qubit frequency. The qubit frequency without a magnet is 7.815, GHz while the qubit frequency with the magnet was 7.814 GHz.

After characterizing the $g \longrightarrow e$ transition, we then turned to characterizing the $e \longrightarrow f$ transition, because this information will be used to measure the qubit temperature and the higher levels will be used in qubit gates and swaps. First we went through similar measurements so that we know if any of these states could be dominant loss sources. Figure 5.9 has these measurements and shows that these modes and transitions have similar lossiness. First we find the higher frequency transitions with an experiment identical to the experiment we used to find the $g \longrightarrow e$ transition. This transition has a much weaker signal since a cold qubit is naturally in the g state most of the time. Next, we did two Rabi experiments: the first one was done immediately after the qubit was π-pulsed to the e state, and the second one is done without any π pulse. We can compare the amplitudes of the Rabi oscillations to get a measurement of the qubit temperature. Essentially, this is the measurement of the probability of the qubit being in the g state versus the e state.

After these measurements were taken, we pushed on further using only the sample that included a magnet. We wanted to demonstrate a swap between excitations in the qubit and the lattice site, so that we could potentially load or unload single qubits into the edge states of the lattice. Before performing this swap, we needed to find the frequency of the lattice mode and measure the χ shift between the qubit and this mode, denoted as χ_L. In order to do this, we first swept a tone near the expected lattice mode frequency (8.9 GHz), then pulsed at the qubit frequency, and finally measured transmission through the readout resonator. If we hit the lattice mode frequency, then the qubit mode frequency would shift,

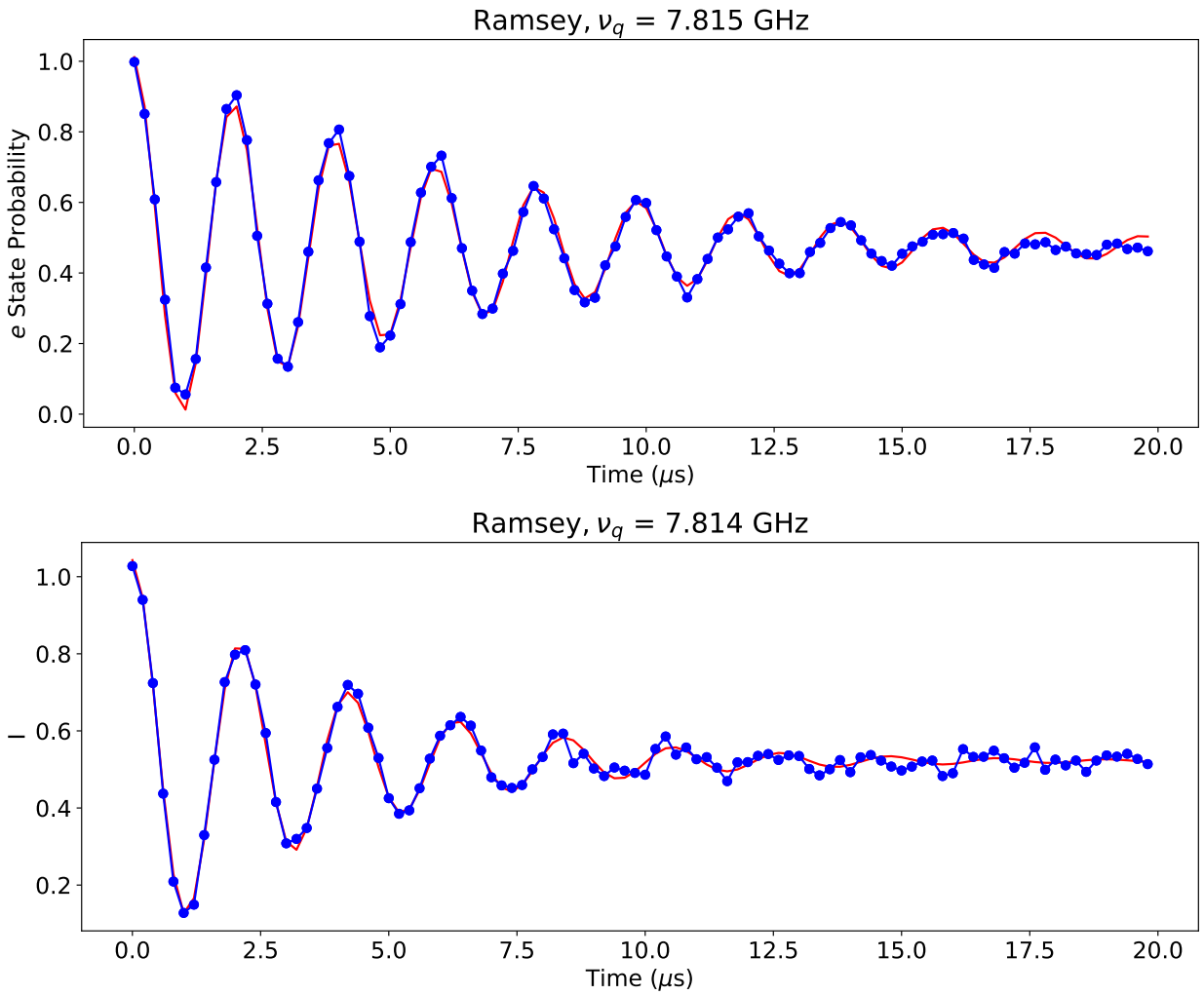

Figure 5.9: Ramsey measurements of the transmon mode. These measurements yield values for the t_2 of the qubit, as well as accurate measurements of the qubit frequency. **Top.** Ramsey measurement in the sample with no magnet. The t_2 is 7μs and the measured qubit frequency is 7.815 GHz. **Bottom.** Ramsey measurement in the sample with a magnet. The t_2 is 4μs and the measured qubit frequency is 7.814 GHz.

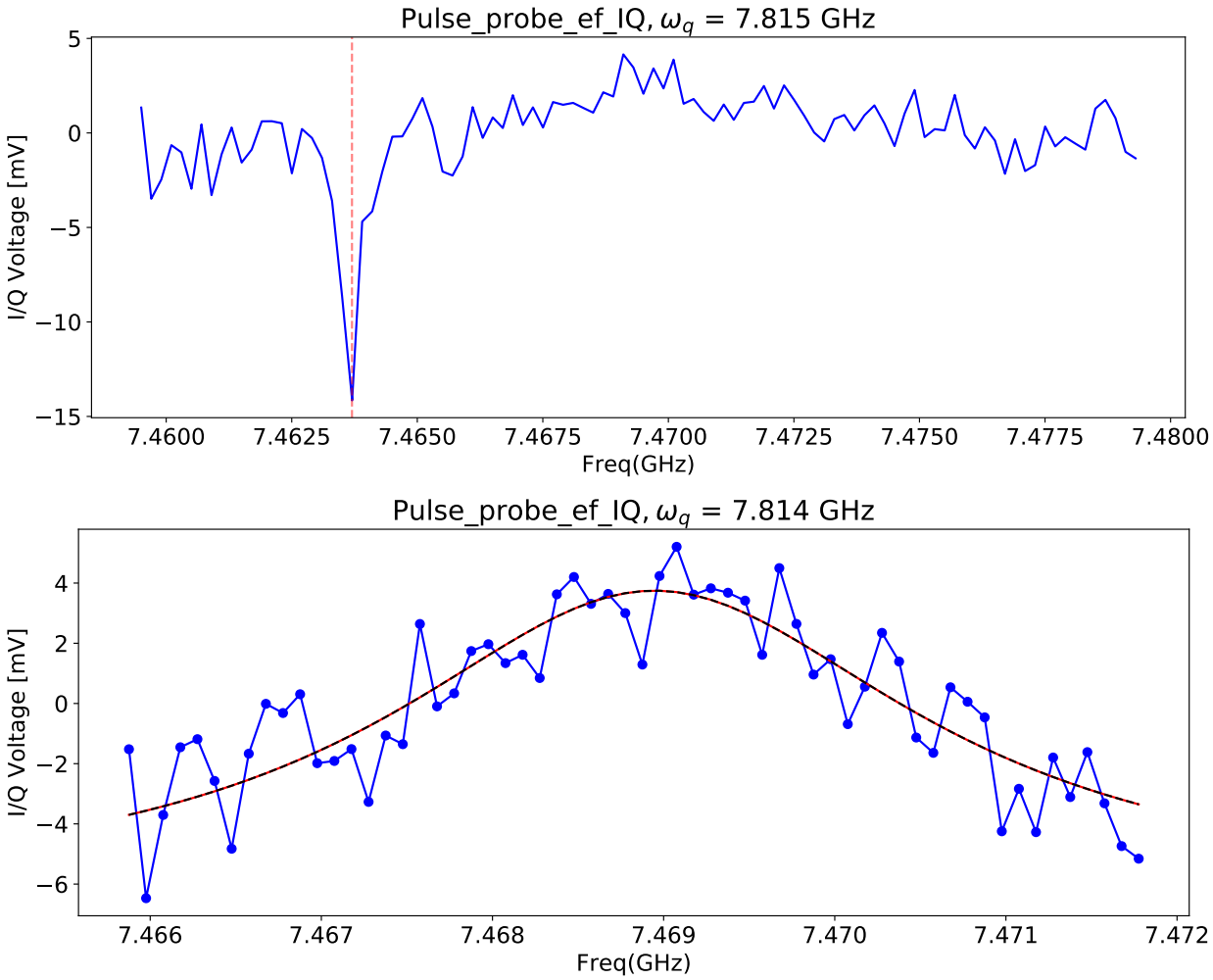

Figure 5.10: Qubit ef transition frequency measurements, performed exactly like the ge transistion measurements. **Top.** ef transition with no magnet. The transition is at 7.463 GHz. **Bottom.** ef transition with the magnet. The peak broadening occursbecause more power was used in this measurement. The transition is at 7.469 GHz.

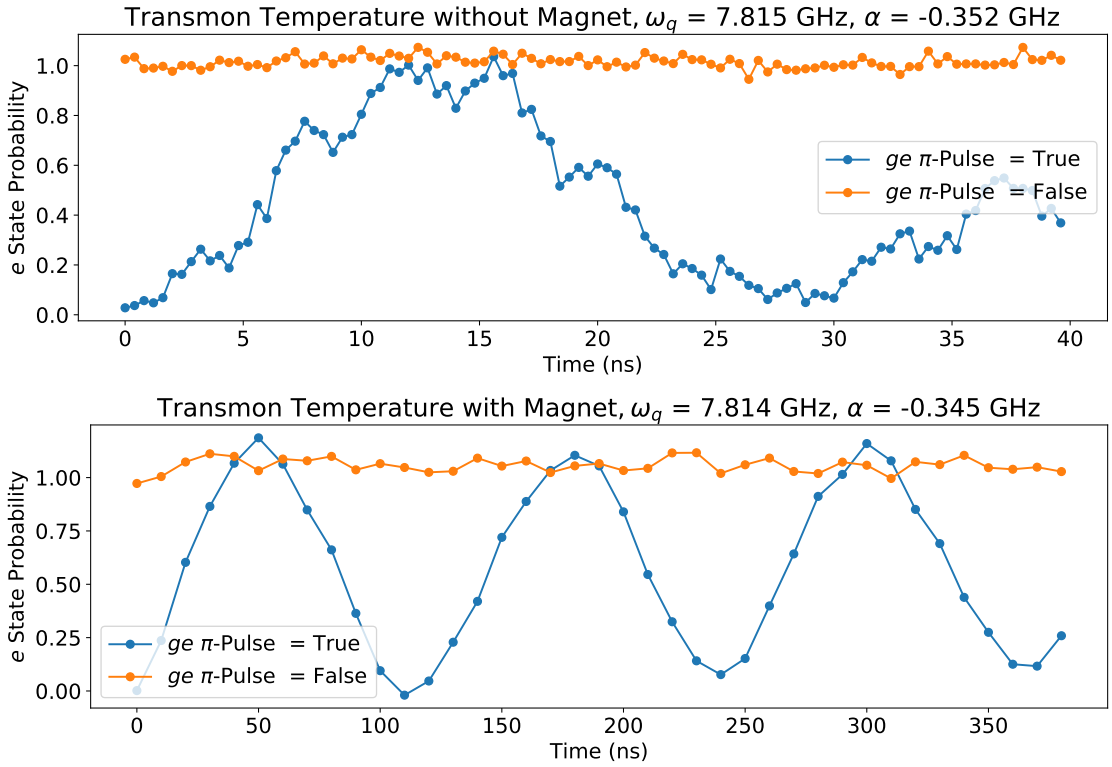

Figure 5.11: Measurement of the qubit temperature. This is done by comparing the Rabi oscillation amplitude of the $e \longrightarrow f$ transition when either a π-pulse to the e state is done before the measurement or not. The ratio of the amplitudes is a probability of being in the e state vs. the g state. **Top.** Qubit temperature with no magnet. The temperature is measured at 100 mK, though these temperatures are very rough since the Rabi oscillations not *pi*-pulsed are hard to fit since they are so small. **Bottom.** Qubit temperature with a magnet. The temperature is measured at 200 mK, though the signal to noise ratio for the Rabi oscillations not π-pulsed is very low.

so that the readout resonator will not be shifted by the now off-resonant pulse on the qubit. The results of this measurement are shown in Figure 5.12. The lattice mode frequency is measured at 8.9009 GHz. Next, to measure χ_l, we switch the constant tone to 8.9009 GHz and then performed the sweep near the qubit frequency. After lowering the power so that on average approximately one photon is in the lattice mode, we see the plot shown in Figure 5.12. The two peaks are the frequencies of the qubit when the lattice is populated with either 0 or 1 photon. The splitting between the modes is measured to be 10.6 MHz, which makes $\chi_l = 5.3$ MHz. We can use χ_l to determine g_l as well using equation 5.3, obtaining a g_l of 155 MHz.

Next we wanted to determine the loss for the $e \longrightarrow f$ and $g \longrightarrow f$ transitions, since these will be used in the swap and will dominate the loss. Fig. 5.13 shows these measurements and the resulting t_2 times of 2.0 seconds and 1.6 seconds respectively.

In order to perform a swap between the qubit mode and the lattice mode, we look at the Hamiltonian of a strongly driven system in order to identify the available schemes to transfer an excitation. Driving the Hamiltonian can make many terms that were previously negligible in the rotating wave approximation large (dependent on the drive strength). By adding a drive term $\omega_d = 2\omega_q + \alpha - \omega_l$ with drive strength Ω_d, we can get a swap term in the Hamiltonian like this:

$$\frac{H_{swap}}{\hbar} = -2\sqrt{\chi_r \chi_l}[\Omega_d(\hat{a}_q^\dagger)^2 \hat{a}_l + \Omega_d^*(\hat{a}_q)^2 \hat{a}_l^\dagger] \tag{5.5}$$

This specific term converts two excitations in the qubit to an excitation in the lattice cavity via a drive photon. There are many types of transitions available in this system, but a rule of thumb for which transitions are possible is that four photons are required with a drive photon that is at a frequency of the difference between the qubit photons and the lattice photons. For example, another possible transition would be between one excitation in the

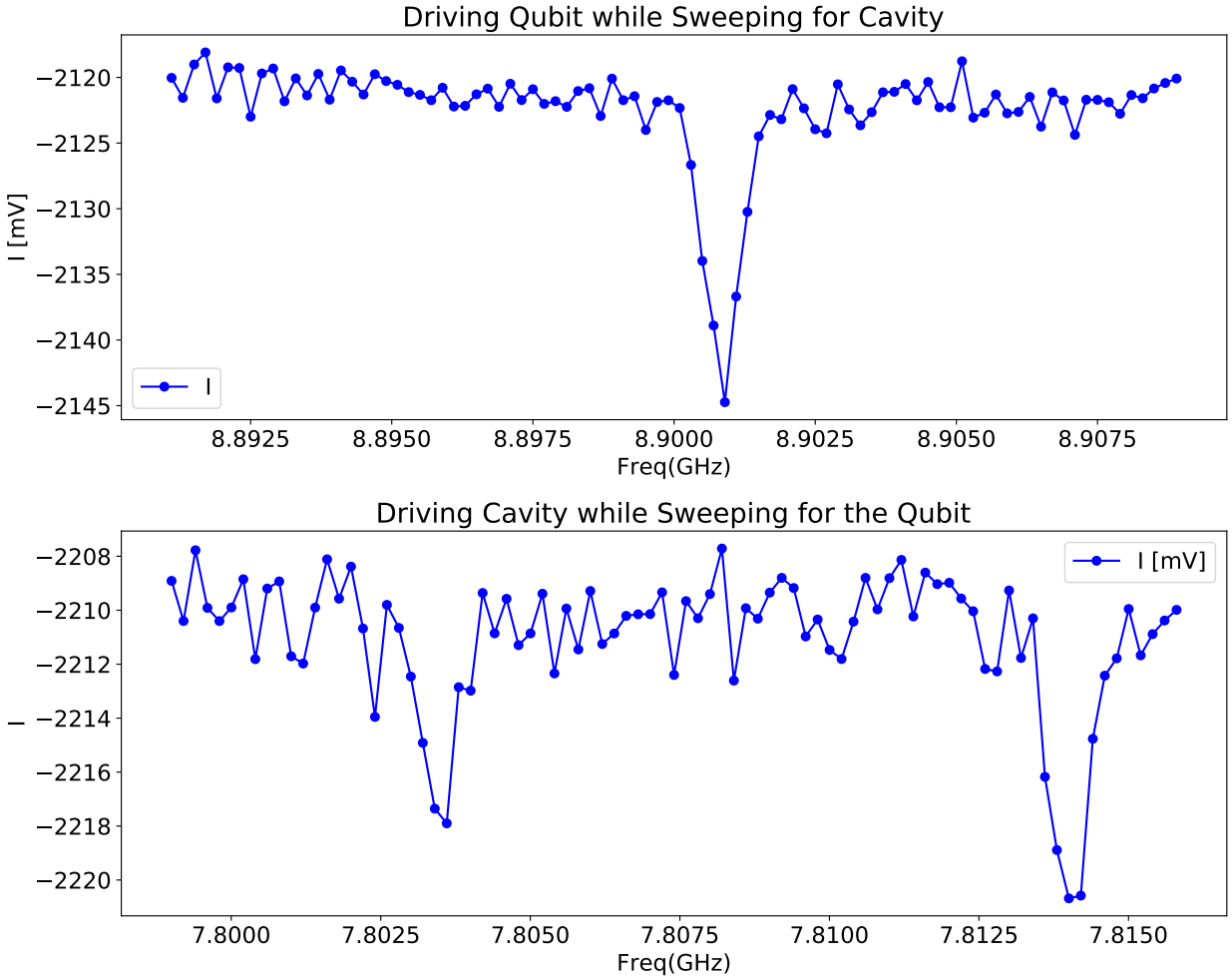

Figure 5.12: Measurements done to ascertain the frequency of the lattice cavity mode and the χ shift between the lattice mode and the qubit (χ_l). **Top.** In this measurement we first sweep a drive near the lattice mode frequency, then π-pulse the qubit and perform readout. If the drive excites the cavity, then the qubit frequency will shift and the π-pulse will be off-resonant to the qubit. This changes the readout transmission signal and allows us to find $\omega_l = 8.9009$ GHz. **Bottom.** We then drive the lattice frequency very weakly and sweep a tone near the qubit frequency. This allows us to see the number splitting of the qubit when photons are in the lattice cavity, and measure $\chi_l = 5.3$ MHz.

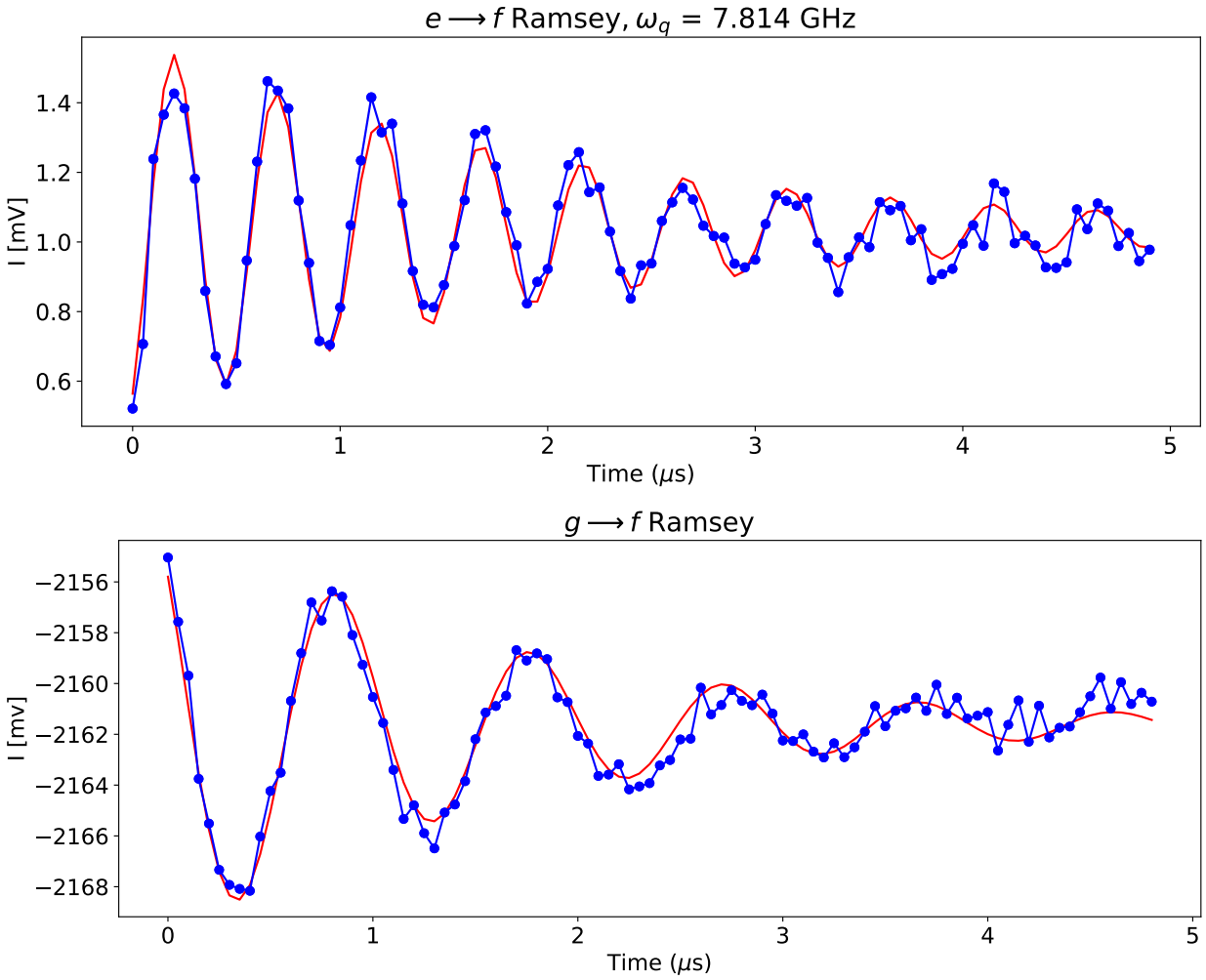

Figure 5.13: Ramsey measurements for the ef and gf transition in the sample with a magnet. The t_2 measurements are 2.0 seconds and 1.6 seconds respectively. The gf t_2 is what dominates the loss of the photon swap procedure.

qubit and two photons in the storage cavity, but this time the drive would need to be at $\omega_d = 2\omega_l - \omega_q$. For this system, ω_d would be at a frequency of 10 GHz, which is hard to amplify to the high powers required to get fast swaps. Fast swaps are required since the swap time should be negligible compared to photon lifetimes.

In order to perform these swaps, we added another input drive that consisted of an I and Q channel from the PXI mixed with a signal generator. We first π-pulsed the transmon to the e state, then π-pulsed the qubit up another level to the f state. Similarly to the way in which we found the cavity transition, we then swept the new drive near $f0$ to $g1$ transition energy, or $\omega_d = (2\omega_q + \alpha) - \omega_l$, which is ~6.83 GHz. After each point on the sweep, the qubit was then π-pulsed back to the e state, so that we can do readout on the calibrated e state. If the swept drive was on resonance with the transition, then less population would be in the f state after the drive pulse, so the qubit would have smaller population in the e state and a change in transmission through the readout cavity would occur. After this frequency was found, we then did a Rabi experiment as shown in Figure 5.14 to calibrate the time needed to π pulse the $f0g1$ transition. Higher rates were desirable since the lifetime of many of these transitions is comparable to the gate times, so photons will start decaying before experiments are finished. In Figure 5.14b, we show the fastest swap to the $g1$ state that we could achieve for the coupling rates of our system, with a time of ~100 ns.

With all of these procedures working in the model with a single site, we then turned our attention to coupling transmons to delocalized edge modes of the lattice.

5.4 Single Qubit Coupled to the Chern Insulator

First we removed the transmon from the lattice and followed the procedure discussed in Chapter 4 to tune the rest of the lattice modes to the 8.9009 GHz, the frequency of the lattice mode with the qubit inside the cavity. We mounted a qubits onto the lattice so that

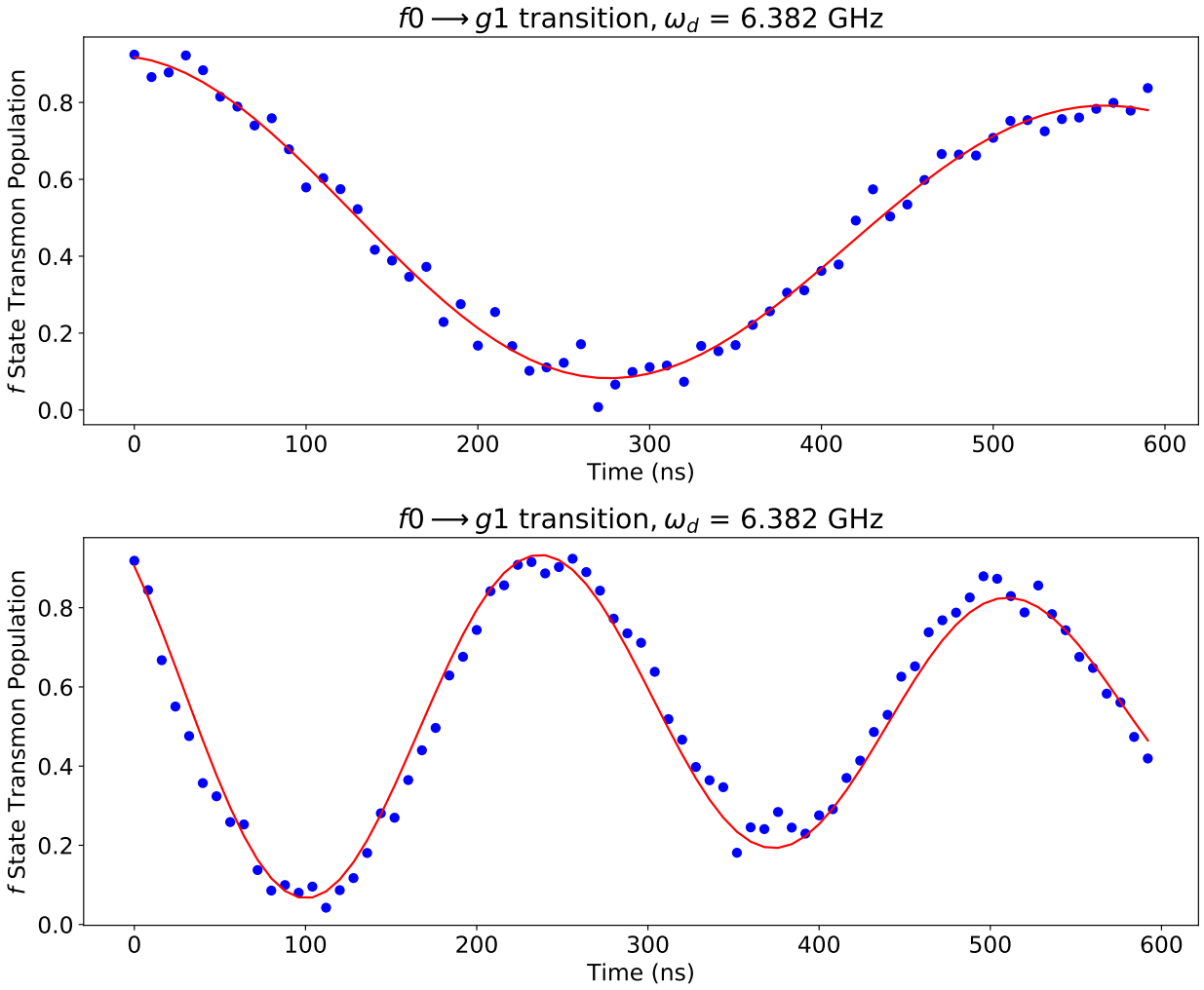

Figure 5.14: Rabi swap between the $f0$ state and the $g1$ state plotted for two different powers. The qubit is first excited to the f state, then a drive pulse is input at 6.832 GHz, which is equal to $\omega_d = (2\omega_q + \alpha) - \omega_l$. The population in the f state of the qubit is plotted as a function of time. When the population of the $f0$ state goes to 0, all of the population is in the $g1$ state. The bottom plot is at twice the power of the top plot, and therefore the flopping rate is twice as fast.

they coupled to a corner site (1,1). The qubit was the original qubit used in section 5.3. We connected one output line to the qubit, one to a single lattice site (5,1), and connected the third to the 10-way Radiall switches in order to be able to measure outputs on 10 of the lattice sites. We used circulators on all three lines so that we could do reflection or readout measurements on the 10 switch lattice sites, the qubit, and lattice site (5,1). We connected the rest of the lattice sites to input lines of the fridge

At the time of this writing we were just beginning to measure the lattice, and I wanted to conclude this section with some of the promising preliminary measurements we made. First, we measured transmission between two bulk cavities (3,3) and (2,3) and compared it to transmission between two edge cavities (1,4) and (3,1) to confirm the existence of a gap in the edge modes where the bulk modes lived. The raw transmission data is shown in Figure 5.15. Similar to the results in Chapter 4, we have edge modes in the top gap located at 8.9244 GHz and 8.9338 GHz, and in the bottom gap at 8.8702 GHz and 8.8749 GHz. There should actually be 3 edge modes according to simulation, so either there is degeneracy (unlikely due to the linewidth being much narrower than the disorder) or one of the edge modes is closer in frequency to the bulk modes and must be probed more thoroughly to see its eigenvector. Next, we varied the power of the CW drive and observed nonlinearity of the edge modes due to being coupled to the qubit. This is shown in Figure 5.15 as well. The modes' frequency shifts changes depending on how much a mode's eigenvector is on the particular cavity being measured, but they reach values of up to 2 MHz.

Last, we then performed $f0 \longrightarrow g1$ swaps into the chiral edge modes in the lower band. We varied the sideband swap tone as a function of frequency and plotted the population in the f mode of the qubit as a function of time. This yields the Rabi "chevrons" of the two modes, indicating we can swap into the chiral edge modes of the cavity. The results are shown in Figure 5.16. The qubit is more strongly coupled to the higher frequency mode, so the π time for the swap is only 300 ns, while the lower frequency mode has a π time of 500 ns. These

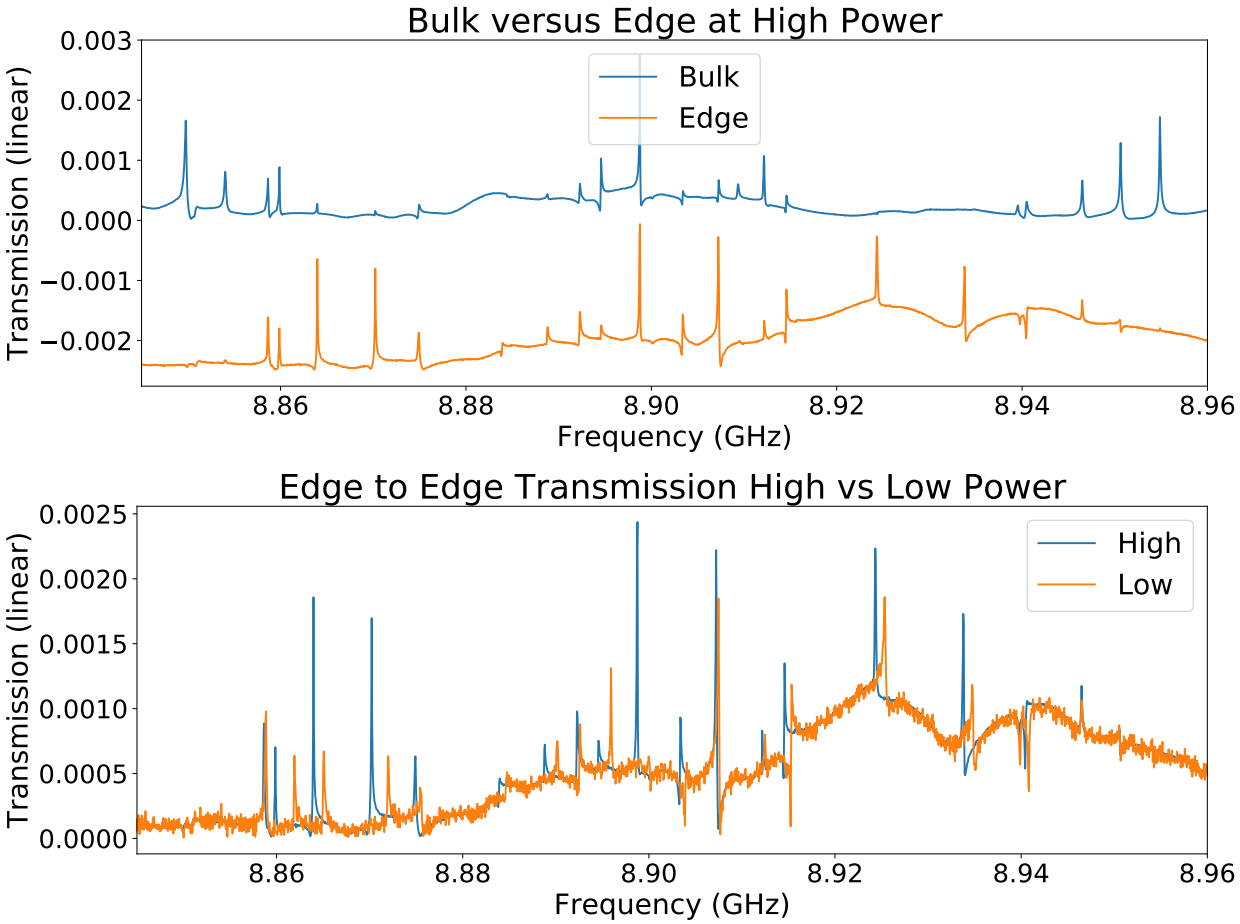

Figure 5.15: **Top.** Comparison of the transmission between to bulk cavities and two edge cavities. As predicted, two large gaps exist in the bulk-bulk transmission and in those gaps there are modes in the edge-edge transmission. **Bottom.** Edge transmission in the high power limit and the low power limit. The modes shift in energy at higher powers, showing that they are strongly coupled to the qubit.

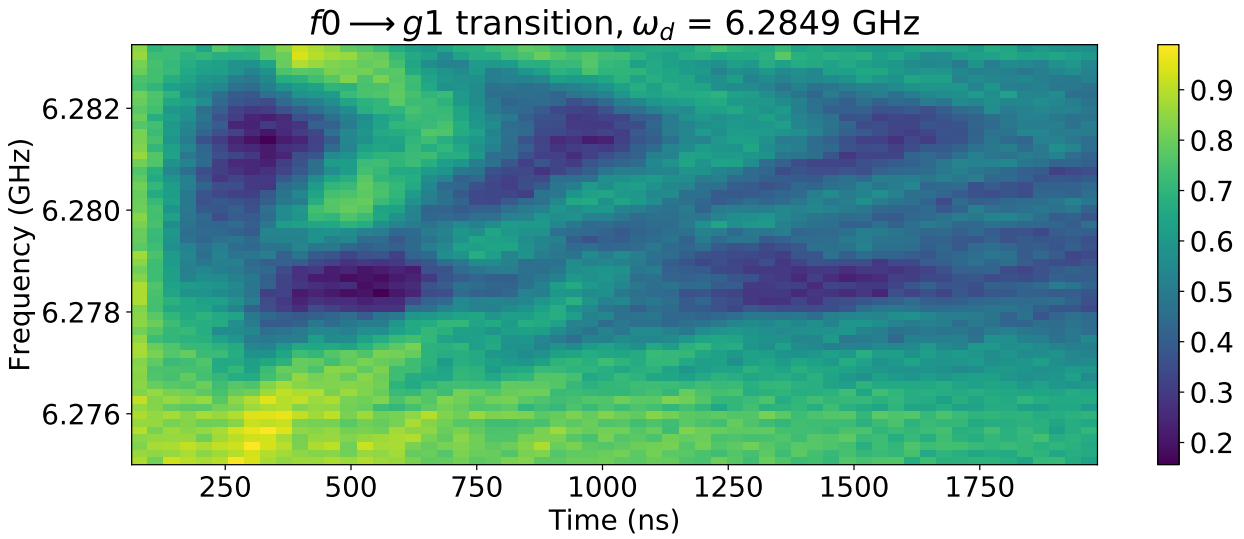

Figure 5.16: Rabi Chevrons of transferring photons from the qubit into the chiral edge modes of the lattice. The qubit is more strongly coupled to the higher frequency mode, so the π time for the swap is only 300 ns, while the lower frequency mode has a π time of 500 ns.

rates are lower than the single cavity $f0 \longrightarrow g1$ swap times since the mode is now more spread out over the lattice, so the coupling to the qubit is smaller.

With these measurements we have demonstrated that we have a system that both breaks time reversal symmetry strongly while interacting strongly with a transmon qubit.

CHAPTER 6

OUTLOOK

This work has pioneered several paths towards making quantum topological materials out of microwave light. We have developed and tested a method to combine strong nonlinearities with time-reversal-symmetry-breaking topology in a low-disorder system where dynamics and eigenmodes are easily measured. This work is easily translatable to Bose-Hubbard model physics as well. Combined with the dissapitive stabilizer [67] developed alongside the Chern insulator we can explore physics with large interactions and arbitrary filling factors. Finally, this system already has the capabilities to explore new physics in chiral quantum optics [14], since we have already coupled single photon emitters to chiral edge channels. Superconducting circuits and cavities are quickly becoming some of the most powerful tools not only to perform universal quantum computation, but also to study quantum materials, condensed matter physics, and quantum optics.

6.1 Fractional Quantum Hall Effect Physics

Our original goal for this project was to develop the technology to simulate fractional quantum Hall physics in our material. While we have demonstrated that this scheme is simultaneously compatible with both requisite interactions, two main technical challenges remain in order to achieve this goal. First, we need to increase the anharmonicities of the lattice modes. This is an interesting problem because the only way to do this is to make the many-body modes more "qubit-like". For small increases in the anharmonicity, we could simply hybridize the modes more strongly by increasing g_l and/or decreasing Δ_l. Our current qubit-cavity system had a χ_l of ~5 MHz, which means that the self-Kerr shift of the lattice mode would be 74 kHz:

$$K_l = \frac{\chi_l^2}{\alpha} = \frac{g_l^4 \alpha}{\Delta_l^2(\Delta_l + \alpha)^2} \tag{6.1}$$

This self-Kerr shift is essentially the interaction energy between particles in the lattice. At these values is much smaller than the tunneling constant, which means that the lattice would be nowhere near the strong interacting/Mott insulator limit where $K_l >> t$. We would need to multiply our current self-Kerr shift by ~300 to just match the tunneling ratio. In order to achieve values this high while leaving α at 350 MHz (α is hard to increase without $\frac{E_C}{E_J}$ becoming too large), Δ_l must become very close to g, which puts the system out of the dispersive regime. This could be a particularly difficult regime in which to work if you are trying to build the simplest fractional quantum Hall material possible since now there would be two modes on every lattice site interacting with all of their neighbors.

Perhaps a cleaner solution would be to effectively invert the lattice, making the sites the transmons and the lattice a dispersive element which the transmons use to virtually couple to each other. I have performed some simulations of this to measure the effective coupling between two qubits in a detuned lattice and I have achieved similar results to what we currently use ($t = 30$ MHz). Since the transmon is where the particles live, the interaction energy would effectively be the α of the transmon. On the other hand, the particles would be much more sensitive to the transmon lifetime, and care would have to be taken to make the transmon's lifetime longer than the current lifetimes I achieved in this work (this is possible- see section 4.5). Another challenge of this approach would be managing the disorder of the transmons. As of the time of this writing, there are not strong methods to either tune single junction qubits or to couple tunable flux qubits to 3D cavities, so one would have to rely on either making many large batches of single junction qubits and post-selecting, or using lattice modes to dispersively shift the qubit into the right frequency. One could imagine adding an extra mode off resonant to the other modes into each lattice site that does not couple to neighbors but does strongly couple to the qubit. Tuning this mode would allow

one to shift the qubit frequency since the qubit frequency is (from equation 5.4) dependent on any coupled cavity:

$$\omega_{ge} = \omega_q + 2\frac{g_r^2}{\Delta_r}(\hat{a}_r^\dagger \hat{a}_r + \frac{1}{2}) + 2\frac{g_l^2}{\Delta_l}(\hat{a}_l^\dagger \hat{a}_l + \frac{1}{2})$$

If an extra cavity was added, another $\frac{g^2}{\Delta}$ term would appear in the qubit frequency. By adjusting this detuning we could shift the qubit frequency. Although this scheme does not scale well to a large number of sites since each cavity-qubit system would have to be individually controlled and tuned, it would allow for large α, low disorder, and long particle lifetimes.

In order to add transmons to each site, I investigated the design shown in Fig. 6.1. In this setup, every site would be composed of the original lattice site, a readout resonator, and a transmon qubit coupled to both resonators. On the opposite side of the lattice, we would machine another lattice made out of readout resonators, but these would be uncoupled to each other. This is possible because the readout cavities are narrower than the lattice cavities. A qubit would be coupled to the resonators by mounting it in a hole between both resonators. This configuration was able to achieve resonator-qubit couplings of 100 MHz while maintaining $\frac{E_J}{E_C}$ ratios of 300.

6.2 Bose-Hubbard Simulations

An extension of these ideas could be applied towards making a 2D Bose-Hubbard simulator. The advantage of going in this direction is that we would not need a magnetic field so all of those restrictions and loss channels associated with applying field would be discarded. To create a quantum material that can probe interesting physics in the regions of the Bose-Hubbard model space which other materials struggle to reach, we would need to find a way

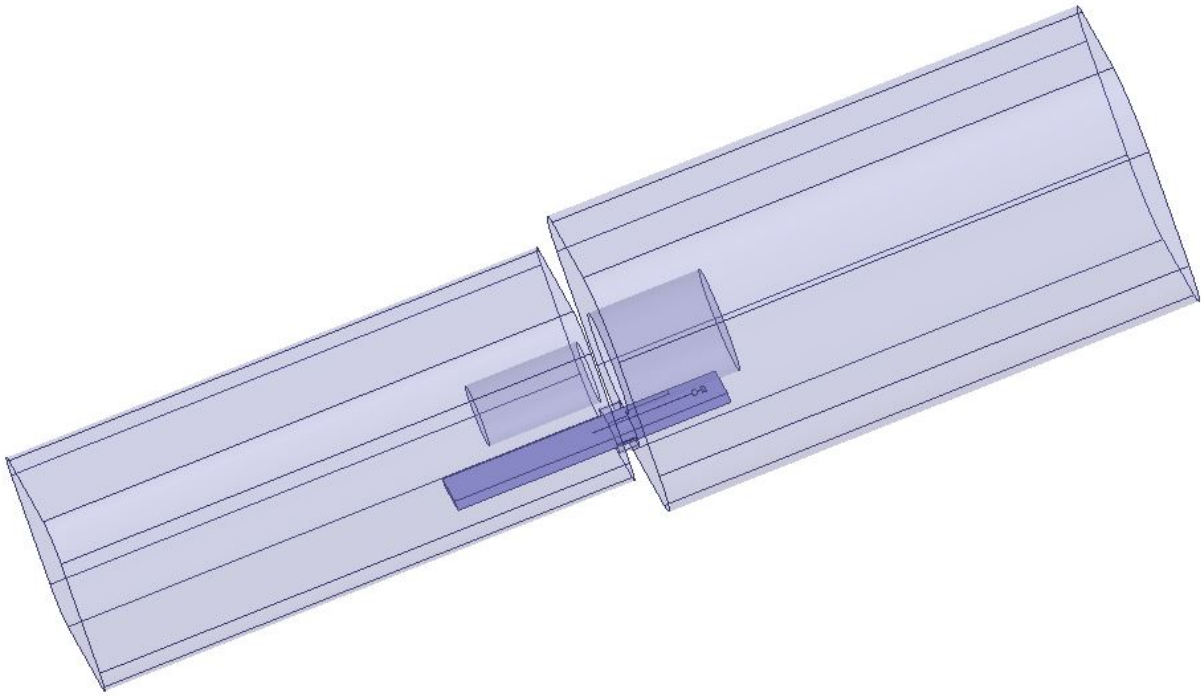

Figure 6.1: Pictured is a single composite site of a possible way to implement a lattice with a qubit and readout resonator for every site. Underneath each lattice site is an inverted readout resonator. This setup would allow for easy machining and access. The qubit is then placed in a channel between the readout resonator and lattice site in order to couple strongly to both.

to tune the filling factor of the number of interacting photons compared to the number of lattice sites. Fortunately, we have designed a photonic autonomous stabilizer [67] that can pump a chain of interacting sites full of photons. This work was done in 2D but could easily be applied to 3D cavities as well. However, pumping the lattice completely full of photons would simply put the material in the Mott insulator regime, which is already well understood. Instead, if we were to block off and stabilize a fraction of the available sites, then immediately after stabilization we could possibly unblock the sites and allow the photons to then thermalize on a larger lattice. This would require developing a way to detune/tune lattice sites quickly ($< 100ns$ preferably) and while in the cryostat. There are several ways this could be implemented. First, designing flux-tunable qubits that work in 3D cavities would easily open this door, since they could simply be tuned to be off resonant with the lattice. Without using flux-tunable qubits we would need a way to detune certain qubits in the lattice to create the wall. The qubits could be excited to the h-state so that they are off resonant, but then the qubits would need a long lifetime while the blocked up lattice fills up to the e state. The blocking qubits could be driven hard slightly off-resonant to AC stark shift the qubit mode off resonance. The AC Stark shift is proportional to the $\frac{\Omega_R^2}{\Delta_A C}$, where Ω_R is the Rabi rate and $\Delta_A C$ is the detuning between the applied tone and qubit transition. A fast Rabi rate of 50 ns and a reasonable detuning of 10 MHz could potentially produce frequency shifts of ~40 MHz, which could be enough of a shift depending on the tunneling rates used. The flexibility of this system to modularly add different components to achieve different Hamiltonians allows it to study many different interesting quantum systems on lattices.

6.3 Exotic Boundary Conditions

In some of our work on circuits [1], we exploited the ability to connect the boundaries of the sample to other edges of the sample to make toroidal boundary conditions and then to

braid those boundary connections in to a Möbius strip. Coupling arbitrary lattice sites to other sites not only offers exciting possibilities in studying exotic topology and curvature, but also can be used to eliminate the edge of the lattice entirely. The edge of materials, while interesting in its own right, complicates the models we are trying to understand. As seen even in the non-interacting case, the edge adds different type of states to the system and just understanding bulk states unaffected by an edge is difficult. If we could eliminate the edge and apply periodic boundary conditions we could use our system to study Hamiltonians that theory is closer to explaining.

We lose a lot of the flexibility that we had working with circuits since (1) we are working with microwaves with wavelengths ∼1 cm so connecting edges of a 10 cm lattice with anything trivial would introduce new modes and (2) we have to preserve both power and phase (for the magnetic field) in these long range couplings. There are, however, still possible methods to couple cavities at long range to each other without loss or extra phase accumulation. One idea on which we have done some preliminary testing is using a ladder of off-resonant, higher frequency cavities to create a coupler that has modes with a concentration of the wavefunction living on the edge of the cavity chain. Some of our early simulations have coupled lattice site with a g of ∼10 MHz over a distance greater than the entire length of the lattice (∼20 cm). Another way to do this is to change the geometry of the piece on which the lattice is machined. It would be feasible to make a lattice actually on a large cylinder or a sphere, though the machining would be technically difficult. In the same vein, a lattice could be machined on both sides of a block of metal, and then coupled through the piece of metal. In effect there would be two sublattices but how these sublattices are connected to each other could be controlled. If only two opposite edges of a sublattice were coupled to the same mirrored edges of the other sublattice, then the resultant topology would be a cylinder, and only two edges would be left. Unfortunately, if one connects the remaining edges in a similar fashion, then the corners of the lattice would be topological defects since they only have three connections while every other site has four. A final idea is to use a

very short coax cable. If the length is chosen correctly then the cable could have a sparse enough density of states that you could have all of the cable modes off resonant. When the cable is then coupled to the cavities, the population of the excitations living in the cable would be suppressed at the lattice frequency, similar to the results found by transporting quantum states through a cable [68]. There are many possible ways to couple cavities at longer distances to each other, and achieving this goal would add another powerful tool to this toolbox of this approach to quantum simulation.

6.4 Other Lattice Geometries

The square lattice discussed in the thesis was one of the most efficient ways to minimize the number of YIG cavities while still achieving a flux that produces band structures with flat bands and large band gaps. In the current scheme the YIG cavities are sites that shift the phase of the photon by the angle between the couplers. In Figure 6.2 we show several other potential lattices that could be used that have different flux per plaquette. The hexagonal lattice would require next nearest neighbor coupling which has not been done yet. Another way to make more arbitrary magnetic fields would be to use the YIG cavities as couplers between sites. In this configuration, the coupler can be bent in such a way that the phase acquired tunneling through it would be tunable depending on the angle the coupler is bent. This method would require large amounts of YIG cavities but could be employed to explore different flux per plaquette.

6.5 Low Loss, Low Profile Tunable Circulators

Another use for the YIG cavities would be to make microwave circulators out of them. The YIG cavities can be made quite small and chained together to produce extremely high non-

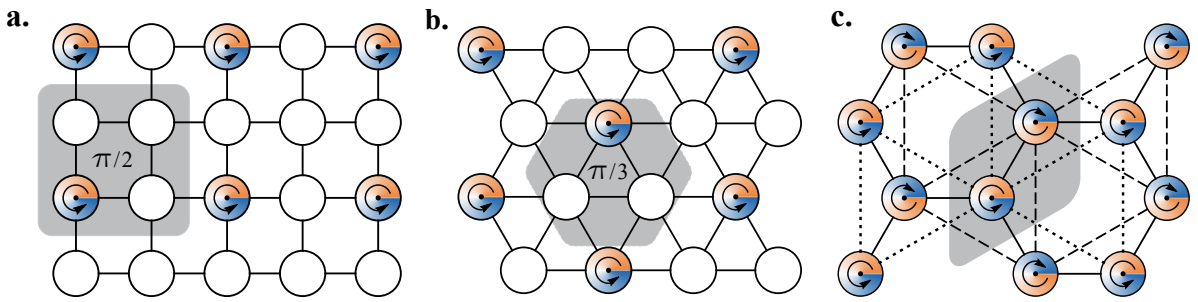

Figure 6.2: Three different type of lattices that could be made using the components we already have to achieve different magnetic fluxes in the lattice. **a.** Current Lattice arrangement that has a flux per plaquette of $\frac{\pi}{2}$. **b.** Triangular lattice that would have $\frac{\pi}{3}$ flux per plaquette. **c.** The Haldane model realized with YIG cavities. A hexagonal lattice with Yig cavities on every site, but their chiralities are staggered. When next nearest neighbor tunneling is added, the net flux through the lattice is 0, but the flux in each sub lattice is $\pm\frac{\pi}{3}$. This figure is from our theory paper [3].

reciprocity in a device. In order to achieve chiral transport, the two chiral modes have to interfere with each other in such a way to destructively interfere at one port and constructively interfere at another. To do this, we make the coupling quality factor of the modes low enough so the linewidth of the modes is equal to the splitting between the chiral modes. In the frequency region between the two mode frequencies, we get nonreciprocity. In Figure 6.3, we plot both theoretical curves and some preliminary data showing difference in transport between two ports on the cavity 120 degrees apart. In order to get the nonreciprical transport, the linewidth of the modes has to be carefully matched to the splitting between the cavity modes. For our preliminary data it was only approximately matched so there is a lot of loss in the through direction. The bandwidth of the circulator is limited by the splitting between the chiral modes, which maxes out in cavity designs I have tried at 500 MHz. Making the circulators tunable would also be possible, since any type of screw or dielectric could tune the resonator.

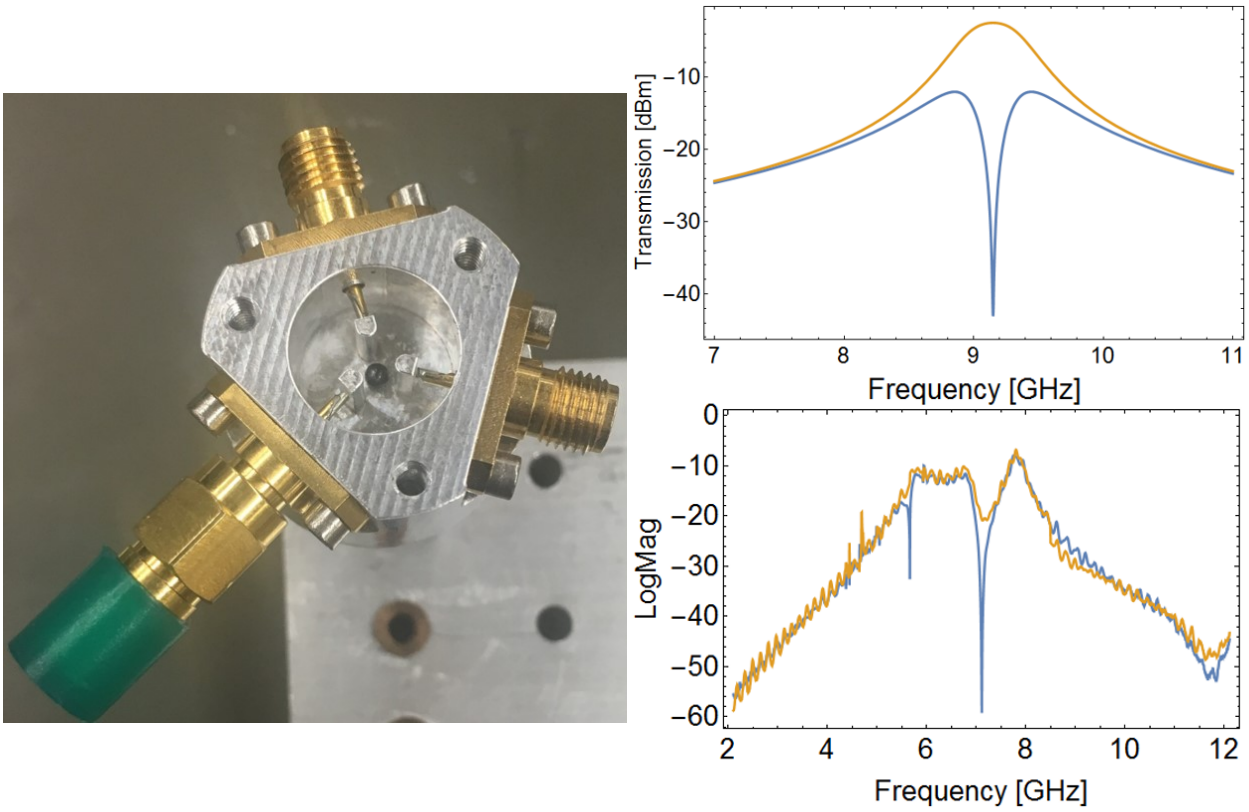

Figure 6.3: **Left.** Picture of a YIG cavity circulator setup. The three ports are 120 degrees apart and strongly coupled to the cavity. A 2mm YIG sphere is in the center of the cavity and a magnetic is on a micrometer below the cavity to tune the chiral mode splitting. **Right.** Theory and data for transmission between two ports of the cavity. One color is one direction while the other is the opposite. In the theory there should be a region with near perfect transmission one direction but large suppression the other direction (40 dBm). The data is not near as clean, due to couplings in the antenna not being balanced and the presence of the higher order YIG modes coupling to the cavity as well.

6.6 Chiral Quantum Optics

Currently we are exploring chiral quantum optics with the lattice coupled to two qubits. Our lattice already supports chiral modes with time reversal symmetry broken, and we have already coupled the lattice to single photon emitters and detectors (qubits). We are currently trying experiments in which we emit photons from one emitter and try to catch it at a different emitter coupled to the edge mode. As discussed in Section 3.8, we could make effectively two topological lattices, coupled by a single nonlinear site (coupled to a transmon). If we pulse the edge mode of one of the lattices, the pulse would eventually reach the nonlinear site and excite it. When it is excited, it becomes detuned and therefore a barrier for the rest of the pulse. Eventually the qubit will reemit the photon, into one of the two lattices. This could be an interesting single photon source, or used to put the emitted photon into a superposition of being in the left or right lattice. We could also use the single site to entangle photons in the different sublattices. As we increase our ability to add and control qubits, many interesting quantum systems coupled by chiral modes will become available for exploration.

Several proposals have shown that exciting physics occur when emitters are coupled to the edge state of a Chern insulator. First, such methods can trap chiral photonic bound states which can lead to directional, long-range interactions and many-body phases [69]. Second, these approaches can host parity-dependent scattering and antibunching of photons, caused by the emitters contributing an effective interaction in the edge mode [70]. In many proposals, the topological system does not break time reversal symmetry, so the emitter is restricted to couple to only one of the chiral modes. In our system, the chiral modes are split in energy so that happens easily. With two emitters, one can form a steady, pure entangled many-atom state by exciting both emitters [14]. In general, connnecting quantum networks with chiral channels could be intriguing for implementing different types of quantum simulators.

CHAPTER 7

CONCLUSIONS

The result of this work was the development of new and exciting tools to build quantum topological materials out of microwave light. We first engineered a microwave cavity lattice that could generate a tight-binding Hamiltonian for photons. We then designed a time-reversal symmetry breaking magnetic field for microwave photons using onsite wave functions to generate a Peierl's phase for photons that tunnel through certain lattice sites. Time reversal symmetry was broken by coupling a YIG sphere biased with a DC magnetic field to chiral cavity modes. All of these innovations were designed to be compatible with low-loss superconducting cavities to increase particle lifetimes and with transmon qubits to add inter-particle interactions.

We then implemented the magnetic field in a superconducting niobium lattice, developing methods to minimize resonator disorder to < 1 MHz and reach time-reversal-symmetry-breaking frequencies of 180 MHz, while achieving chiral resonator quality factors of 200,000. We measured superconducting topologically protected edge modes of a Chern insulator with lifetimes greater than 3 μs compared to lattice hopping rates of 6 ns. Finally, we coupled the lattice to a qubit while maintaining qubit lifetimes great than 2 μs. We then performed quantum swaps of qubit states into a single lattice in the presence of the biasing field required to tune the YIG sphere. Currently we are exploring the system of a single qubit coupled to the edge of our topological insulator.

With these advancements, we have opened many doors to possible quantum simulations. This is the first photonic, time-reversal-symmetry-breaking topological lattice platform that is compatible with strong interactions. There are many ideas for what types of physics would be interesting to explore next, and I anticipate an exciting future of quantum simulation with microwave photons.

Appendices

APPENDIX A

TRANSMON FABRICATION RECIPE

There were two general recipes followed for making qubits, depending on whether we were making qubits in one layer drawn completely in the e-beam or using both an optical and e-beam layer. Written below is the recipe for the optical plus e-beam layer. If only an e-beam layer is used, we follow the cleaning steps and then proceed directly to the PPMA/MMA coating steps and continue on exactly like the optical plus e-beam.

Qubit Fabrication on Sapphire Wafer:

1. Start with a blank annealed Sapphire wafer
2. TAMI Clean the wafer
    (a) 3min - sonicate Toluene
    (b) 3min - sonicate Acetone
    (c) 3min - sonicate Methanol
    (d) 3min - sonicate IPA
    (e) 3min Rinse under running DI water
    (f) Spin dry and blow dry with N2 gun
3. Evaporate Base Layer
    (a) Load into Plassys with wafer flat aligned with rotation arm
    (b) Run the heater code to evaporate any remaining water
    (c) Pump down and cool overnight
    (d) Evaporate 75 nm Nb

(e) Remove from Plassys

4. Spin Photoresist immediate after evaporation:

   (a) Use AX 703, Speed 3500 rpm, ramp 1000 rpm, time 45 seconds

   (b) Place wafer on spinner and turn on vacuum

   (c) Run recipe

   (d) Immediately bake the wafer

      i. 1 min

      ii. 95 C

   (e) Cool wafer on the bench for 10 seconds

5. Optical Patterning on Heidelberg

   (a) Prepare File and convert the design

   (b) Check in viewer- black parts are exposed

   (c) Load the file, load laser (405 nm is best with AZ 703)

   (d) Load wafer

   (e) Dose- For feature sizes bigger than 7μm use dose of 120 with 405 laser, otherwise switch to 375 laser and use dose of 132.

   (f) use focus written on the side of the machine- This is updated daily

   (g) Start exposure

6. Developing the Optical Resist

   (a) Bake for 1 minute at 95C, then rest the wafer for 3 minutes

   (b) Develop the wafer in AZ MIF 300 for 1 minute, gently agitating the solution while it develops

(c) Quench in DI water for 10 seconds

(d) Rinse under DI water for 3 minutes

(e) Spin Dry

(f) Verify that the patterns are correct under microscope

7. Descuming- optional, I did not use it for my qubits

8. Etch the base layer

   (a) Flourine etch for 75 nm base layer

   (b) Test first with dummy wafer

   (c) Use the niobium recipe, run it for twice as long as it normally works

   (d) For the actual wafer watch the wafer as it etches and abort the process when it is finished- should take 3 minutes

   (e) Vent and retrieve wafer

9. Strip Photoresist

   (a) Run recipe 7 on Asher

   (b) 15 minute or longer in 80C NMP or PG Remover

   (c) sonicate in 80C NMP for 5 minutes

   (d) Move to IPA while mechanically rinsing with IPA while transferring

   (e) Sonicate in IPA for 3 minutes

   (f) Rinse with DI water for 3 minutes

   (g) Spin Dry

10. Vacuum Bake- Run Recipe 4

11. Spin Bi-Layer E-beam resist

(a) First layer- MMA EL11, 4000 rpm, ramp 500 rpm/second, time 45 seconds

(b) Bake 180 C for 5 minutes

(c) Second layer- Spin PPMA 950 A7, 4000 rpm, ramp 500 rpm/second, time 45 seconds

(d) Bake 180 C for 5 minutes

12. Evaporate a Gold conduction layer

(a) Vent the thermal evaporator

(b) Place gold pellet holder in clamp, make good electrical contact

(c) Mount and load wafer

(d) Pump down

(e) Run S3 Gold recipe, Max current should be 40%, use 10 nm of gold

(f) Vent, unload, and demount wafer

13. E-beam resist

(a) Prep the E-beam resist developer

i. 6C cold plate

ii. 3:1 IPA:water

iii. Mix well and close lid, let sit at least 1 hr for proper thermalization

(b) Prepare patter with Beamer, export to Raith computer

(c) Vent raith, unload sample holder

(d) Clamp wafer down and screw electrical contact pads down

(e) Record location of alignment marks (if doing more than 1 layer) at microscope

(f) Load sample into Raith and pump down

(g) Find alignment markers and record their positions

(h) Add alignment marker position to cjob file

(i) Run cjob file

14. Etch gold

(a) Submerge wafer in iodine for 45 seconds

(b) Quench in water

(c) Mechanical rinse with water for at least 3 minutes

(d) Dry very well using spinner or N2 gun

15. Develop E-beam resist

(a) Place wafer in develoer

(b) Wait 1:30 minutes, use a timer

(c) Immediately rinse with DI water

(d) Dry with N2 gun as quickly as possible to make sure all the developer is removed

(e) Check pattern under optical microscope

16. Evaporate junctions

(a) Load wafer into Plassys with appropriate orientation relative to the rotation arm

(b) Pump down overnight

(c) Run junction evaporation recipe

i. For single layer: Ar/O_2 gentle descum to clean up any developed photoresist, deposit 20nm thickness of aluminum at evaporation angle of 40°, 20 mbar oxygen for 10 minutes, rotate stage 90° and then deposit 45 nm of aluminum at an evaporation angle of 40°

ii. For double layer: Ar/O_2 gentle descum to clean up any developed photoresist, deposit 80nm thickness of aluminum at evaporation angle of 40°, 20 mbar

oxygen for 10 minutes, Ion gun (use standard recipe) for 10 seconds at +45°, 0°, and −45°, rotate stage 90° and then deposit 45 nm of aluminum at an evaporation angle of 40°

17. Dicing the qubits

    (a) First coat qubit with AX1518- 2500 rpm, 45 seconds

    (b) bake for 5 minutes at 70C

    (c) Mount onto tape

    (d) Dice qubits in dicing machine

18. Liftoff

    (a) PG remover at 80C for 3 hours for diced qubits, longer for wafers

    (b) IPA rinse and bath

    (c) DI rinse

    (d) N2 dry

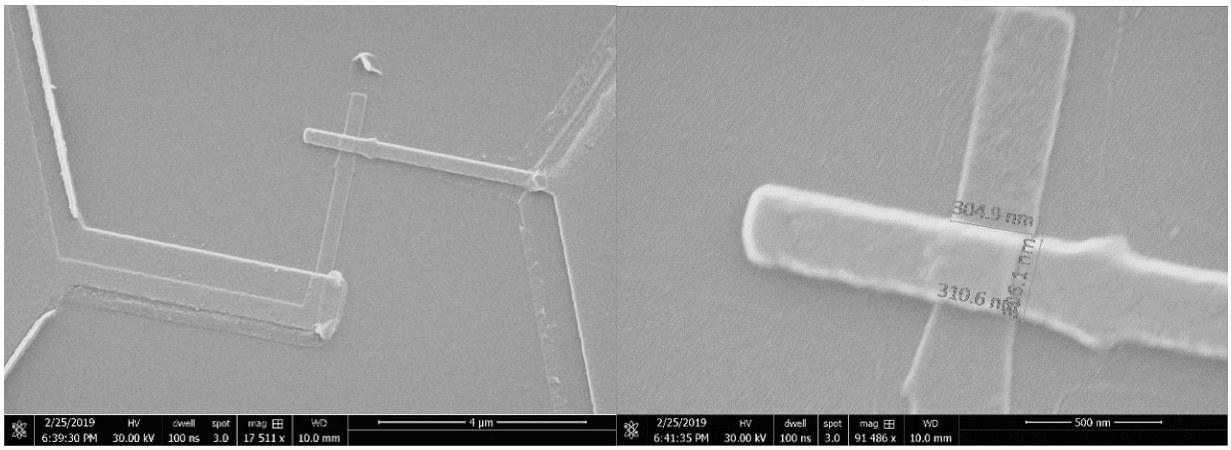

Figure A.1: **Left.** SEM images of one of the first junctions I made following this recipe

APPENDIX B

MATHEMATICA CODE

Included are the Mathematica codes used to calculate the lattice band structure and transmission through the lattice:

```
freqoffset = 6.37 * 2Pi;
Clear[Hmat]
Clear[ii]
Clear[jj]
Size = 21;
FundamentalOnOutside = True;
siteindices = Flatten[Table[{ii, jj}, {ii, 1, 2}, {jj, 1, Size}], 1];
J = 32.5;
ϕ = 1/4 * 2Pi; κ = 0. 3;
ω0 = 9600 − freqoffset;
(*getsiteindex[ii_, jj_]:=1 + If[Length[#] > 0, #[[1, 1]], 0]&[Position[siteindices, {ii, jj}]]; *)
(* dumps all out of bound states into index 1*)

nInd = Length[siteindices];

(*Hmat = Table[0, {nInd}, {nInd}];
Hmat+=Table[If[ll == qq, ω0, 0], {ll, 1, nInd}, {qq, 1, nInd}]; *)
Hmat = Table[0, {nInd}, {nInd}];
For[ii = 1, ii ≤ 2, ii++,
For[jj = 1, jj ≤ Size, jj++,
curind = getsiteindex[ii, jj];
```

```
Hmat[[curind, curind]]+=ω0(* + RandomReal[{-5, 5}]/(2Pi)*) + I κ/2;]]


For[jj = 1, jj ≤ Size - 1, jj++,
ii = 1;
Hmat[[getsiteindex[ii, jj], getsiteindex[ii, jj + 1]]]+= - JExp[-I ϕ];
Hmat[[getsiteindex[ii, jj + 1], getsiteindex[ii, jj]]]+= - JExp[I ϕ];

ii = 2;
Hmat[[getsiteindex[ii, jj], getsiteindex[ii, jj + 1]]]+= - J;
Hmat[[getsiteindex[ii, jj + 1], getsiteindex[ii, jj]]]+= - J;
]

If[FundamentalOnOutside==True,
For[jj = 1, jj ≤ (Size + 1)/2, jj++,
ii = 1;
Hmat[[getsiteindex[ii, 2jj - 1], getsiteindex[ii + 1, 2jj - 1]]]+= - J - JExp[2Iq];
Hmat[[getsiteindex[ii + 1, 2jj - 1], getsiteindex[ii, 2jj - 1]]]+= - J - JExp[-2Iq];
]

For[jj = 1, jj ≤ (Size - 1)/2, jj++,
ii = 1;
Hmat[[getsiteindex[ii, 2jj], getsiteindex[ii + 1, 2jj]]]+=J - JExp[2Iq];
Hmat[[getsiteindex[ii + 1, 2jj], getsiteindex[ii, 2jj]]]+=J - JExp[-2Iq];
],

For[jj = 1, jj ≤ (Size - 1)/2, jj++,
```

```
ii = 1;
Hmat[[getsiteindex[ii, 2jj], getsiteindex[ii + 1, 2jj]]]+= - J - JExp[2Iq];
Hmat[[getsiteindex[ii + 1, 2jj], getsiteindex[ii, 2jj]]]+= - J - JExp[-2Iq];
]

For[jj = 1, jj ≤ (Size + 1)/2, jj++,
ii = 1;
Hmat[[getsiteindex[ii, 2jj - 1], getsiteindex[ii + 1, 2jj - 1]]]+=J - JExp[2Iq];
Hmat[[getsiteindex[ii + 1, 2jj - 1], getsiteindex[ii, 2jj - 1]]]+=J - JExp[-2Iq];
]
]


evs = Table[Eigenvalues[Hmat], {q, -Pi/2, Pi/2, .01}];
qs = Table[q, {q, -Pi/2, Pi/2, .01}];
tt = Table[Transpose[{qs, evs[[;;, q]]}], {q, 1, Length[evs[[1]]]}];

ListLinePlot[Sort[tt[[;;]]], PlotRange → All]
```

And for calculating transmission:

```
getsiteindex[ii_, jj_]:=If[Length[#] > 0, #[[1, 1]], 0]&[Position[siteindices, {ii, jj}]];
Clear[Hmat]
Clear[ii]
Clear[jj]
Size = 11;
FundamentalOnOutside = True;
siteindices = Flatten[Table[{ii, jj}, {ii, 1, Size}, {jj, 1, Size}], 1];
J = .032;
```

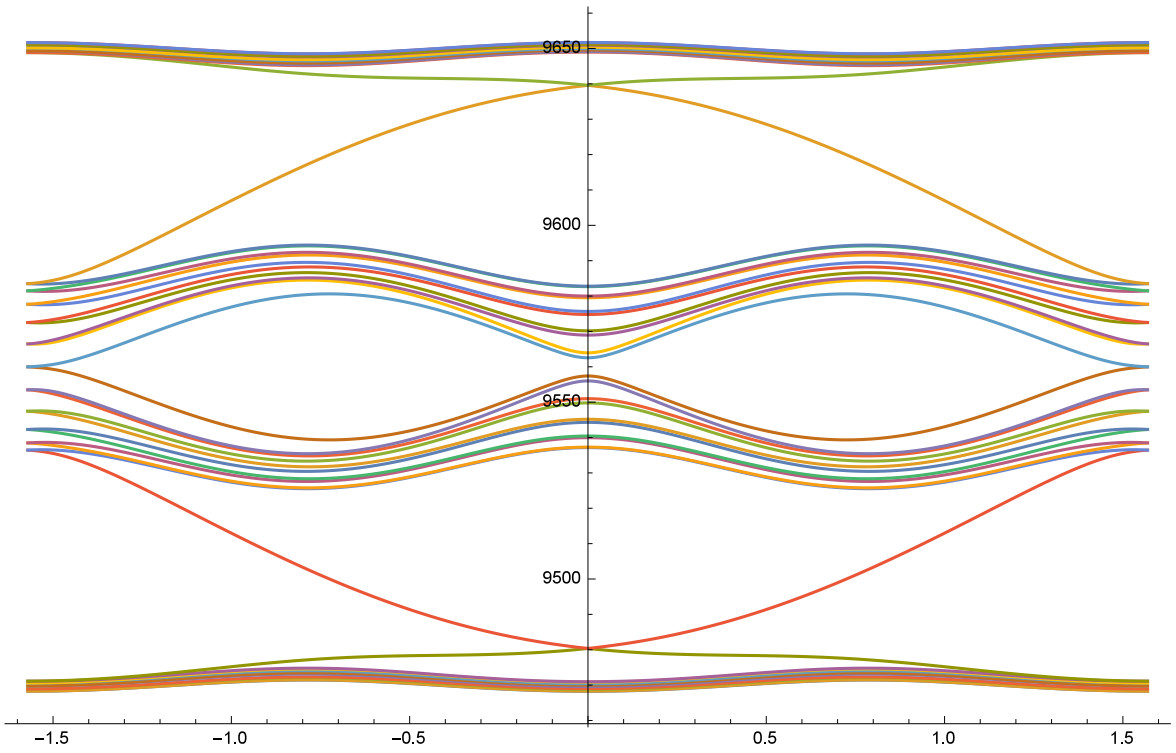

Figure B.1: Calculated band structure of the quarter-flux Hofstadter Lattice.

```
ϕ = 1/4 * 2Pi; κ = .003;
ω0 = 9.600;
(*getsiteindex[ii_, jj_]:=1 + If[Length[#] > 0, #[[1, 1]], 0]&[Position[siteindices, {ii, jj}]]; *)
(* dumps all out of bound states into index 1*)

nInd = Length[siteindices];

(*Hmat = Table[0, {nInd}, {nInd}];
Hmat+=Table[If[ll == qq, ω0, 0], {ll, 1, nInd}, {qq, 1, nInd}]; *)
Hmat = Table[0, {nInd}, {nInd}];
For[ii = 1, ii ≤ Size, ii++,
For[jj = 1, jj ≤ Size, jj++,
curind = getsiteindex[ii, jj];
 Hmat[[curind, curind]]+=ω0(* + RandomReal[{−5, 5}]/(2Pi)*) + I κ/2; ]]
```

```
For[jj = 1, jj ≤ Size − 1, jj++,
For[ii = 1, ii ≤ (Size + 1)/2, ii++,
Hmat[[getsiteindex[2ii − 1, jj], getsiteindex[2ii − 1, jj + 1]]] += − JExp[−I ϕ];
Hmat[[getsiteindex[2ii − 1, jj + 1], getsiteindex[2ii − 1, jj]]] += − JExp[I ϕ];
]
For[ii = 1, ii ≤ (Size − 1)/2, ii++,
Hmat[[getsiteindex[2ii, jj], getsiteindex[2ii, jj + 1]]] += − J;
Hmat[[getsiteindex[2ii, jj + 1], getsiteindex[2ii, jj]]] += − J;
]
]

If[FundamentalOnOutside==True,
For[jj = 1, jj ≤ (Size + 1)/2, jj++,
For[ii = 1, ii ≤ Size − 1, ii++,
Hmat[[getsiteindex[ii, 2jj − 1], getsiteindex[ii + 1, 2jj − 1]]] += − J;
Hmat[[getsiteindex[ii + 1, 2jj − 1], getsiteindex[ii, 2jj − 1]]] += − J;
]
]

For[jj = 1, jj ≤ (Size − 1)/2, jj++,
For[ii = 1, ii ≤ (Size − 1)/2, ii++,
Hmat[[getsiteindex[2ii − 1, 2jj], getsiteindex[2ii, 2jj]]] += − J;
Hmat[[getsiteindex[2ii, 2jj], getsiteindex[2ii − 1, 2jj]]] += − J;
]
```

```
For[ii = 1, ii ≤ (Size − 1)/2, ii++,
Hmat[[getsiteindex[2ii, 2jj], getsiteindex[2ii + 1, 2jj]]]+=J;
Hmat[[getsiteindex[2ii + 1, 2jj], getsiteindex[2ii, 2jj]]]+=J;
]
]


(*,
For[jj = 1, jj ≤ (Size − 1)/2, jj++,
ii = 1;
Hmat[[getsiteindex[ii, 2jj], getsiteindex[ii + 1, 2jj]]]+= − J − JExp[2Iq];
Hmat[[getsiteindex[ii + 1, 2jj], getsiteindex[ii, 2jj]]]+= − J − JExp[−2Iq];
]

For[jj = 1, jj ≤ (Size + 1)/2, jj++,
ii = 1;
Hmat[[getsiteindex[ii, 2jj − 1], getsiteindex[ii + 1, 2jj − 1]]]+=J − JExp[2Iq];
Hmat[[getsiteindex[ii + 1, 2jj − 1], getsiteindex[ii, 2jj − 1]]]+=J − JExp[−2Iq];
]*)
]

nSys = Length[Hmat];
Imat = IdentityMatrix[Length[Hmat]];

{es, vs} = Eigensystem[Re[Hmat//N]];

xin = 1;
yin = 1;
```

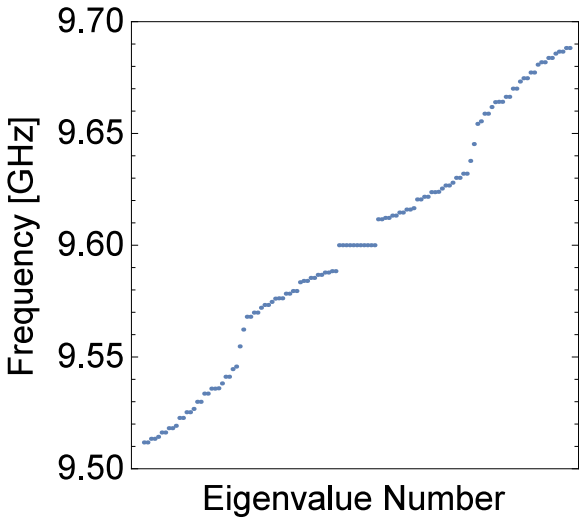

Figure B.2: Eigenvalues of the Hofstadter Hamiltonian.

```
inIndex = getsiteindex[xin, yin]; (* − 1isthefix*)

ψin = Table[If[kk == inIndex, 1, 0], {kk, 1, nSys}];

GetPlot[dat_]:=Table[dat[[getsiteindex[ii, jj]]], {ii, 1, Size}, {jj, 1, Size}];
```

```
Export["frequencydrivehigh.pdf", FrequencyDrive]
```

frequencydrivehigh.pdf

```
Export["ResponseAtFreqhigh.pdf", Response]
```

ResponseAtFreqhigh.pdf

```
Clear[pout]

xin = 1;

yin = 1;

xout = 10;
```

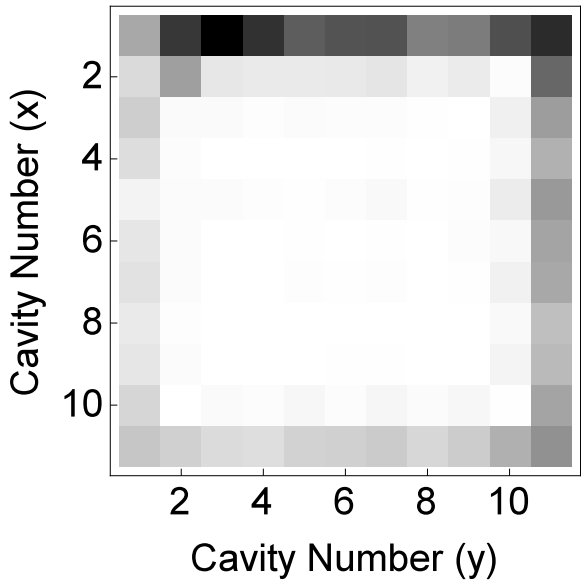

Figure B.3: Transmission in an Edge Mode

```
yout = 1;
outIndex = getsiteindex[xout, yout];
inIndex = getsiteindex[xin, yin];
pin = Table[If[kk == inIndex, 1, 0], {kk, 1, nSys}];
pout = Table[If[kk == outIndex, 1, 0], {kk, 1, nSys}];


xin = 5;
yin = 5;
xout = 5;
yout = 5;
outIndex = getsiteindex[xout, yout];
inIndex = getsiteindex[xin, yin];
pin2 = Table[If[kk == inIndex, 1, 0], {kk, 1, nSys}];
pout2 = Table[If[kk == outIndex, 1, 0], {kk, 1, nSys}];
```

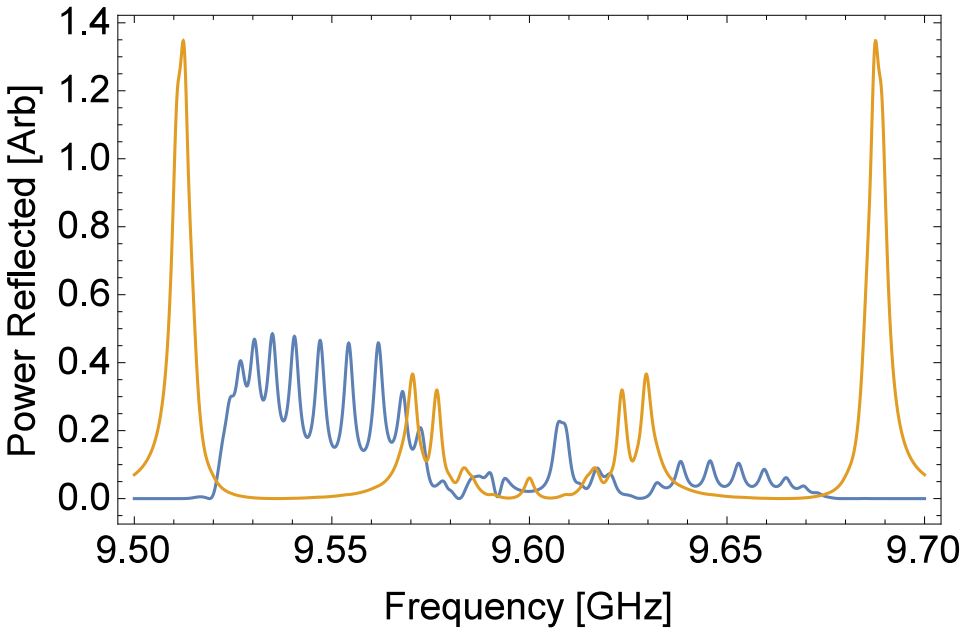

Figure B.4: Transmission between bulk sites (yellow) and edge sites (blue)

PlotT =

Plot[{.0006(Abs[pout.Inverse[Hmat − Imat ∗ δ].pin]^2) + .00,

.0001Abs[pout2.Inverse[Hmat − Imat ∗ δ].pin2]^2}, {δ, 9.500, 9.700}, PlotRange → All,

Frame → True, FrameLabel → {"Frequency [GHz]", "Power Reflected [Arb]"},

FrameStyle → Directive[Black, 20], PlotStyle → Bold, ImageSize → 500]

REFERENCES

[1] Jia Ningyuan, Clai Owens, Ariel Sommer, David Schuster, and Jonathan Simon. Time- and site-resolved dynamics in a topological circuit. *Physical Review X*, 5:021031, Jun 2015.

[2] Yuehui Lu, Ningyuan Jia, Lin Su, Clai Owens, Gediminas Juzeliūnas, David I. Schuster, and Jonathan Simon. Probing the berry curvature and fermi arcs of a weyl circuit. *Phys. Rev. B*, 99:020302, Jan 2019.

[3] Brandon M Anderson, Ruichao Ma, Clai Owens, David I Schuster, and Jonathan Simon. Engineering topological many-body materials in microwave cavity arrays. *Physical Review X*, 6(4):041043, 2016.

[4] Clai Owens, Aman LaChapelle, Brendan Saxberg, Brandon M Anderson, Ruichao Ma, Jonathan Simon, and David I Schuster. Quarter-flux hofstadter lattice in a qubit-compatible microwave cavity array. *Physical Review A*, 97(1):013818, 2018.

[5] Simon E Nigg, Hanhee Paik, Brian Vlastakis, Gerhard Kirchmair, Shyam Shankar, Luigi Frunzio, MH Devoret, RJ Schoelkopf, and SM Girvin. Black-box superconducting circuit quantization. *Physical Review Letters*, 108(24):240502, 2012.

[6] Kieran A Murphy, Karin A Dahmen, and Heinrich M Jaeger. Transforming mesoscale granular plasticity through particle shape. *Physical Review X*, 9(1):011014, 2019.

[7] John Bardeen, Leon N Cooper, and John Robert Schrieffer. Theory of superconductivity. *Physical Review*, 108(5):1175, 1957.

[8] SA Kivelson and DS Rokhsar. Bogoliubov quasiparticles, spinons, and spin-charge decoupling in superconductors. *Physical Review B*, 41(16):11693, 1990.

[9] J George Bednorz and K Alex Müller. Possible high tc superconductivity in the ba- la- cu- o system. *Zeitschrift für Physik B Condensed Matter*, 64(2):189–193, 1986.

[10] David Isaac Schuster. *Circuit quantum electrodynamics*. Yale University, 2007.

[11] D Ristè, CC Bultink, MJ Tiggelman, RN Schouten, KW Lehnert, and L DiCarlo. Millisecond charge-parity fluctuations and induced decoherence in a superconducting transmon qubit. *Nature communications*, 4:1913, 2013.

[12] Ningyuan Jia, Nathan Schine, Alexandros Georgakopoulos, Albert Ryou, Logan W Clark, Ariel Sommer, and Jonathan Simon. A strongly interacting polaritonic quantum dot. *Nature Physics*, 14(6):550, 2018.

[13] Ruichao Ma, Clai Owens, Andrew Houck, David I Schuster, and Jonathan Simon. Autonomous stabilizer for incompressible photon fluids and solids. *Physical Review A*, 95(4):043811, 2017.

[14] Peter Lodahl, Sahand Mahmoodian, Søren Stobbe, Arno Rauschenbeutel, Philipp Schneeweiss, Jürgen Volz, Hannes Pichler, and Peter Zoller. Chiral quantum optics. *Nature*, 541(7638):473, 2017.

[15] K v Klitzing, Gerhard Dorda, and Michael Pepper. New method for high-accuracy determination of the fine-structure constant based on quantized hall resistance. *Physical Review Letters*, 45(6):494, 1980.

[16] Horst L. Stormer, Daniel C. Tsui, and Arthur C. Gossard. The fractional quantum hall effect. *Review of Modern Physics*, 71:S298–S305, Mar 1999.

[17] R De-Picciotto, M Reznikov, M Heiblum, V Umansky, G Bunin, and D Mahalu. Direct observation of a fractional charge. *Physica B: Condensed Matter*, 249:395–400, 1998.

[18] Ady Stern. Anyons and the quantum hall effect - a pedagogical review. *Annals of Physics*, 323(1):204–249, 2008.

[19] Chetan Nayak, Steven H Simon, Ady Stern, Michael Freedman, and Sankar Das Sarma.

Non-abelian anyons and topological quantum computation. *Reviews of Modern Physics*, 80(3):1083, 2008.

[20] Sanghun An, P Jiang, H Choi, W Kang, SH Simon, LN Pfeiffer, KW West, and KW Baldwin. Braiding of abelian and non-abelian anyons in the fractional quantum hall effect. *arXiv preprint arXiv:1112.3400*, 2011.

[21] Robert L Willett, Loren N Pfeiffer, and KW West. Alternation and interchange of e/4 and e/2 period interference oscillations consistent with filling factor 5/2 non-abelian quasiparticles. *Physical Review B*, 82(20):205301, 2010.

[22] Waheb Bishara, Parsa Bonderson, Chetan Nayak, Kirill Shtengel, and J. K. Slingerland. Interferometric signature of non-abelian anyons. *Physical Review B*, 80:155303, Oct 2009.

[23] R.O. Umucalilar and I. Carusotto. Many-body braiding phases in a rotating strongly correlated photon gas. *Physics Letters A*, 377(34–36):2074 – 2078, 2013.

[24] Fabian Grusdt, Norman Y Yao, D Abanin, Michael Fleischhauer, and E Demler. Interferometric measurements of many-body topological invariants using mobile impurities. *Nature communications*, 7, 2016.

[25] Immanuel Bloch, Jean Dalibard, and Wilhelm Zwerger. Many-body physics with ultracold gases. *Reviews of Modern Physics*, 80(3):885, 2008.

[26] Lisa M Nash, Dustin Kleckner, Alismari Read, Vincenzo Vitelli, Ari M Turner, and William TM Irvine. Topological mechanics of gyroscopic metamaterials. *Proceedings of the National Academy of Sciences*, 112(47):14495–14500, 2015.

[27] Roman Süsstrunk and Sebastian D Huber. Observation of phononic helical edge states in a mechanical topological insulator. *Science*, 349(6243):47–50, 2015.

[28] Markus Greiner, Olaf Mandel, Tilman Esslinger, Theodor W Hänsch, and Immanuel Bloch. Quantum phase transition from a superfluid to a mott insulator in a gas of ultracold atoms. *Nature*, 415(6867):39–44, 2002.

[29] N.R. Cooper. Rapidly rotating atomic gases. *Advances in Physics*, 57(6):539–616, 2008.

[30] Nathan Gemelke, Edina Sarajlic, and Steven Chu. Rotating few-body atomic systems in the fractional quantum hall regime. *arXiv preprint arXiv:1007.2677*, 2010.

[31] Y. J. Lin, R. L. Compton, K. Jimenez-Garcia, J. V. Porto, and I. B. Spielman. Synthetic magnetic fields for ultracold neutral atoms. *Nature*, 462(7273):628–632, December 2009.

[32] NR Cooper. Optical flux lattices for ultracold atomic gases. *Physical Review Letters*, 106(17):175301, 2011.

[33] M Eric Tai, Alexander Lukin, Matthew Rispoli, Robert Schittko, Tim Menke, Dan Borgnia, Philipp M Preiss, Fabian Grusdt, Adam M Kaufman, and Markus Greiner. Microscopy of the interacting harper–hofstadter model in the two-body limit. *Nature*, 546(7659):519, 2017.

[34] M. Aidelsburger, M. Atala, M. Lohse, J. T. Barreiro, B. Paredes, and I. Bloch. Realization of the hofstadter hamiltonian with ultracold atoms in optical lattices. *Physical Review Letters*, 111:185301, Oct 2013.

[35] Gregor Jotzu, Michael Messer, Remi Desbuquois, Martin Lebrat, Thomas Uehlinger, Daniel Greif, and Tilman Esslinger. Experimental realization of the topological haldane model with ultracold fermions. *Nature*, 515(7526):237–240, 11 2014.

[36] Yin-Chen He, Fabian Grusdt, Adam Kaufman, Markus Greiner, and Ashvin Vishwanath. Realizing and adiabatically preparing bosonic integer and fractional quantum hall states in optical lattices. *Physical Review B*, 96(20):201103, 2017.

[37] HafeziM., MittalS., FanJ., MigdallA., and TaylorJ. M. Imaging topological edge states in silicon photonics. *Nature Photonics*, 7(12):1001–1005, 12 2013.

[38] Nathan Schine, Albert Ryou, Andrey Gromov, Ariel Sommer, and Jonathan Simon. Synthetic landau levels for photons. *Nature*, 534(7609):671–675, Jun 2016. Letter.

[39] Mikael C. Rechtsman, Julia M. Zeuner, Yonatan Plotnik, Yaakov Lumer, Daniel Podolsky, Felix Dreisow, Stefan Nolte, Mordechai Segev, and Alexander Szameit. Photonic floquet topological insulators. *Nature*, 496(7444):196–200, 04 2013.

[40] Zheng Wang, Yidong Chong, J. D. Joannopoulos, and Marin Soljacic. Observation of unidirectional backscattering-immune topological electromagnetic states. *Nature*, 461(7265):772–775, 10 2009.

[41] Fabian Grusdt and Michael Fleischhauer. Fractional quantum hall physics with ultracold rydberg gases in artificial gauge fields. *Physical Review A*, 87(4):043628, 2013.

[42] Andreas Wallraff, David I Schuster, Alexandre Blais, L Frunzio, R-S Huang, J Majer, S Kumar, Steven M Girvin, and Robert J Schoelkopf. Strong coupling of a single photon to a superconducting qubit using circuit quantum electrodynamics. *Nature*, 431(7005):162–167, 2004.

[43] Pedram Roushan, Charles Neill, Anthony Megrant, Yu Chen, Ryan Babbush, Rami Barends, Brooks Campbell, Zijun Chen, Ben Chiaro, Andrew Dunsworth, et al. Chiral ground-state currents of interacting photons in a synthetic magnetic field. *Nature Physics*, 2016.

[44] AG Radnaev, YO Dudin, R Zhao, HH Jen, SD Jenkins, A Kuzmich, and TAB Kennedy. A quantum memory with telecom-wavelength conversion. *Nature Physics*, 6(11):894, 2010.

[45] A Grassellino, A Romanenko, D Sergatskov, O Melnychuk, Y Trenikhina, A Crawford, A Rowe, M Wong, T Khabiboulline, and F Barkov. Nitrogen and argon doping of niobium for superconducting radio frequency cavities: a pathway to highly efficient accelerating structures. *Superconductor Science and Technology*, 26(10):102001, 2013.

[46] Alicia J Kollár, Mattias Fitzpatrick, and Andrew A Houck. Hyperbolic lattices in circuit quantum electrodynamics. *Nature*, 571(7763):45, 2019.

[47] Pedram Roushan, Charles Neill, Anthony Megrant, Yu Chen, Ryan Babbush, Rami Barends, Brooks Campbell, Zijun Chen, Ben Chiaro, Andrew Dunsworth, et al. Chiral ground-state currents of interacting photons in a synthetic magnetic field. *Nature Physics*, 13(2):146, 2017.

[48] Kejie Fang, Zongfu Yu, and Shanhui Fan. Realizing effective magnetic field for photons by controlling the phase of dynamic modulation. *Nature photonics*, 6(11):782, 2012.

[49] Matthew Reagor, Hanhee Paik, Gianluigi Catelani, Luyan Sun, Christopher Axline, Eric Holland, Ioan M. Pop, Nicholas A. Masluk, Teresa Brecht, Luigi Frunzio, Michel H. Devoret, Leonid Glazman, and Robert J. Schoelkopf. Reaching 10ms single photon lifetimes for superconducting aluminum cavities. *Applied Physics Letters*, 102(19), 2013.

[50] Teresa Brecht, Matthew Reagor, Yiwen Chu, Wolfgang Pfaff, Chen Wang, Luigi Frunzio, Michel H Devoret, and Robert J Schoelkopf. Demonstration of superconducting micromachined cavities. *Applied Physics Letters*, 107(19):192603, 2015.

[51] Hanhee Paik, DI Schuster, Lev S Bishop, G Kirchmair, G Catelani, AP Sears, BR Johnson, MJ Reagor, L Frunzio, LI Glazman, et al. Observation of high coherence in josephson junction qubits measured in a three-dimensional circuit qed architecture. *Physical Review Letters*, 107(24):240501, 2011.

[52] Matthew Reagor, Wolfgang Pfaff, Christopher Axline, Reinier W Heeres, Nissim Ofek, Katrina Sliwa, Eric Holland, Chen Wang, Jacob Blumoff, Kevin Chou, et al. Quantum

memory with millisecond coherence in circuit qed. *Physical Review B*, 94(1):014506, 2016.

[53] Jaeyoon Cho, Dimitris G Angelakis, and Sougato Bose. Fractional quantum hall state in coupled cavities. *Physical Review Letters*, 101(24):246809, 2008.

[54] VR Karasik and I Yu Shebalin. Superconducting properties of pure niobium. *SOV PHYS JETP*, 30(6):1068–1075, 1970.

[55] Jerzy Krupka, Pavlo Aleshkevych, Bartlomiej Salski, Pawel Kopyt, and Adam Pacewicz. Ferromagnetic resonance revised–electrodynamic approach. *Scientific reports*, 7(1):5750, 2017.

[56] Ruichao Ma, Clai Owens, Aman LaChapelle, David I Schuster, and Jonathan Simon. Hamiltonian tomography of photonic lattices. *Physical Review A*, 95(6):062120, 2017.

[57] Jens Koch, Andrew A. Houck, Karyn Le Hur, and S. M. Girvin. Time-reversal-symmetry breaking in circuit-qed-based photon lattices. *Physical Review A*, 82:043811, Oct 2010.

[58] M. Z. Hasan and C. L. Kane. Colloquium. *Review of Modern Physics*, 82:3045–3067, Nov 2010.

[59] DT McClure, W Chang, Charles M Marcus, LN Pfeiffer, and KW West. Fabry-perot interferometry with fractional charges. *Physical Review Letters*, 108(25):256804, 2012.

[60] Sanghun An, Simas Glinskis, Woowon Kang, Leo Ocola, Loren Pfeiffer, Ken West, and Kirk Baldwin. Fabrication of electronic fabry-perot interferometer in the quantum hall regime. *arXiv preprint arXiv:1401.1897*, 2014.

[61] Jens Koch, M Yu Terri, Jay Gambetta, Andrew A Houck, DI Schuster, J Majer, Alexandre Blais, Michel H Devoret, Steven M Girvin, and Robert J Schoelkopf. Charge-insensitive qubit design derived from the cooper pair box. *Physical Review A*, 76(4):042319, 2007.

[62] Eliot Kapit, Mohammad Hafezi, and Steven H Simon. Induced self-stabilization in fractional quantum hall states of light. *Physical Review X*, 4(3):031039, 2014.

[63] M Hafezi, P Adhikari, and JM Taylor. Chemical potential for light by parametric coupling. *Physical Review B*, 92(17):174305, 2015.

[64] Alberto Biella, Florent Storme, José Lebreuilly, Davide Rossini, Rosario Fazio, Iacopo Carusotto, and Cristiano Ciuti. Phase diagram of incoherently driven strongly correlated photonic lattices. *Physical Review A*, 96(2):023839, 2017.

[65] Carles Navau, Jordi Prat-Camps, Oriol Romero-Isart, J Ignacio Cirac, and Alvaro Sanchez. Long-distance transfer and routing of static magnetic fields. *Physical Review Letters*, 112(25):253901, 2014.

[66] Lev S Bishop. Circuit quantum electrodynamics. *arXiv preprint arXiv:1007.3520*, 2010.

[67] Ruichao Ma, Brendan Saxberg, Clai Owens, Nelson Leung, Yao Lu, Jonathan Simon, and David I Schuster. A dissipatively stabilized mott insulator of photons. *Nature*, 566(7742):51, 2019.

[68] N Leung, Y Lu, S Chakram, RK Naik, N Earnest, R Ma, K Jacobs, AN Cleland, and DI Schuster. Deterministic bidirectional communication and remote entanglement generation between superconducting qubits. *npj Quantum Information*, 5(1):18, 2019.

[69] M. Bello, G. Platero, J. I. Cirac, and A. González-Tudela. Unconventional quantum optics in topological waveguide qed. *Science Advances*, 5(7), 2019.

[70] Matous Ringel, Mikhail Pletyukhov, and Vladimir Gritsev. Topologically protected strongly correlated states of photons. *New Journal of Physics*, 16(11):113030, 2014.

bib1